Additive Manufacturing for Antenna Applications

A Thesis Submitted to The University of Kent
for the Degree of Doctor of Philosophy
in Electronic Engineering

By

Sung Yun Jun

Abstract

This thesis presents methods to make use of additive manufacturing (AM) or 3D printing (3DP) technology for the fabrication of antenna and electromagnetic (EM) structures. A variety of 3DP techniques based on filament, resin, powder and nano-particle inks are applied for the development and fabrication of antennas. Fully and partially metallised 3D printed EM structures are investigated for operation at mainly microwave frequency bands. First, 3D Sierpinski fractal antennas are fabricated using binder jetting printing technique, which is an AM metal powder bed process. It follows with the introduction of a new concept of sensing liquids using and non-planer electromagnetic band gap (EBG) structure is investigated. Such structure can be fabricated with inexpensive fuse filament fabrication (FFF) in combination with conductive paint. As a third method, inkjet printing technology is used for the fabrication of antennas for origami paper applications. The work investigates the feasibility of fabricating foldable antennas for disposable paper drones using low-cost inkjet printing equipment. It then explores the applicability of inkjet printing on a 3D printing substrate through the fabrication of a circularly polarised patch antenna which combines stereolithography (SLA) and inkjet printing technology, both of which use inexpensive machines. Finally, a variety of AM techniques are applied and compared for the production of a diversity WLAN antenna system for customized wrist-worn application.

Sung Yun Jun

May 2018

Acknowledgements

I am deeply grateful to my supervisor, Dr. Benito Sanz Izquierdo for his continuous assistance, valuable suggestions, and enthusiastic encouragement during the planning and development of this research work. I have been extremely lucky to have such a wonderful supervisor. His immense knowledge and insightful views give me the motivation to develop my scientific knowledge and experimental background through his valuable suggestions during my work.

I would also like to give my special thanks to all the staff of the School of Engineering and Digital Arts at University of Kent for providing me with all the necessary help whenever needed. Special thanks to Simon Jakes for all his help and assistance with antenna fabrication and measurement.

Finally, I would like to express my gratitude to my wife (So Young Jung) for supporting me to focus on the successful completion of this work. I would also like to thank my parents (Dr. Eui Cheon Jun and Hwa Sun Kim) and my brother (Hyun Seok Jun) for providing me with continuous encouragement, understanding, and patience during my Ph.D. I would not have completed this thesis without their support and belief in me.

Table of Contents

List of Figures

List of Acronyms

AM	Additive manufacturing
3DP	3D printing
EBG	Electromagnetic band gap
EM	Electromagnetic
FFF	Fuse filament fabrication
FDM	Fused deposition modeling
SLA	Stereolithography
DLP	Digital light processing
SLS	Selective laser sintering
SLM	Selective laser melting
CP	Circularly polarized
PET	Polyethylene terephthalate
MEMS	Micro-electro-mechanical systems
CAD	Computer-aided design
PLA	Polylactic acid
ABS	Acrylonitrile butadiene styrene
UV	Ultraviolet
DOD	Drop-on-demand
mm-wave	millimeter wave
THz	Terahertz
EBM	Electron beam melting
RFID	Radio frequency identification
LCP	Liquid crystal polymer
BST	Barium strontium titanate
UHF	Ultra high frequency
WLAN	Wireless local area networks
CPW	Coplanar waveguide
GPS	Global positioning systems
WSN	Wireless sensor network
SIW	Substrate integrated waveguide

FIT	Finite integration technique
PBC	Periodic boundary condition
UAVs	Unmanned aerial vehicles

CHAPTER 1.

INTRODUCTION

1.1 Overview and Motivations

Additive manufacturing (AM) or 3D printing (3DP) is a technology that has been attracting significant attention from the research community and manufacturing industry [1]-[3]. AM offers rapid prototyping and the ability to fabricate complex objects from a digital 3D model. This technology produces a more realistic output using advanced electronics systems at lower costs, multiple functionalities and more flexibility than conventional lithographic technology. One of the most common AM techniques is fused deposition modeling (FDM)/fused filament fabrication (FFF) [4], which is based on the extrusion of a plastic filament/metal wire from the heated nozzle. Other popular techniques are stereolithography (SLA)/digital light processing (DLP) [5] and selective laser sintering (SLS)/selective laser melting (SLM) of metallic powders [6] bonded with successive layers of fluid resin and powder, respectively.

AM is developing quickly and promises to make significant advances in the future. Researchers and industrialists are concentrating their efforts on the development of new techniques and applications in the area of electronics [7], [8], automobiles [9], and medical devices [10], [11]. One area of special interest is in the flexible and rapid prototyping of antenna and microwave components [12]-[14]. Figure 1.1 shows the growth areas of 3DP in a variety of industries. 3DP is expected to develop rapidly and substantially in the future of manufacturing. Specifically, the aerospace and automotive areas have increased explosively in the coming future. Figure 1.2 presents the future of 3DP materials. Although there are different outlooks for each industry, the market for 3DP metal materials has high growth potential.

3D Printed Part Market Grows to $8.4 Billion in 2025
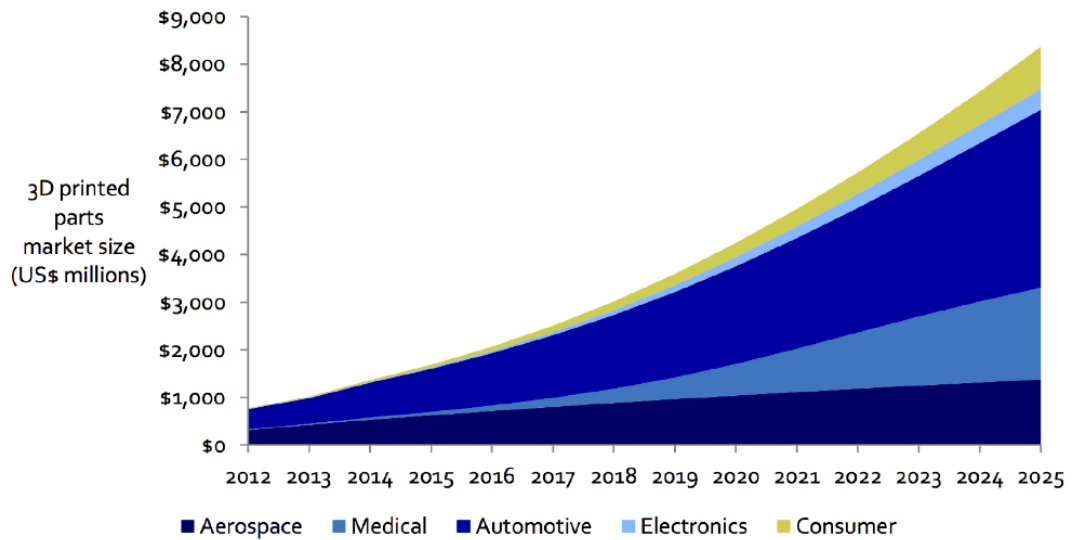
Figure 1.1 The growth of 3D printed part market [20]

The development of new materials and conductive inks has also been one of the main motivations for this trend. Inkjet printing technology with silver nanoparticle conductive inks has advanced very rapidly in recent years [15], [16]. This allows for the easy fabrication and prototyping of electronics and sensors on various substrates. These conductive inks have been specially formulated to work with industrial printers and, more recently [16], with standard home inkjet printers. Inkjet printing is a digital direct-write technique that provides the advantages of speed and accuracy to the fabrication process at a relatively low cost. The droplets of the conductive inks ejected from a heated nozzle are directly deposited at the specified position on functional materials to form electronic patterns. In the RF and microwave design area, it is desirable to integrate the electronics circuits and devices with antennas using flexible materials [17]-[19].

In general, 3DP may be a viable solution if the structures contain complex geometrical features and their properties are sufficiently novel or unusual to justify the extra cost involved.
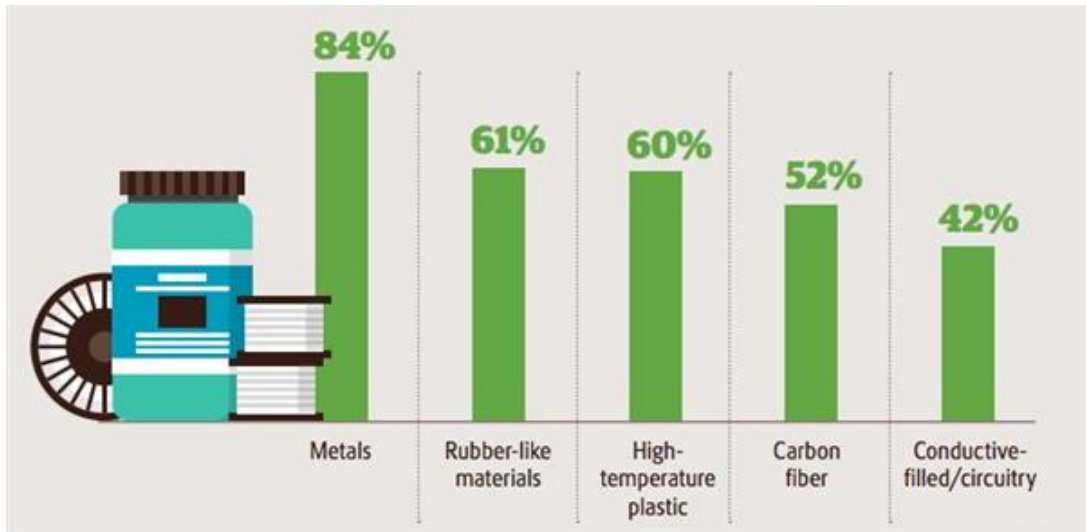
Figure 1.2 The future of 3D printing materials [21]

1.2 Research Objectives and Contributions

Complicated high-precision antennas cannot be fabricated easily using conventional lithographic technology. As mentioned in Section 1.1, AM technology is more functional and suitable for expanding the possibilities of antenna design. The primary purpose of this work is to present the potential applicability of AM in the field of antenna engineering. In this work, multiple antenna configurations with different shapes, different feed lines, and different frequencies are used as the basis for developing 3D printed electromagnetic structures. Antennas are fabricated using commercial or desktop 3D printers and different AM technologies for the various substrates. In addition, the metalized antenna patterns on the 3D printed dielectric substrates are achieved using various methods, including silver conductive ink. The surface roughness of the antenna patterns and the substrates are also presented and analyzed in this work. Finally, antenna performance is investigated and compared with that of antennas fabricated by the conventional etching process.

The main contributions from this work are:

(1) AM has been proven to be suitable for the development and fabrication of 3D fractal antennas. Its main advantage is that significant material reduction can be achieved using Sierpinski fractals or similar structures, potentially reducing costs of manufacturing while retaining good mechanical strength. The performance of the antenna is summarized through simulations and experimental results.

(2) The applicability of inexpensive AM technologies to the development of a non-planar electromagnetic structure for antenna applications has been described. A relatively simple structure consisting of metallic patches with trenches has been used for this demonstration. This technique could be applied to more complex 3D electromagnetic structures.

(3) Antennas suitable for integration with low-cost inkjet printing electronics on disposable paper drones have been demonstrated. This has been proven to be an inexpensive and fast method with sufficient printed quality for this application. The fabricated antennas have acceptable performance for efficient communication between the plane and a remote controller.

(4) Combining SLA and inkjet printing has been demonstrated to be suitable for the manufacturing of GPS antennas. The output from the SLA machine is sufficiently smooth to allow the deposition of metallic layers using inkjet printing technology. The inkjet printing process employing silver ink seems to be ideal for this application. The advantage of the fabrication method is the use of low-cost machines that are more suitable for home and office use.

(5) The application of AM to the development of WLAN antennas for a customized wrist worn application has been demonstrated. The last process uses a single machine to fabricate both the bracelet and then the metallic layers using a direct-write system with silver conductive ink. The diversity of the wrist-worn antenna system is developed for the final processes. This work demonstrates that inexpensive open-source machines can be used as an alternative for the 3D printing of antennas.

1.3 Publications arising from this work

- Journal papers

[1] **S. Jun,** A. Elibiary, B. Sanz-Izquierdo, D. Bird and A. McCleland, "3D Printing of Conformal Antennas for Diversity Wrist Worn Applications," submitted to *IEEE Transactions on Components, Packaging and Manufacturing Technology (Conditionally Accepted)*

[2] **S. Jun,** B. Sanz-Izquierdo, D. Bird, and A. McClelland, "Investigation of Antennas integrated into Disposable Unmanned Aerial Vehicles," submitted to *IEEE Transactions on Vehicular Technology (Under major revision)*

[3] **S. Jun,** B. Sanz-Izquierdo, and E.A Parker, "Liquids sensor/detector using an EBG structure," submitted to *IEEE Transactions on Antennas and Propagation (Under major revision)*

[4] **S. Jun**, B. Sanz-Izquierdo. E.A. Parker, D. Bird, A. McCleland, "Manufacturing considerations in the 3D printing of Fractal Antennas," *IEEE Transactions on Components, Packaging and Manufacturing Technology,* vol. 7, no. 11, pp. 1891-1898, Nov. 2017. *(Featured on the front cover)*

[5] **S. Jun**, B. Sanz-Izquierdo, J. Heirons, C. Mao, S. Gao, D. Bird and A. McClelland, "Circular polarised antenna fabricated with low-cost 3D and inkjet printing equipment", *Electronics Letters*, vol. 53, no. 6, pp. 370-371, 2017. *(Accompanied by a special invited feature article)*

[6] **S. Jun**, B. Sanz-Izquierdo and E. A. Parker, "3D printing technique for the development of non-planar electromagnetic bandgap structures for antenna applications," *Electronics Letters*, vol. 52, no. 3, pp. 175–176, Feb. 2016.

- Conference papers

[1] M.Fawaz, **S. Jun**, W.B.Oakey, C. Mao, A. Elibiary, B.Sanz-Izquierdo, D.Bird, A. McClelland, " 3D printed patch Antenna for millimeter wave 5G wearable applications," in *European Conference on Antennas and Propagation (EUCAP)*, London, UK, 2018.

[2] Ahmed Elibiary, W. Oakey, **S. Jun**, B. Sanz-Izquierdo, D.Bird, A.Mc.Clelland, " Fully 3D printed GPS Antenna using a Low-cost Open-source 3D Printer," in *Antennas & Propagation Conference (LAPC)*, 2017 Loughborough, Nov. 2017.

[3] **S. Jun**, B. Sanz-Izquierdo, E.A. Parker and J. Franco, "A Fractal Tetrahedron Antenna Fabricated using Metal 3D printing," in *2017 IEEE International Symposium on Antennas and Propagation (APSURSI)*, San Diego, California, USA, 2017.

[4] **S. Jun**, A. Shastri, B. Sanz-Izquierdo and A. McClelland, "Inkjet Printed Dual-Band Origami Frog Antenna," in *2017 IEEE International Symposium on Antennas and Propagation (APSURSI)*, San Diego, California, USA, 2017

[5] **S. Jun**, J. Heirons and B. Sanz-Izquierdo, "Inkjet printed dual band antenna for paper UAVs," in *2017 11th European Conference on Antennas and Propagation (EUCAP)*, Paris, France, 2017

[6] J. Heirons, **S. Jun**, A. Shastri, B. Sanz-Izquierdo, D. Bird, L. Winchester, L. Evans and A. McClelland," Inkjet Printed GPS antenna on a 3D Printed substrate using low-cost machines," in *Antennas & Propagation Conference (LAPC)*, 2016 Loughborough, Nov. 2016.

[7] A. Shastri, **S. Jun**, B. Sanz-Izquierdo, H. Aldawas, Q. Ahmed and M.Sobhy "Evaluation of a Low-Cost Inkjet Printed Slot Antenna for Energy Harvesting Applications" in *Antennas & Propagation Conference (LAPC), 2016 Loughborough* , Nov. 2016.

[8] B. Sanz-Izquierdo, **S. Jun**, J. Heirons, N. Acharya and T.B. Baydur, " Inkjet Printed and Folded LTE Antenna for Vehicular Application," in *Proc. 46th EuMC*, London, UK, 3-7 Oct. 2016.

[9] B. Sanz-Izquierdo, **S. Jun** and T. B. Baydur, "MIMO LTE vehicular antennas on 3d printed cylindrical forms," *Wideband and Multi-Band Antennas and Arrays for Civil, Security & Military Applications*, London, 2015.

[10] **S. Jun**, B. Sanz-Izquierdo, and M. Summerfield, "UWB antenna on 3D printed flexible substrate and foot phantom," *Antennas & Propagation* Conference (LAPC), *2015 Loughborough* , Nov. 2015.

[11] **S. Jun**, B. Sanz-Izquierdo, "A CPW-fed antenna on 3D printed EBG substrate," *Antennas & Propagation Conference (LAPC), 2015 Loughborough* , Nov. 2015.

[12] B. Sanz-Izquierdo, **S. Jun**, "WLAN antenna on 3D printed bracelet and wrist phantom," *Antennas and Propagation Conference (LAPC), 2014 Loughborough* , Nov. 2014.

1.4 Thesis Outline

The organization of this thesis is as follows:

Chapter 2 presents a brief summary of the additive manufacturing processes. The popular AM processes are reviewed, and their applications for antenna and microwave components are discussed in this section.

Chapter 3 presents the use of AM techniques for the fabrication of 3D fractal monopole antennas. The 3DP of three-dimensional designs based on the Sierpinski fractal concept is studied and its performance is discussed. AM allows for the fabrication of the sophisticated features of these antennas. The AM technique employed is metal powder binder printing, which jets a binding material onto a powder bed containing metal particles. Metal 3DP is ideal for maintaining the mechanical strength of the structures. The envisaged applications are in the defense and aerospace sectors, where high value, lightweight, and mechanically robust antennas may be integrated with other 3D printed parts.

Chapter 4 describes a novel procedure to detect liquids with different permittivity using an electromagnetic band gap (EBG) structure. The variation in the dielectric characteristics of the liquids inserted produces a change in the reflected phase of the EBG. This change in phase could be detected in various ways. Moreover, the use of 3D printing for the development of non-planar EBG structures for antenna applications is proposed in this chapter. Inexpensive FFF is used as the fabrication process. Silver-loaded conducting ink is employed for the metallic components of the EBG.

Chapter 5 discusses disposable paper drones integrated with antennas using inkjet printing technology. The antenna elements are directly printed onto a photo paper substrate using silver nanoparticle conductive ink. The substrate is then folded to create a paper drone. Low-cost desktop inkjet printing equipment is used to deposit the metallic tracks of the antenna, and all designs target the current frequency bands employed in the control and wireless communication of commercial drones (2.4 GHz and 5 GHz bands). The purpose of this work is to investigate potential antenna

scenarios for disposable drones which may one day be fully fabricated using inkjet printing technology.

Chapter 6 investigates the use of AM equipment for the development of circularly polarized (CP) antennas. CP patch antennas are fabricated using two AM processes, SLA and inkjet printing using silver inks. A widely available SLA printer is first employed for the layer-by-layer fabrication of the substrate, and then inkjet printing is used to deposit the metallic layers of the radiating element on the substrate. The excellent adhesion of the metallic patterns to the substrate is observed, and reasonably low resistance is achieved on the metallic surfaces. The aim is to demonstrate the use of alternative, inexpensive machines for the prototyping and manufacturing of antennas.

Chapter 7 presents for the first time the application of 3D printing techniques for the development of conformal antennas for diversity wrist worn wireless communications. Three processes are described with the common challenge of depositing the metallic layers of the antennas on a wristband fabricated using FFF. The first is a multistep process that combines adding a layer to smooth the surface of the band, a jetting process to deposit the metallic tracks, a flash curing system, and then an electroplating process. The second combines painting the metallic layers by hand and then an electroplating process. The last process uses a single machine to fabricate both the bracelet and then the metallic layers using a direct-write system with silver conductive ink. The wrist worn antennas are presented, and their performances on a human wrist are discussed. The diversity of the wrist-worn antenna system is developed for the final processes.

Chapter 8 presents the summarized conclusions of each chapter and suggests relevant future work.

References

[1] H. Lipson, M. Kurman, Fabricated: The new world of 3D printing, John Wiley & Sons, 2013.

[2] I. Gibson, D. W. Rosen, B. Stucker, Additive manufacturing technologies, Springer, 2010.

[3] T. T. Wohlers, Wohlers Report 2013: Additive Manufacturing and 3D Printing State of the Industry: Annual Worldwide Progress Report, Wohlers Associates, 2013.

[4] P. Dudek, "FDM 3D printing technology in manufacturing composite elements," Arch. Metall. Mater., vol. 58, no. 4, pp. 1415–1418, Dec. 2013.

[5] J. Maas, B. Liu, S. Hajela, Y. Huang, X. Gong, and W. J. Chappell, "Laser-based layer-by-layer polymer stereolithography for high frequency applications," Proc. IEEE, vol. 105, no. 4, pp. 645–654, Apr. 2017.

[6] O. A. Peverini et al., "Selective Laser Melting Manufacturing of Microwave Waveguide Devices," in Proceedings of the IEEE, vol. 105, no. 4, pp. 620-631, April 2017.

[7] E. Macdonald, R. Salas, D. Espalin, M. Perez, E. Aguilera, D. Muse and R. Wicker, "3D Printing for the Rapid Prototyping of Structural Electronics", IEEE Access, vol. 2, pp. 234-242, 2014.

[8] A. J. Lopes, E. MacDonald, and R. B. Wicker, "Integrating stereolithography and direct print technologies for 3D structural electronics fabrication," Rapid Prototyping J., vol. 18, no. 2, pp. 129–143, 2012.

[9] T. Ketterl, Y. Vega, N. Arnal, J. Stratton, E. Rojas-Nastrucci, M. Cordoba-Erazo, M. Abdin, C. Perkowski, P. Deffenbaugh, K. Church and T. Weller, "A 2.45 GHz Phased Array Antenna Unit Cell Fabricated Using 3-D Multi-Layer Direct Digital Manufacturing", IEEE Transactions on Microwave Theory and Techniques, vol. 63, no. 12, pp. 4382-4394, 2015.

[10] A. Cloonan, D. Shahmirzadi, R. Li, B. Doyle, E. Konofagou and T. McGloughlin, "3D-Printed Tissue-Mimicking Phantoms for Medical Imaging and Computational Validation Applications", 3D Printing and Additive Manufacturing, vol. 1, no. 1, pp. 14-23, 2014.

[11] F.P.W. Melchels, J. Feijen and D.W. Grijpma, "A review on stereolithography and its applications in biomedical engineering", Biomaterials, Vol. 31, pp. 6121–6130, 2010.

[12] B. Sanz-Izquierdo and E. A. Parker, "3D printing technique for fabrication of frequency selective structures for built environment," Electron. Lett., vol. 49, no. 18, pp. 1117–1118, Aug. 2013.

[13] R. Zhu, G. Lipworth, T. Zvolensky, D. R. Smith, and D. L. Marks, "Versatile manufacturing of split-block microwave devices using rapid prototyping and electroplating," IEEE Antennas Wireless Propag. Lett., vol. 16, pp. 157–160, 2017.

[14] X. Shang et al., "W-band waveguide filters fabricated by laser micromachining and 3-D printing," IEEE Trans. Microw. Theory Techn., vol. 64, no. 8, pp. 2572–2580, Aug. 2016.

[15] S. Khan, R. Dahiya, and L. Lorenzelli, "Technologies for printing sensors and electronics over large flexible substrates: A review," IEEE Sensors J., vol. 15, no. 6, pp. 3164–3185, Jun. 2015.

[16] Y. Kawahara et al., "Instant Inkjet Circuits: Lab-Based Inkjet Printing to Support Rapid Prototyping of UbiComp Devices," Proc. 2013 ACM Int'l Joint Conf. Ubiquitous Computing (UbiComp 13), pp. 363–372, 2013.

[17] G. McKerricher, J. Gonzalez and A. Shamim, "All inkjet printed 3D microwave capacitors and inductors with vias," 2013 IEEE MTT-S International Microwave Symposium Digest (MTT), Seattle, WA, 2013, pp. 1-3.

[18] J. Mei, M. Lovell, M. Mickle, "Formulation and processing of novel conductive solution inks in continuous inkjet printing of 3-D electric circuits", IEEE Trans. Electron. Packag. Manuf., vol. 28, no. 3, pp. 265-273, Jul. 2005.

[19] L. Yang, A. Rida, R. Vyas, and M. M. Tentzeris, "RFID tag and RF structures on a paper substrate using inkjet-printing technology," IEEE Trans. Microw. Theory Tech., vol. 55, no. 12, pp. 2894–2901, Dec. 2007.

[20] Lux Research, Inc. [online]: http://www.luxresearchinc.com/ (Accessed Aug. 2017).

[21] 3D Printing & 3Ders [online]: https://www.3ders.org/ (Accessed Aug. 2017).

CHAPTER 2.

LITERATURE REVIEW AND BACKGROUND

2.1 Introduction

This chapter reviews the previous work on additive manufacturing (AM) or 3D printing (3DP) technology and its application to antenna and microwave engineering. The 3DP has attracted considerable attention and led to many AM applications [1]-[4]. It provides rapid prototyping, allowing complex 3D solid object/models to be built quickly and cost-efficiently with a high degree of design freedom. In particular, 3DP enables depositing material by layers to fabricate a structure from the digital 3D design model, and a wide range of plastic, resin, metal, and composite materials have been employed for AM processes. Several specific technologies are described, including filament, resin, and powder-based 3DP. The process has been applied in various fields, including bioprinting [5], health monitoring [6], medical robotics [7], and structural electronics [8].

Inkjet printing technology has been recently developed for AM processes. This provides direct printing of patterns on substrates through droplets ejected from a nozzle, and is the key technology to enable printed electronics [9]-[11]. Consequently, many studies have reported electronic devices fabricated using this technology. Most studies have used planar, uniform, and thin sheets made of cellulose or polyethylene terephthalate (PET). A recent advance in semiconductor layers has been to fully inkjet-printed electronics [12], [13], and inkjet-printed components have been applied in biomedical [14], sensor [15], pharmaceutical [16], and micro-electro-mechanical systems (MEMS) [17] fields.

Popular AM processes are reviewed in Section 2.2, and AM applications for antenna and microwave components are discussed in Section 2.3.

2.2 Additive Manufacturing Process

Many different AM or 3DP processes are employed to create 3D solid object/models. The desired objects are created by depositing layers of the selected materials through the different fabrication processes. The most popular materials are plastic or polymer filaments for fused deposition modelling (FDM), photosensitive resin for stereolithography (SLA), and powdered metal or plastics for selective laser melting (SLM). Figure 2.1 shows a typical, generalized, AM process. The original model is typically created by 3D computer-aided design (CAD) software, then exported to the 3D printer. Almost all AM technology uses STL file format, and most machines then build the 3D model using machine specific software, forming each layer from the selected materials. Some objects with complex geometry require additional materials for support structures and subsequent manual attention to remove them to finalize the 3D model. After printing, there are sometimes post processing stages, such as drying, polishing, electroplating, and coating for specific application purposes. Thus, AM provides various advantages to enable manufacturing cost efficient, flexible, and sophisticated objects that can be applied to diverse applications.

CAD Model - 3D Model

| 3D CAD Model | STL convert | File transfer to machine | Machine setup | Build | Remove | Post-process | Application |
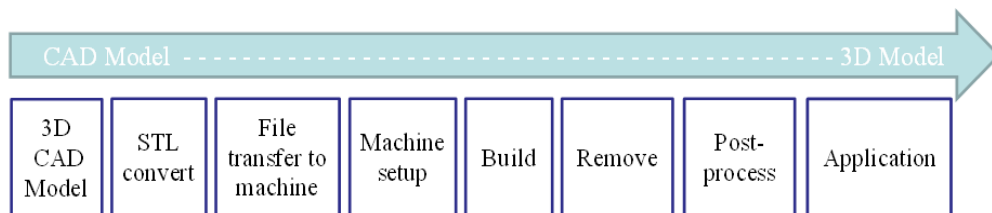
Figure 2.1 Generalized Additive Manufacturing Process [18]

2.2.1 Extrusion: Fused Deposition Modelling / Fused Filament Fabrication

The most commonly used 3DP process is fused deposition modelling (FDM), which is also called fused filament fabrication (FFF) [19]-[21]. This technology typically

works with low cost personal printers and plastic filaments for the home and office. The desired models are built by melted thermoplastic filaments on a printed bed. Figure 2.2 shows the typical FDM process. The filament is led to the extrusion head, which melts the filament using the appropriate temperature heated extrusion head. The melted filament is extruded and flows onto the build platform. The extrusion head is moved to the correct position on the build platform vertically and horizontally, and the heated filament material is deposited to build the model layer by layer. The process is repeated until the model is complete.
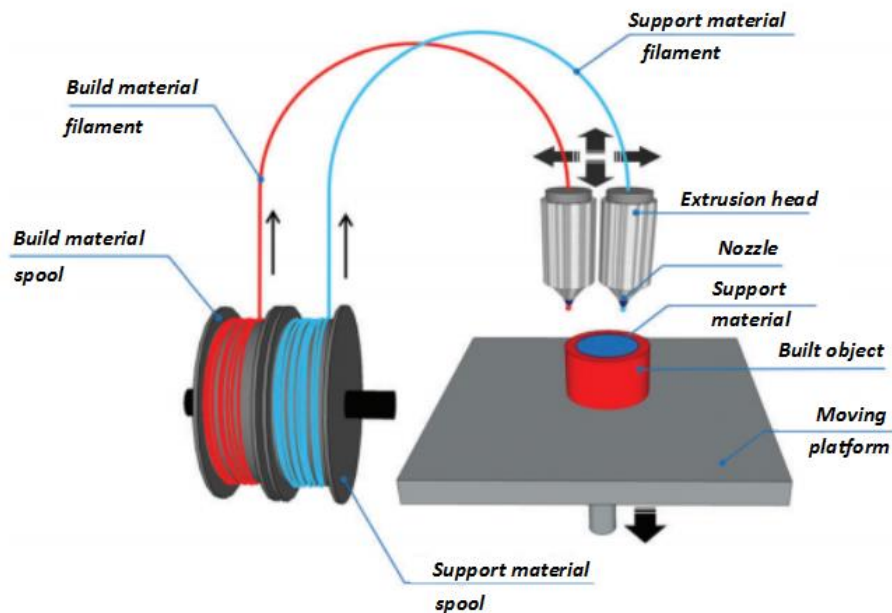
Figure 2.2 The structure of FDM process [19]

A variety of plastic filament materials are used for FDM, which might be specifically chosen for the model being constructed. Popularly used materials include polylactic acid (PLA), and acrylonitrile butadiene styrene (ABS). PLA is a highly biodegradable thermoplastic made from renewable materials including corn starch, sugar cane, and wood chips. The filament has a better environmental impact than most other filaments, and requires less energy for printing, with printer nozzle temperature generally in the range 190–230°C. Although a heated build platform is

probably not essential, generally 60–80°C is considered helpful for build quality. The other common filament material (ABS) is commonly used to print durable parts that can tolerate high temperatures. ABS is a ductile non-biodegradable petroleum based plastic, somewhat less fragile and flexible than PLA. However, the surface quality of the printed model is rougher than other materials. Printers using ABS filament typically operate with at 210–250°C print nozzle and 80–110°C build platform. Nozzle diameter is also determined by the size of the extruded filaments. PLA and ABS filaments for 3DP are commercially available at 1.75 mm and 3 mm diameter.

2.2.2 Resin: Stereolithography / Digital Light Processing

Stereolithography (SLA) and digital light processing (DLP) technologies use liquid photosensitive resin as the principal 3DP material in contrast to the plastic filament materials of FDM and FFF [22]-[24]. These systems employ photopolymerization to convert the liquid material to a solid object using a suitable light source. Figure 2.3 shows the typical SLA and DLP processes. The SLA or DLP 3DP process commences with a model created by 3D CAD, and exported to the printer in STL or OBJ formats. Printing occurs in a large resin filled tank, which is changed to solid by selectively exposure to ultraviolet (UV) light. The initial layer is cured using UV light after the build platform is placed in the liquid resin tank, then the platform rises the height of a layer, and exposes the resin for the layer, which deposits on the preceding layer. The process is repeated until the 3D solid model is completed. There are slight differences between the SLA and DLP processes. SLA creates the model point by point using a laser beam, whereas DLP creates the model layer by layer using a digital projector screen [25].

The optical spot size of the laser beam or digital projector screen is tiny, and constitutes the primary factor for printing resolution. Therefore, these processes provide higher resolution 3D printed models than filament based 3D printers. They also provide smoother and higher quality model surfaces. However, SLA and DLP printing sometimes requires supports for printing, which must be removed in post processing, which somewhat restricts design freedom and requires more effort than FDM printing.
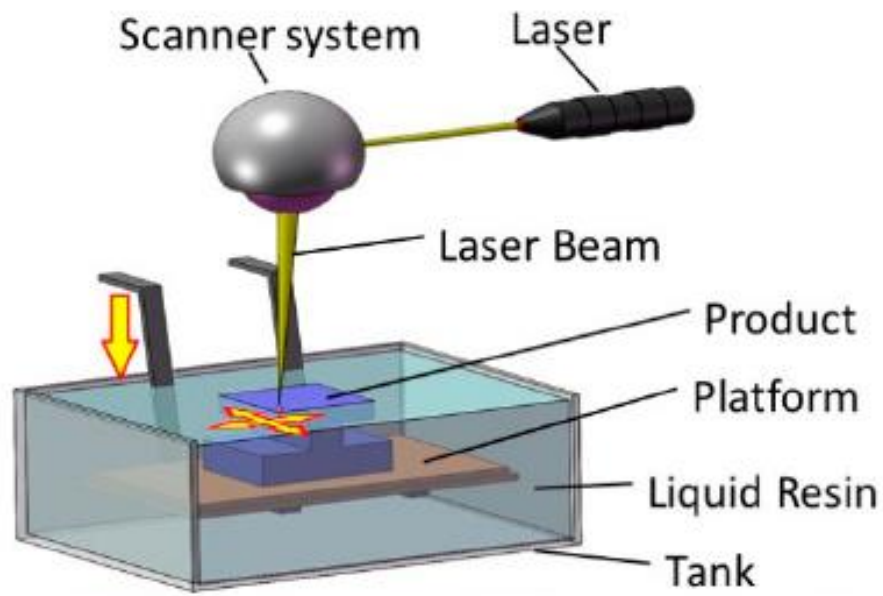
(a)
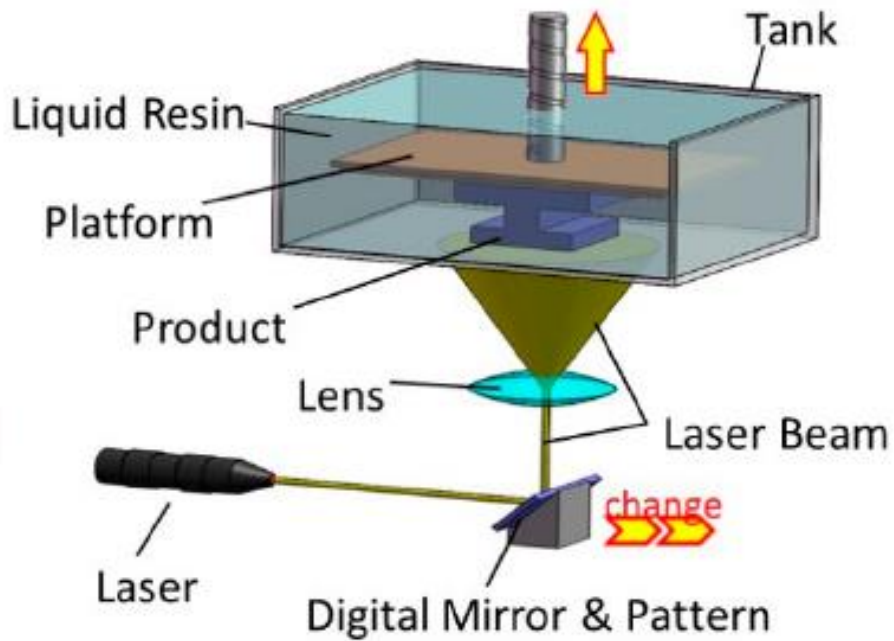
(b)

Figure 2.3 The illustration of (a) SLA and (b) DLP processes [22]

2.2.2 Powder: Selective Laser Sintering / Selective Laser Melting

Selective laser sintering (SLS) and selective laser melting (SLM) are primarily used for powder based 3D printers [26]-[29]. These printers use various materials, including metal, steel, and aluminum powder. SLS and SLM support fabricating complex parts better than extrusion (FDM and FFF) and resin (SLA and DLP) based 3DPs, and support structures are not required. Figure 2.4 shows the typical SLS and SLM process.
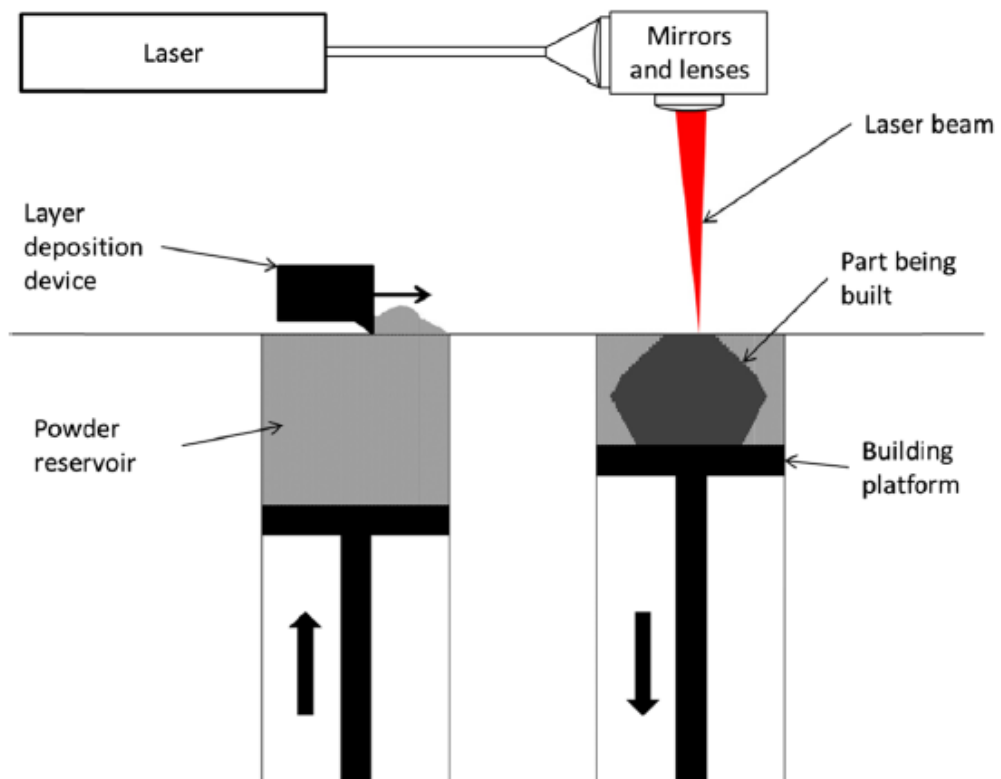
Figure 2.4 Schematics of SLS and SLM processes [28]

A 3D CAD model is transmitted to the powder based 3D printer, and the build platform increases each time by a layer of powder on a z axis. A roller in the 3D printer spreads out a layer of powder evenly. A laser beam heats the selected area of the layer and sinters the desired area. A layer of powder on the melting point is deposited by using a laser beam. The build platform goes down by a layer thickness

of the z axis, and a new layer of powder is spread over the surface of the previous layer. The new layer is attached above the last layer. This process is repeated layer by layer until the component is complete.

There are slight differences between these methods, powder is sintered in SLS but melted in SLM to form the solid structure. However, both processes can print entirely metal parts for prototyping or production, and neither requires support structures for printing. These advantages allow intricate geometric designs, and powder based AM processes have been used for automotive and aerospace components and medical applications.

2.2.4 Inkjet printing technology

Inkjet printing is a direct writing process without photomasks, and offers fundamental advantages of low cost, flexibility, and relatively simple principle steps constructed by photolithography. Inkjet printing provides the formation by placing ink droplets on a substrate under digital control [30]-[33], where the ink is deposited on particular regions of the substrates as additive patterns. Patterning resolution is typically from ten to one hundred microns [32]. Thus, inkjet printing is rapidly expanding for patterning technologies onto flexible substrates, providing flexible printed electronics devices, such as displays, sensors, semiconductors, and MEMS circuits.

Figure 2.5 shows the typical working process of drop-on-demand (DOD) inkjet printing. The ink droplets are ejected from the printing nozzle into 2D and 3D structures. This noncontact process uses movement of the ink droplets and substrates to form the structural patterns.
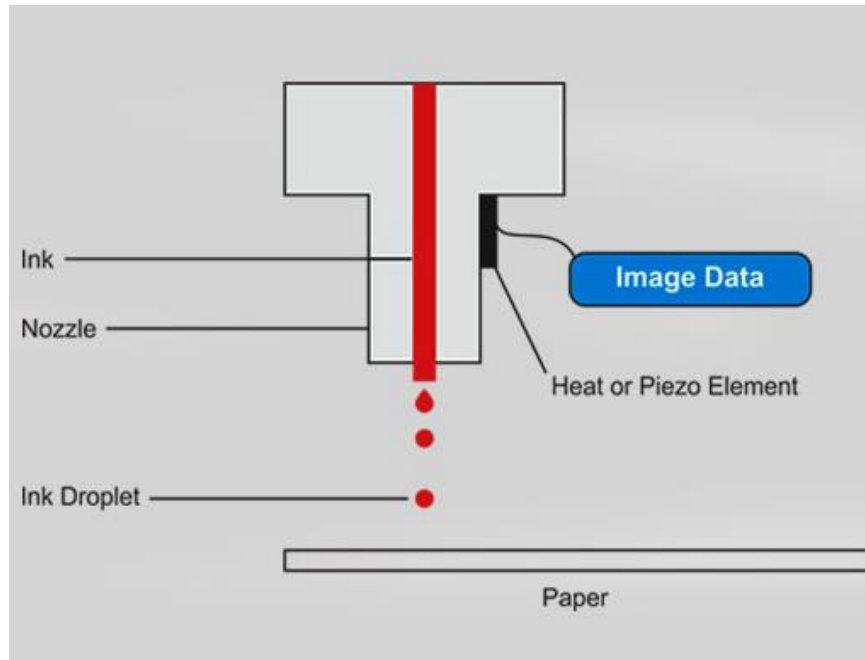
Figure 2.5 An illustration of the inkjet printing technology [33]

A range of functional inks have been developed and deposited on a wide range of substrate materials using inkjet printing. The trace patterns are designed using CAD software and directly printed onto the substrates. This provides significantly reduced time and material consumption for printing. Recent inkjet printing research offers promising potential for fabricating printed electronics, sensors, and biomedical applications.

2.3 Additive Manufacturing for Antenna and Microwave Applications

Recent studies have shown potential AM or 3DP applications for antenna and microwave engineering. Complicated 3D structures are typically generalized by CAD systems and fabricated layer by layer. The AM or 3DP technologies show potential to produce cost and time efficient complex geometrical antenna and microwave components for microwave, millimeter wave (mm-wave), and terahertz (THz) frequencies.

2.3.1 Filament Based Materials

The advent of 3DP has allowed fabrication of arbitrarily complex antenna structures. Metallic structures on dielectric substrates are accomplished by integration of FDM with thermoplastic filaments and micro-dispensing of conductive inks. Frequency selective structures using 3DP triple cross dipoles for long wavelengths have been proposed [34], [35], based on fully and partially metalizing 3DP shapes, as shown in Figure 2.6. These were manufactured using FDM with a personal 3D printer. Nonplanar electromagnetic band gap structures have been prototyped by combining FDM and silver conductive paint [36].
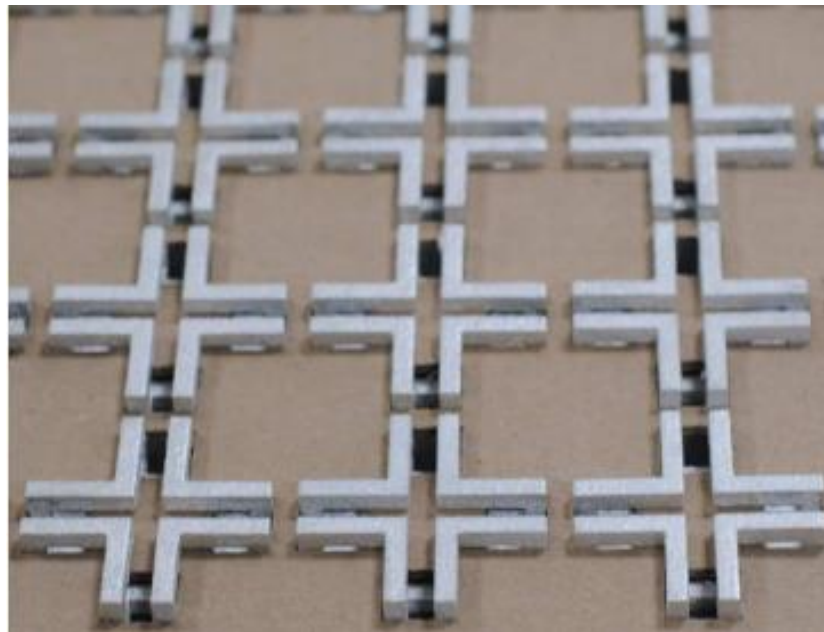
Figure 2.6 A 3x3 array of the 3-D folded loop FSS [34]

Metal pipe rectangular waveguides [37] have been fabricated by FDM 3DP, as shown in Figure. 2.7. The lower frequency (X band) waveguide structure was printed layer by layer using nonconductive plastic filament then surface electroplated. The 3D printed patch antenna on the embedded wire mesh was fabricated in [38]. The flexibility of conductors and dielectrics onto the complex 3D printed surface can be applied for new types of 3D microwave applications. Dipole and coplanar waveguide fed ultrawideband antennas have been tested using 3DP onto phantom with human tissue liquid for wearable applications [39] ,[40].
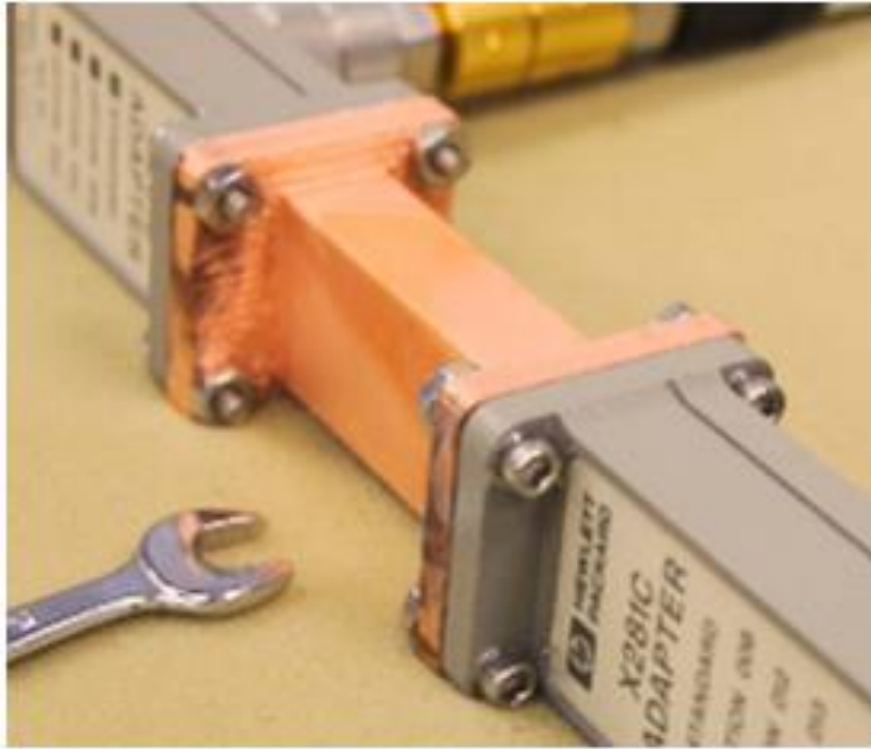
Figure 2.7 FDM 3-D printed and copper-plated WR-90 [37]

2.3.2 Resin Based Materials

Silver plated WR-10 waveguides have been fabricated by 3DP using digital light projection stereolithography (DLP-SLA) [41]. This DLP-SLA printing and silver electroless plating system has also been demonstrated for mm-wave components due to the high native printing resolution and successful metallization of the waveguide interior and exterior. 3D printed cube antennas have been studied and fabricated for wireless sensor applications [42]. Moreover, the small 3D printed cube antenna has been extended to realize the integrated wireless devices. Figure 2.8 shows how these antennas were fabricated using SLA 3DP, compared with conventional PCB fabrication method.
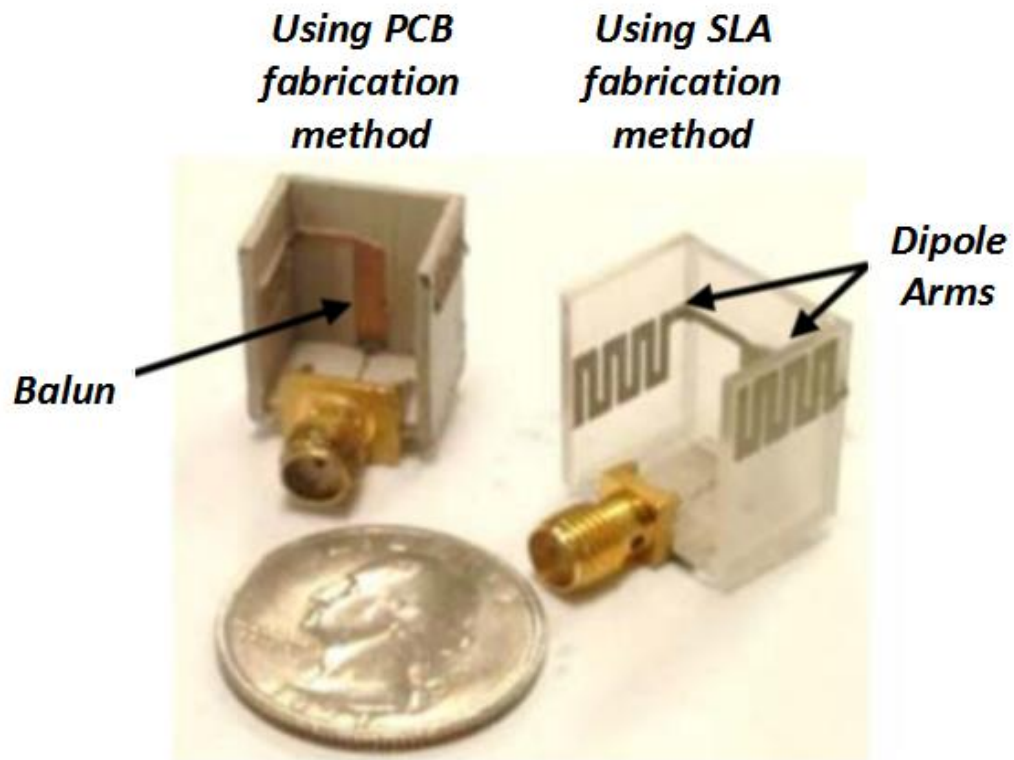
Figure 2.8 The fabricated cube antennas [42]

Antenna substrates have been modified and investigated for local control of effective relative permittivity [43]. The customized value of effective relative permittivity is determined by air cavity size and spacing in the various substrates. 3DP for lightweight X band waveguide bandpass filters has been recently developed in [44]. A filter based on spherical resonators was fabricated by SLA 3DP, and then coated with 25 μm copper layers on the surface. Figure. 2.9 shows the illustration of the filter before and after plating.
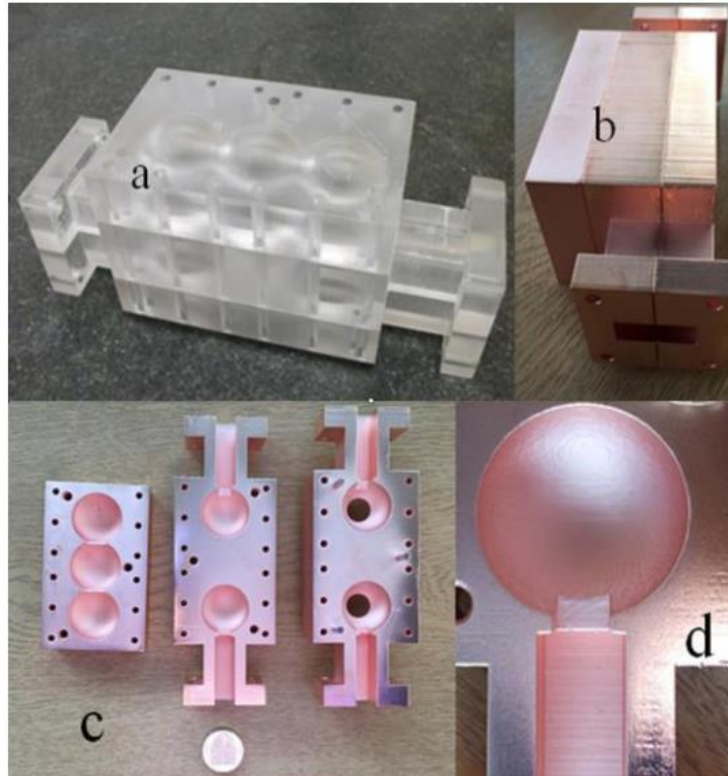
Figure 2.9 Fabrication of the SLA 3D printed filter before and after plating. (a) Before plating; (b) and (c) after plating; (d) zoom view of one spherical resonator [44]

2.3.3 Powder Based Materials

Developments in powder based 3DP have demonstrated complex design freedom and reduced material volume for RF and microwave components, enabling direct manufacture of 3D structures. Complex 3DP volcano smoke antennae have been proposed in [45]. The ultrawideband volcano smoke antenna has been fabricated using SLM, and then electroplated, as shown in Figure. 2.10. In other words, the antenna was manufactured directly using steel powder and electroplated with copper to improve conductivity.

Figure 2.10 SLM 3D printed volcano smoke antenna [45]

Recently, the surface roughness of 3DP horn antennas have been evaluated in [46]. As shown in Figure 2.11, the two 3DP horn antennas were directly manufactured from metal powder using electron beam melting (EBM) and compared with a standard gain horn antenna provided by Pasternack.
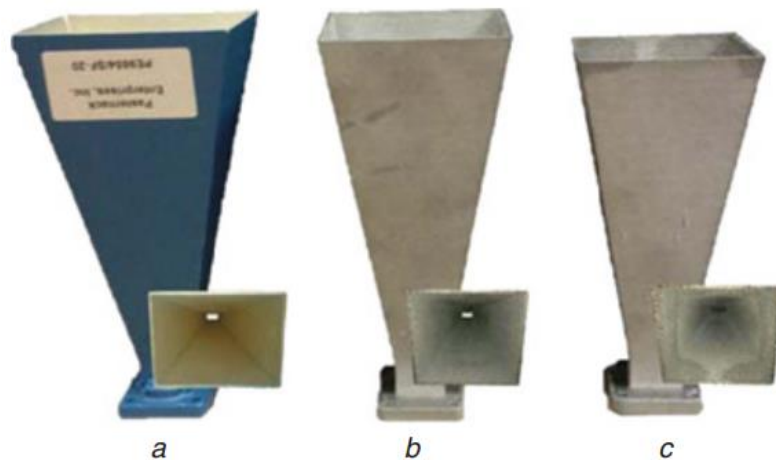
Figure 2.11 Photographs of horn antennas (a) reference horn (b) 3D printed horn 1 (c) 3D printed horn 2 [46]

An electrically small folded spherical helix antenna and spherical zigzag antenna were also 3D printed and metalized in [47]. Both antennas were fabricated using selective laser sintering (SLS) and coated with polycrystalline copper. All 3D printed antennas and microwave components provided acceptable performance, including resonant frequency, bandwidth, and radiation characteristics.

2.3.4 Inkjet Based Materials

Development of nanoparticle silver inks for inkjet printing technology has also advanced very rapidly in recent years. Rapid prototyping of UbiComp devices on paper and plastic films have been produced using instant inkjet printed circuits [48], and sensors and electronics have been printed on flexible substrates [49]. Inkjet printing technology has been applied to fabricate frequency selective surfaces (FSS) in [50]. Novel wideband and high gain antennas on paper substrates have been manufactured in [51]. RF energy harvesting and power transmission devices have been also deposited on paper substrates in [52].

Inkjet printing of antennas has also been proposed on a variety of substrates. A flexible inkjet printed broadband UHF radio frequency identification (RFID) tag on liquid crystal polymer (LCP) substrate was developed for sensing applications [53]. A multilayer mm-wave yagi-uda antenna and proximity fed patch arrays on flexible substrates have been proposed using purely additive inkjet printing technology [54], [55]. Figure 2.12 shows the inkjet printed yagi-uda antenna. The antenna was fabricated using single-platform inkjet printing utilizing dielectric substrates and metal nanoparticle inks. A compact inkjet printed ultrawideband antenna on a kapton polyimide substrate has been used for flexible and wearable electronics [56]. A monopole antenna on paper substrates for wireless communication is presented in [57], and phased-array antennas have been realized by inkjet printed barium strontium titanate (BST) thick films [58].

Figure 2.12 Inkjet-printed Yagi–Uda antenna [54]

Fabrication methods for printing plastic and metallic layers have been recently combined to develop RF harvesting sensors [59], and 3D origami RF systems have been fabricated by combined fully 3DP techniques including conductive layers. Figure 2.13 shows inkjet printed patch antennas on unfolded and folded 3D printed form. Inkjet printing technology has demonstrated the feasibility of 3DP for complex structures using low cost, simple, fast, and eco-friendly processes. The methodology has many electromagnetic applications, including antenna and microwave components.
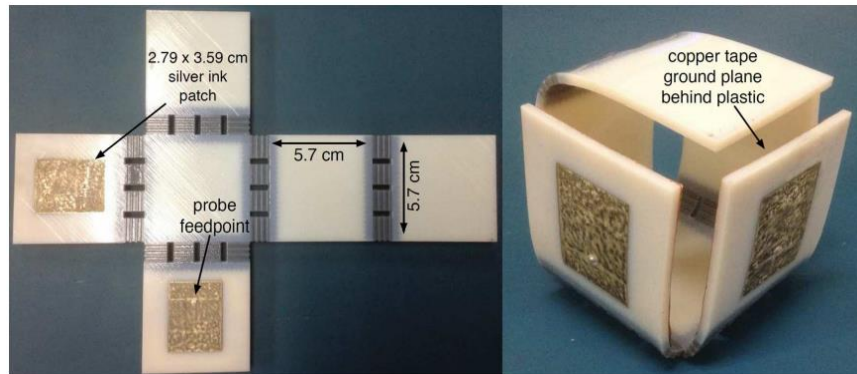
Figure 2.13 Inkjet-printed patch antennas on unfolded (left) and folded (right) 3D-printed cube [59]

Table 2.1 presents a comparison of the three AM methods that are most-used in equipment: FDM, SLA, and SLM. 3D printers are widely used for product development because of the low cost, time-saving, and design freedom. FDM printers are low-cost consumer machines with low material costs. However, their levels of accuracy and detail are poor. SLA printers are based on resin and have higher accuracy and produce smoother surfaces compared to FDM printers. However, there is a limited choice of resins for SLA printers and the printed structures are sensitive to UV light exposure. Moreover, SLA printers are more expensive than FDM printers. Compared to FDM and SLA printers, SLS printers do not require support structures to produce complicated objects because the powder acts as a self-supporting material and provides strong functional parts. However, the cost of the machines is quite high and the range of materials is for SLS printers limited.

TABLE 2.1

COMPARISON OF ADDITIVE MANUFACTURING METHODS USED IN EQUIPMENT

	FDM	*SLA*	*SLS*
Machine model	Ultimaker 2+ [60]	Form 2 [61]	Fuse 1 [61]
Material	PLA, ABS	Resin	Powder
Layer thickness	0.2 mm	0.02 mm	100 µm
Build Speed	30–300 mm/s	10–30 mm/hour	10 mm/hour
Build Volume	$223 \times 223 \times 205$ mm	$145 \times 145 \times 175$ mm	$677 \times 668 \times 1059$ mm
File types	.STL, .OBJ, .X3D, and .3MF	.STL and .OBJ	.STL and .OBJ
Price	£1,790	£3,360	£10,679

References

[1] J. Kietzmann, L. Pitt, and P. Berthon, "Disruptions, decisions, and destinations: Enter the age of 3-D printing and additive manufacturing," Business Horizons, vol. 58, pp. 209-215, 2015/03/01/ 2015.

[2] N. Crane, J. Tuckerman, and G. N. Nielson, "Self-assembly in additive manufacturing: Opportunities and obstacles," Rapid Prototyping J., vol. 17, no. 3, pp. 211–217, 2011.

[3] S. Upcraft and R. Fletcher, "The rapid prototyping technologies," Assembly Autom., vol. 23, pp. 318–330, Jan. 2012.

[4] G. C. Anzalone, C. Zhang, B. Wijnen, P. G. Sanders, and J. M. Pearce, "A Low-Cost Open-Source Metal 3-D Printer," IEEE Access, vol. 1, pp. 803-810, 2013.

[5] J. Shi, L. Zhu, Z. Li, J. Yang, and X. Wang, "A Design and Fabrication Method for a Heterogeneous Model of 3D Bio-Printing," IEEE Access, vol. 5, pp. 5347-5353, 2017.

[6] L. Fang, T. Chen, R. Li, and S. Liu, "Application of Embedded Fiber Bragg Grating (FBG) Sensors in Monitoring Health to 3D Printing Structures," IEEE Sensors J., vol. 16, pp. 6604-6610, 2016.

[7] T. K. Morimoto and A. M. Okamura, "Design of 3-D Printed Concentric Tube Robots," IEEE Trans. Robot., vol. 32, pp. 1419-1430, 2016.

[8] E. Macdonald, R. Salas, D. Espalin, M. Perez, E. Aguilera, D. Muse, and R. B. Wicker, "3D Printing for the Rapid Prototyping of Structural Electronics," IEEE Access, vol. 2, pp. 234-242, 2014.

[9] C. Sternkiker, E. Sowade, K. Y. Mitra, R. Zichner, and R. R. Baumann, "Upscaling of the Inkjet Printing Process for the Manufacturing of Passive Electronic Devices," IEEE Trans. Electron Devices, vol. 63, pp. 426-431, 2016.

[10] B. J. Kang, C. K. Lee, and J. H. Oh, "All-inkjet-printed electrical components and circuit fabrication on a plastic substrate," Microelectron. Eng., vol. 97, no. 4023, pp. 251–254, 2012.

[11] S. M. Bidoki, J. Nouri, and A. A. Heidari, "Inkjet deposited circuit components," J. Micromech. Microeng., vol. 20, no. 5, p. 055023, 2010.

[12] B. A. Ridley, B. Nivi, and J. M. Jacobson, "All-inorganic field effect transistors fabricated by printing," Science, vol. 286, pp. 746–749, 1999.

[13] K. E. Paul, W. S. Wong, S. E. Ready, and R. A. Street, "Additive jet printing of polymer thin-film transistors," Appl. Phys. Lett., vol. 83, no. 10, pp. 2070–2072, 2003.

[14] M. Choi, J. Heo, M. Yang, and J. Hong, "Inkjet Printing-Based Patchable Multilayered Biomolecule-Containing Nanofilms for Biomedical Applications," ACS Biomaterials Science & Engineering, vol. 3, pp. 870-874, 2017/06/12 2017.

[15] J. Li, F. Rossignol, and J. Macdonald, "Inkjet printing for biosensor fabrication: combining chemistry and technology for advanced manufacturing," Lab on a Chip, vol. 15, pp. 2538-2558, 2015.

[16] R. D. Boehm, P. R. Miller, J. Daniels, S. Stafslien, and R. J. Narayan, "Inkjet printing for pharmaceutical applications," Materials Today, vol. 17, pp. 247-252, 2014/06/01/ 2014.

[17] S. B. Fuller, E. J. Wilhelm, and J. M. Jacobson, "Ink-jet printed nanoparticle microelectromechanical systems," J. MEMS, vol. 11, no. 1, pp. 54–60, 2002.

[18] I. Gibson, D. Rosen, and B. Stucker. (2015). Additive manufacturing technologies : 3D printing, rapid prototyping, and direct digital manufacturing.

[19]   J. P. Kruth, M. C. Leu, T. Nakagawa, "Progress in Additive Manufacturing and Rapid Prototyping", CIRP Annals - Manufacturing Technology, Vol. 47, Issue. 2, 1998, PP. 525-540.

[20]   S. Song, A. Wang, Q. Huang, and F. Tsung, "Shape deviation modeling for fused deposition modeling processes," in 2014 IEEE International Conference on Automation Science and Engineering (CASE), 2014, pp. 758-763.

[21]   K. Tong, S. Joshi, E. A. Lehtihet, "Error compensation for fused deposition modeling (fdm) machine by correcting slice files", Rapid Prototyping Journal, vol. 14, no. 1, pp. 4-14, 2008.

[22]   Y. Xu, X. Wu, X. Guo, B. Kong, M. Zhang, X. Qian, S. Mi, and W. Sun, "The Boom in 3D-Printed Sensor Technology," Sensors, vol. 17, p. 1166, 2017.

[23]   B. C. Gross, J. L. Erkal, S. Y. Lockwood, C. Chen, and D. M. Spence, "Evaluation of 3D Printing and Its Potential Impact on Biotechnology and the Chemical Sciences," Analytical Chemistry, vol. 86, pp. 3240-3253, 2014/04/01 2014.

[24]   Hull, C.W. Apparatus for Production of Three-Dimensional Objects by Stereolithography. U.S. Patent 4575330, 11 March 1986.

[25]   [online]: https://formlabs.com/blog/3d-printing-technology-comparison-sla-dlp/ (Accessed August. 2017).

[26]   P. Bertrand, F. Bayle, C. Combe, P. Goeuriot, and I. Smurov, "Ceramic components manufacturing by selective laser sintering," Applied Surface Science, vol. 254, pp. 989-992, 2007.

[27]   E. Juste, F. Petit, V. Lardot, and F. Cambier, "Shaping of ceramic parts by selective laser melting of powder bed," Journal of Materials Research, vol. 29, no. 17, pp. 2086–2094, 2014.

[28]   L. Ferrage, G. Bertrand, P. Lenormand, D. Grossin, and B. Ben-Nissan, "A review of the additive manufacturing (3DP) of bioceramics: alumina, zirconia (PSZ) and hydroxyapatite," Journal of the Australian Ceramic Society, vol. 53, pp. 11-20, April 01 2017.

[29]   J. P. Kruth, G. Levy, F. Klocke, and T. H. C. Childs, "Consolidation phenomena in laser and powder-bed based layered manufacturing," CIRP Annals, vol. 56, pp. 730-759, 2007/01/01/ 2007.

[30]   K. Hon, L. Li, and I. Hutchings, "Direct writing technology—Advances and developments," CIRP Annals - Manufacturing Technology, vol. 57, no. 2, pp. 601-620, 2008.

[31]   M. Singh, H. M. Haverinen, P. Dhagat, and G. E. Jabbour, "Inkjet Printing Process and Its Applications," Adv. Mater., vol. 22, no. 6, pp. 673-685, 2010.

[32]   T. Kawase, S. Moriya, C. J. Newsome, and T. Shimoda, "Inkjet printing of polymeric field-effect transistors and its applications," Jpn. J. Appl. Phys., vol. 44, no. 6A, pp. 3649–3658, 2005.

[33]   [online]:   https://www.controlprint.com/products/hires/   (Accessed August. 2017).

[34]   B. Sanz-Izquierdo and E. Parker, "3-D Printing of Elements in Frequency Selective Arrays", IEEE Trans. Antennas Propagat., vol. 62, no. 12, pp. 6060-6066, 2014.

[35]   B. Sanz-Izquierdo and E. A. Parker, "Frequency selective surfaces formed by partially metalising 3D printed shapes," in 2015 9th European Conference on Antennas and Propagation (EuCAP), 2015, pp. 1-4.

[36]   S. Jun, B. Sanz-Izquierdo, and E. A. Parker, "3D printing technique for the development of non-planar electromagnetic bandgap structures for antenna applications," Electron Lett., vol. 52, pp. 175-176, 2016.

[37]   M. D'Auria, W. J. Otter, J. Hazell, B. T. W. Gillatt, C. Long-Collins, N. M. Ridler, and S. Lucyszyn, "3-D Printed Metal-Pipe Rectangular Waveguides," IEEE Trans. Compon. Packaging Manuf. Technol., vol. 5, pp. 1339-1349, 2015.

[38]   M. Liang, C. Shemelya, E. MacDonald, R. Wicker and H. Xin, "3-D Printed Microwave Patch Antenna via Fused Deposition Method and Ultrasonic Wire Mesh Embedding Technique", IEEE Antennas Wirel. Propag. Lett., vol. 14, pp. 1346-1349, 2015.

[39]   B. Sanz-Izquierdo and J. Sungyun, "WLAN antenna on 3D printed bracelet and wrist phantom," in 2014 Loughborough Antennas and Propagation Conference (LAPC), 2014, pp. 372-375.

[40]   S. Jun, B. Sanz-Izquierdo, and M. Summerfield, "UWB antenna on 3D printed flexible substrate and foot phantom," in 2015 Loughborough Antennas & Propagation Conference (LAPC), 2015, pp. 1-5.

[41] J. Shen, M. Aiken, C. Ladd, M. D. Dickey and D. S. Ricketts, "A simple electroless plating solution for 3D printed microwave components," 2016 Asia-Pacific Microwave Conference (APMC), New Delhi, 2016, pp. 1-4.

[42] I. T. Nassar and T. M. Weller, "An electrically-small, 3-D cube antenna fabricated with additive manufacturing," in Proc. IEEE Topical Conf. Wireless Sensors Sensor Networks (WiSNet), 2013, pp. 58–60.

[43] J. Tribe, W. G. Whittow, R. W. Kay and J. C. Vardaxoglou, "Additively manufactured heterogeneous substrates for three-dimensional control of local permittivity," Electronics Letters, vol. 50, no. 10, pp. 745-746, May 8 2014.

[44] C. Guo, X. Shang, M. J. Lancaster and J. Xu, "A 3-D Printed Lightweight X-Band Waveguide Filter Based on Spherical Resonators," IEEE Microw. Wirel. Compon. Lett, vol. 25, no. 7, pp. 442-444, July 2015.

[45] A. Lopez, E. C., R. Chandra and A. Johansson, "Optimization and fabrication by 3D printing of a volcano smoke antenna for UWB applications", Antennas and Propagation (EuCAP), 2013 7th European Conference on, pp. 1471-1473, 2013.

[46] C. Garcia, H. Tsang, J. Barton and R. Rumpf, "Effects of extreme surface roughness on 3D printed horn antenna", Electronics Letters, vol. 49, no. 12, pp. 734-736, 2013.

[47] Kim, O.S., "Rapid Prototyping of Electrically Small Spherical Wire Antennas," IEEE Trans. Antennas Propagat., vol.62, no.7, pp.3839-3842, July 2014. ->SLS

[48] Y. Kawahara, S. Hodges, B. S. Cook, C. Zhang, G. D. Abowd, "Instant inkjet circuits: Lab-based inkjet printing to support rapid prototyping of UbiComp devices", Proc. 2013 ACM Int. Joint Conf. on Pervasive and Ubiquitous Computing (UbiComp '13), pp. 363-372, 2013-Sep. -> Inkjet

[49] S. Khan, L. Lorenzelli, and R. S. Dahiya, "Technologies for Printing Sensors and Electronics Over Large Flexible Substrates: A Review," IEEE Sensors J., vol. 15, pp. 3164-3185, 2015.

[50] J. C. Batchelor, E. A. Parker, J. A. Miller, V. Sanchez-Romaguera, and S. G. Yeates, "Inkjet printing of frequency selective surfaces," Electron Lett., vol. 45, pp. 7-8, 2009.

[51]   B. S. Cook and A. Shamim, "Inkjet Printing of Novel Wideband and High Gain Antennas on Low-Cost Paper Substrate," IEEE Trans. Antennas Propag., vol. 60, pp. 4148-4156, 2012.

[52]   S. Kim, R. Vyas, A. Georgiadis, A. Collado, and M. M. Tentzeris, "Inkjet-printed RF energy harvesting and wireless power trasmission devices on paper substrate," in 2013 European Microwave Conference, 2013, pp. 983-986.

[53]   A. Rida, L. Yang, T. Reynolds, E. Tan, S. Nikolaou, and M. M. Tentzeris, "Inkjet-printing UHF antenna for RFID and sensing applications on liquid crystal polymer," in Proc. IEEE Antennas Propag. Soc. Int. Symp., pp. 1–4, Jun. 2009.

[54]   B. K. Tehrani, B. S. Cook and M. M. Tentzeris, "Inkjet Printing of Multilayer Millimeter-Wave Yagi-Uda Antennas on Flexible Substrates," IEEE Antennas Wireless Propag. Lett., vol. 15, pp. 143-146, 2016.

[55]   B. Cook, B. Tehrani, J. Cooper and M. Tentzeris, "Multilayer Inkjet Printing of Millimeter-Wave Proximity-Fed Patch Arrays on Flexible Substrates", IEEE Antennas Wireless Propag. Lett., vol. 12, pp. 1351-1354, 2013.

[56]   H. R. Khaleel, "Design and fabrication of compact inkjet printed antennas for integration within flexible and wearable electronics," IEEE Trans. Compon. Packag. Technol., vol. 4, no. 10, pp. 1722–1728, Oct. 2014.

[57]   H. F. Abutarboush, A. Shamim, "Paper-Based Inkjet-Printed Tri-Band U-Slot Monopole Antenna for Wireless Applications," IEEE Antennas Wireless Propag. Lett., vol.11, pp.1234-1237, 2012.

[58]   M. Nikfalazar, A. Mehmood, M. Sohrabi, M. Mikolajek, A. Wiens, H. Maune, C. Kohler, J. Binder and R. Jakoby, "Steerable Dielectric Resonator Phased-Array Antenna Based on Inkjet-Printed Tunable Phase Shifter With BST Metal-Insulator-Metal Varactors", IEEE Antennas Wireless Propag. Lett., vol. 15, pp. 877–880, 2016.

[59]   J. Kimionis, M. Isakov, B. S. Koh, A. Georgiadis, and M. M. Tentzeris, "3D-Printed Origami Packaging With Inkjet-Printed Antennas for RF Harvesting Sensors," IEEE Trans. Microw. Theory Tech., vol. 63, pp. 4521-4532, 2015.

[60]   [online]: https://ultimaker.com/en/ (Accessed August. 2017).

[61]   [online]: https://formlabs.com/ (Accessed August. 2017).

CHAPTER 3.

3D PRINTED FRACTAL ANTENNAS

3.1 Introduction

This chapter discusses the fabrication of 3D fractal antennas using metal additive manufacturing (AM), also referred to as metal 3D printing (3DP) technologies. 3DP offers the possibility to produce the fabrication of the complex features of fractal models. 3D fractal shapes based on the Sierpinski concept are proposed. These structures have the important property of being able to reduce the amount of material used in an AM process which can lead to lighter weight devices. This is the first time that 3D fractals have been discussed in terms of potential material reduction and their benefit to the AM of microwave components. Material volume reduction is achieved in relation to the equivalent tetrahedron based shapes. Although other types of antenna design, such as planar form structures, may provide better overall volume efficiency, the challenge here has been to use this manufacturing technique to fabricate such complicated 3D structures, and the challenge has been met. All the fractal designs are able to operate at the 2.4 GHz Bluetooth band, and the final design (dual inverse fractal) covers both the 2.4 GHz and 5 GHz WLAN bands. Previously proposed fractal designs required modification of the dimensions of the later iterations in order to achieve operation at the bands of existing wireless communication technologies [1]-[3]. In our case, the scale ratio between the repetitive patterns has been maintained and is the design which has evolved to improve input impedance at the higher band. The 3DP technique employed is a binder jetting metal process. The technique is ideal for the high detailed components of the fractals. The technique is ideal for the highly detailed components of the fractals.

Fractal antennas were introduced more than two decades ago [4], [5]. Since then, they have been widely researched and reported. They offer multiband and

multifunctional operations [6], [7] and, in some cases, small physical size. The basic concept of the fractal antenna starts from the iteration of self-similar elements with different direction and scale but not changing the main shape. Most of the fractal antennas available in the literature are two dimensional, normally based on the monopole [8]-[10] and the patch type [11]. These geometries have been employed in frequency selective surface (FSS) [12], [13] and electromagnetic bandgap (EBG) structures [14], [15]. More recently, three-dimensional fractal antennas have been investigated [16], [17]. They provide improved omnidirectional radiation pattern and wider impedance bandwidth.

This chapter is organized as follows. Section 3.2 proposes a 3D printed Sierpinski gasket antenna to demonstrate the feasibility of using metal AM techniques in 3D fractal antenna productions. Section 3.3 introduces a novel dual fractal design and discusses the fabrication and output features. Section 3.4 presents a novel design based on the inverse fractal antenna and analyses its main characteristics. Finally, this chapter finishes with a discussion and conclusion in Section 3.5. All antenna designs have been simulated using CST Microwave Studio^{TM} and verified with experimental results.

3.2 Sierpinski gasket tetrahedron antenna

In this section, the fabrication of fractal monopole antennas via additive manufacturing with metals is proposed, with the Sierpinski tetrahedron fractal antenna as an example. The design has been tuned for a first resonant frequency operating at the Bluetooth frequency band. The cores of the radiating elements were fabricated using a metal powder based manufacturing method and a material based on steel. Steel is not the most efficient conductor, which may initially indicate that it is not suitable for antenna applications. For this reason, the antenna was coated using a simple and inexpensive copper plating process.

33

3.2.1 Antenna design and analysis

The Sierpinski tetrahedral antenna [18], [19] is formed by removing scaled down versions of an original solid tetrahedron in a repetitive process. This removal of material weakens the structure, so a procedure for providing adequate strength is outlined in this section. But before this can be done, a brief outline of the design procedure follows. If the scale factor used is 0.5, each repetition results in four identical copies with their corners touching each other (Figure 3.1). The number of tetrahedron created at the ith iteration is:

$$N_i = 4^i \tag{1}$$

All the sides of the tetrahedrons are equal in length, given by:

$$L_i = \left(\frac{1}{2}\right)^i L_0 = 2^{-i} L_0 \tag{2}$$

where L_0 is the length of the side of the initial tetrahedron.
The height of each new tetrahedron, h_i in relation to the total initial height H_0, and to the initial side L_0, is:

$$h_i = \left(\frac{1}{2}\right)^i H_0 = \left(\frac{1}{2}\right)^i \sqrt{\frac{2}{3}} L_0 \tag{3}$$

In this fractal, the combined surface area of all faces of all tetrahedrons (both interior and exterior faces) is equal the total area of the original tetrahedron. If the total surface area of the original tetrahedron is A_0, the surface area of each tetrahedron created in iteration i is given by:

$$A_i = \left(\frac{1}{4}\right)^i A_0 \tag{4}$$

The quantity A_i might be significant if not all faces were to be covered by depositing conducting material. The total surface area at the ith iteration is then:

$$A_{Ti} = 4^i \left(\frac{1}{4}\right)^i A_0 = A_0 \qquad (5)$$

In general, the external faces are more important than the internal characteristics in terms of radiation current. The total external surface area A_{ETi} is:

$$A_{ETi} = \left(\frac{3}{4}\right)^i A_0 \qquad (6)$$

The reduction of the volume from the original non-fractal tetrahedron design (V_0) is an important factor when considering the cost of the material used for additive manufacturing processes. The volume of each tetrahedron can be calculated as:

$$V_i = \left(\frac{1}{8}\right)^i V_0 \qquad (7)$$

Thus the total volume is given by:

$$V_{Ti} = 4^i \left(\frac{1}{8}\right)^i V_0 = 2^{-i} V_0 \qquad (8)$$

A 3D Sierpinski fractal antenna can be created by arranging the structure so that the feeding is connected to one of the vertices [19]. Three iterations have been applied in this illustration, giving a total number of 64 tetrahedrons. A Sierpinski antenna of total height H_0 of 22mm was simulated, and its reflection coefficient (S_{11}) is presented in Figure 3.2 as "without overlap." From equations (6) and (8), the designs use 42% of the external area and 12.5% of the volume of the corresponding non-fractal tetrahedron. A circular metal ground plane with radius r of 70mm was employed. In order to be able to fabricate the antenna using AM techniques and moreover to provide sufficient mechanical strength, every minor tetrahedron was

35

overlapped with its neighbor. The overlap was 0.56mm throughout. Figure 3.1 illustrates the principle. This decreased the total height of the antenna from 22.0mm to 18.1mm. The modified design is presented as "with overlap" in Figure 3.1(b), i.e. successive tetrahedrons are merged into each other. The new design used 58% of the external area and 22% of the volume of an equivalent non-fractal tetrahedron of height 18.1 mm. The overlap increased the frequencies of most resonant modes and improved the S_{11} matching (Figure 3.2). This design is able to operate at the 2.4GHz band with further resonant modes at higher bands.

(a)

(b)
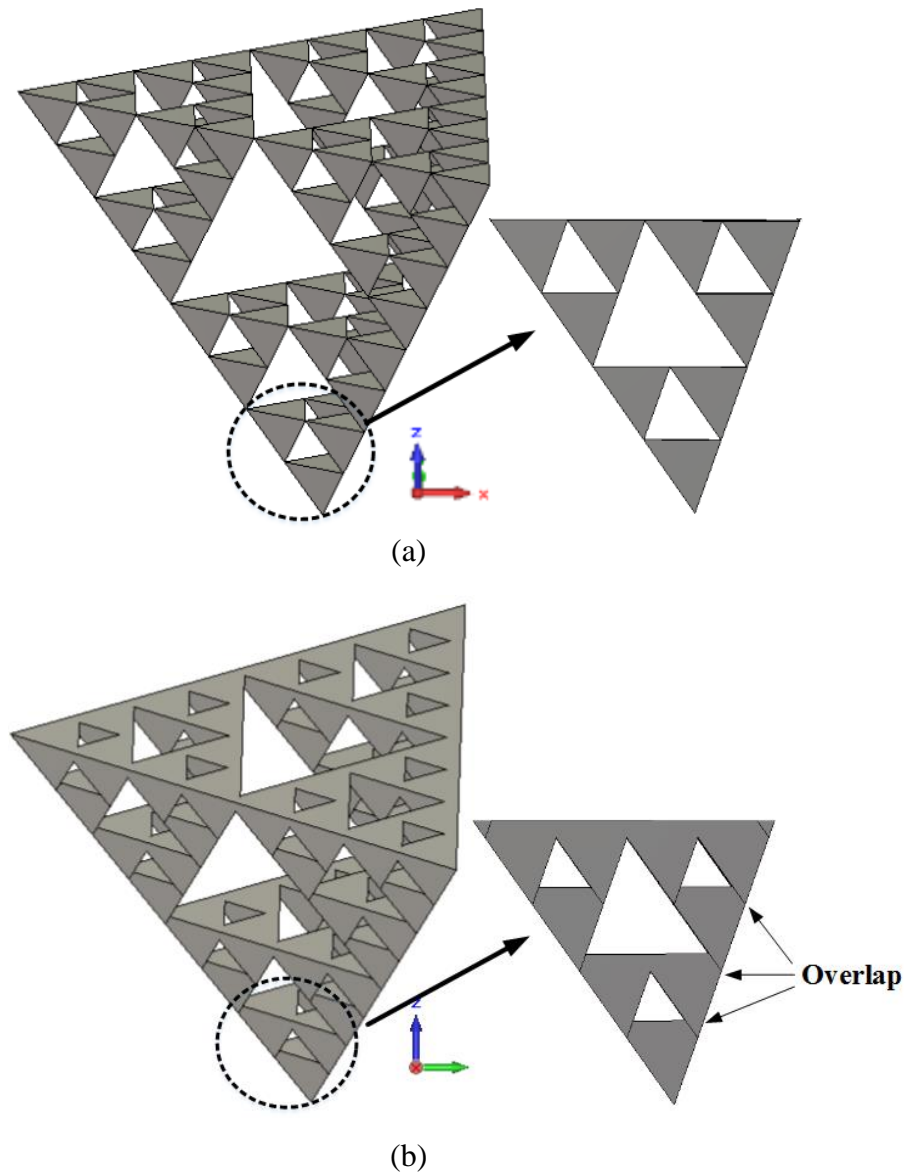
Figure 3.1 Perspective view of the Sierpinski fractal antenna

(a) without overlap and (b) with overlap

36
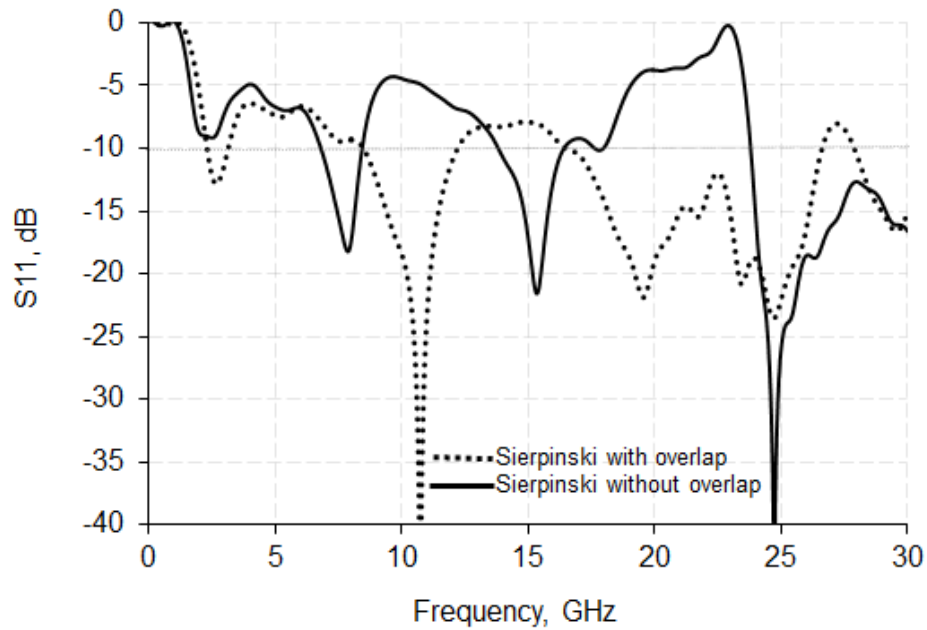
Figure 3.2 Reflection coefficients of the Sierpinski fractal antenna:
with, and without overlap

As shown in Figure 3.1(b), a Sierpinski tetrahedron gasket is developed from 3 mathematical iterations. This relatively simple design was employed as an illustration. This fractal shape was placed on a circular copper ground plate of diameter d = 140mm and fed by a 50Ω SMA connector. The inner of the SMA connector extended beyond the ground and into the antenna at its lowest point, providing mechanical support to the structure. This point had to be reduced slightly to enable adequate fixing to the coaxial connector. This reduced the height of the radiating element to about 17mm. These mechanical changes also had the effect of improving the input matching across frequencies.

The computed reflection coefficient S_{11} of the antenna is shown in Figure 3.3. For comparison, the S_{11} characteristic of a non-fractal tetrahedron monopole antenna of the same dimensions is included. In this specific design, the first and second resonance occurred at about the same frequency as those of the non-fractal tetrahedron antenna, but higher modes differ both in resonant frequency and input match. The mode at 2.4GHz is almost identical for the two antennas while the mode

at 10GHz is better matched in the case of the fractal antenna. The main benefit of the fractal structure is that it uses 22% of the volume of an equivalent non-fractal tetrahedron. This is nearly 80% reduction in the material used in the 3DP process.
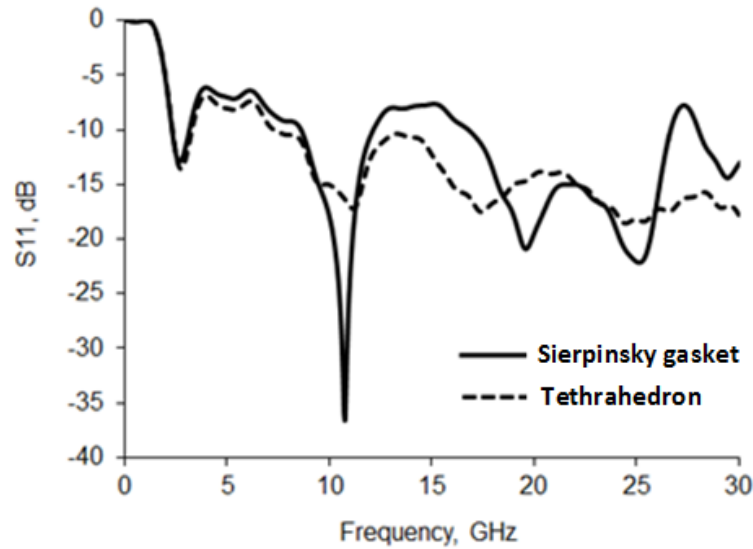
Figure 3.3 Simulated reflection coefficient (S_{11}) for the Sierpinski gasket and a non-fractal tetrahedron monopole antenna

3.2.2 Measurement Results, Reflection Coefficient

The complexity of the internal and external features of the new design makes it very difficult to fabricate using traditional subtractive techniques. In order to investigate the potential applicability of additive manufacturing for 3D fractal antenna development, a metal powder bed fusion process, and more specifically Metal Powder Embinder Printing was employed [20], [21]. This metal technique was selected because of the mechanical robustness of the output, and the possibility of printing high detailed features. The technology prints the models by binding together layers of ultra-fine grains of stainless steel powder in a precision inkjet printer. Once the printing is done, the part is sintered in an oven at 1300°C. The design specifications required a minimum thickness wall of 0.3mm and a minimum detail of 0.1mm.

The digital model was exported from CST Microwave Studio^{TM} to an STL format and then uploaded to the 3D printer developed in Eichenberger Futuretech AG [22]. Additive manufacturing using copper was unavailable. The base metal used was 316L stainless steel, a material with inferior conductivity. Consequently, a layer of copper of approximately 50µm was deposited onto the antenna using an electroplating process readily available in our laboratory at the University of Kent. This increased the surface conductivity to that for copper. At radio frequencies, the penetration of currents into surface of the conductive layers was controlled by the skin depth effect. The skin depth of the copper layer at 2.4 GHz was 1.3µm calculated by an equation [23]. The deposited copper layer is enough thick to carry out an amount of current. An aperture of a diameter of 2mm was created during the design process which was later used to feed the antenna with a 50Ω SMA connector. The resulting copper plated fractal antenna is shown in Figure 3.4.

(a)   (b)
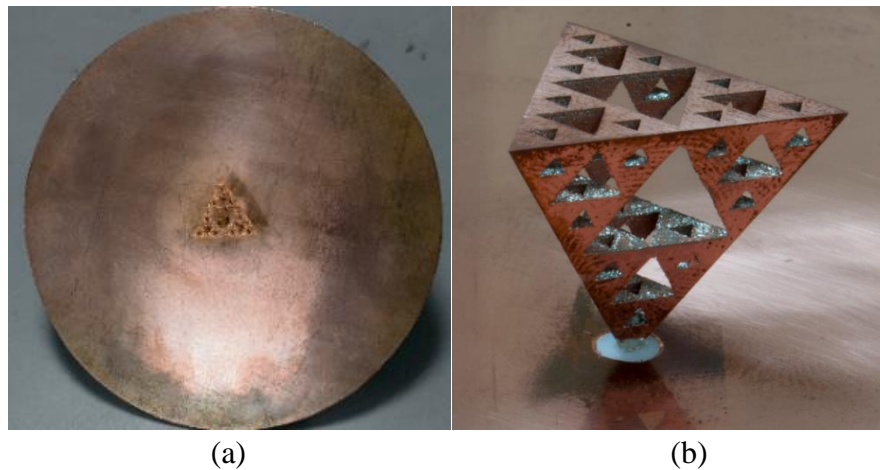
Figure 3.4 Fabricated fractal Antenna

(a) Top view (b) Perspective view of the fractal radiator

The reflection coefficient (S_{11}) shown in Figure 3.5, together with the computed results for the steel configuration. S_{11} was measured using a Rohde & Schwarz vector network analyzer with a frequency sweep of 0 to 13.6GHz. Measured results compare well with those from the simulations, with only a 4.61% frequency shift in the resonant frequencies. This probably arises from inaccuracies in the fabrication process. The measured radiation patterns at 2.45GHz in the *xy* plane and *xz* plane are

shown in Figure 3.6. Radiation patterns were virtually omnidirectional at 2.45GHz.
The calculated gain was 3.7dB at 2.45GHz.
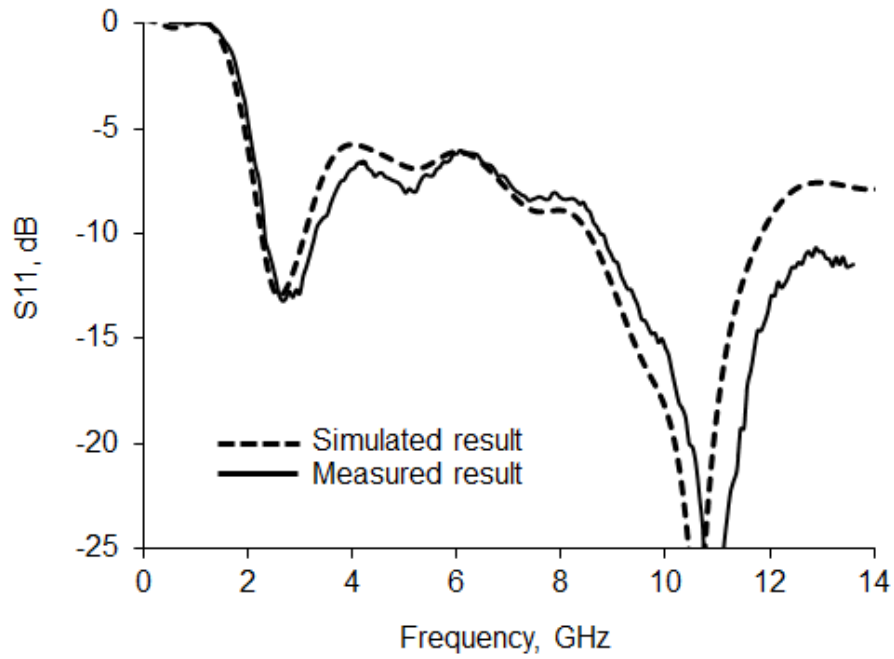
Figure 3.5 Simulated and measured reflection coefficient (S_{11})

(a)   (b)
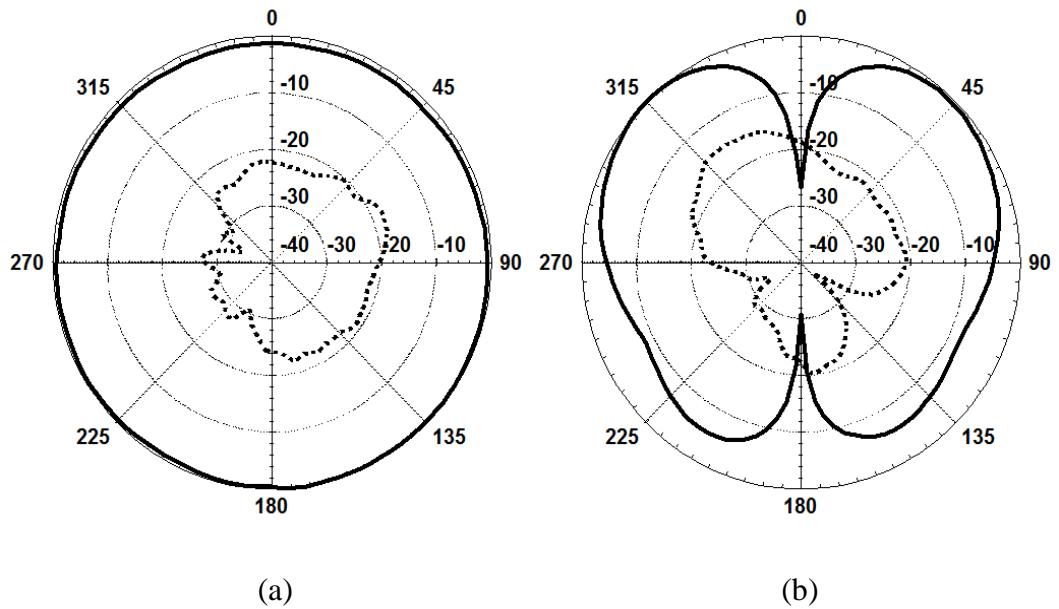
Figure 3.6 Normalized Radiation Pattern of the Antenna at 2.45GHz (Solid line: Co-
polarization. Dotted line: Cross-polarization) (a) *xy* plane (b) *xz* plane

3.3 3D dual fractal antenna

3.3.1 Antenna Design and Analysis

In order to improve the matching and better assess the manufacturing process (Figure 3.10), a new structure was created by adding a copy of the design (Figure 3.7(a)) and rotating by 60° around the z-axis. The resulting structure is shown in Figure 3.7(b), and in Figure 3.8 the feed arrangements are illustrated. This design uses 58% of the external area and just 22.4% of the volume of the equivalent non-fractal design. In order to provide mechanical strength, the inner cylinder diameter of 2mm from the coaxial input port was extended to the fractal antenna. The total height of 18mm and the extent of the overlap were retained in the new design.

Adding a copy of the design
and rotating by 60 degree
around the z-axis

(a)   (b)
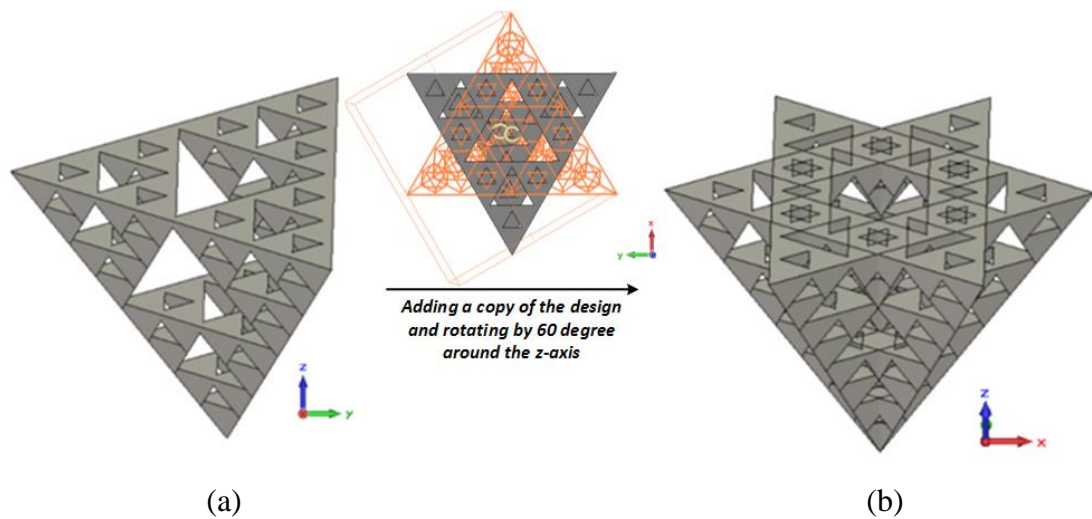
Figure 3.7 Perspective view of (a) a classical and (b) the proposed fractal antenna
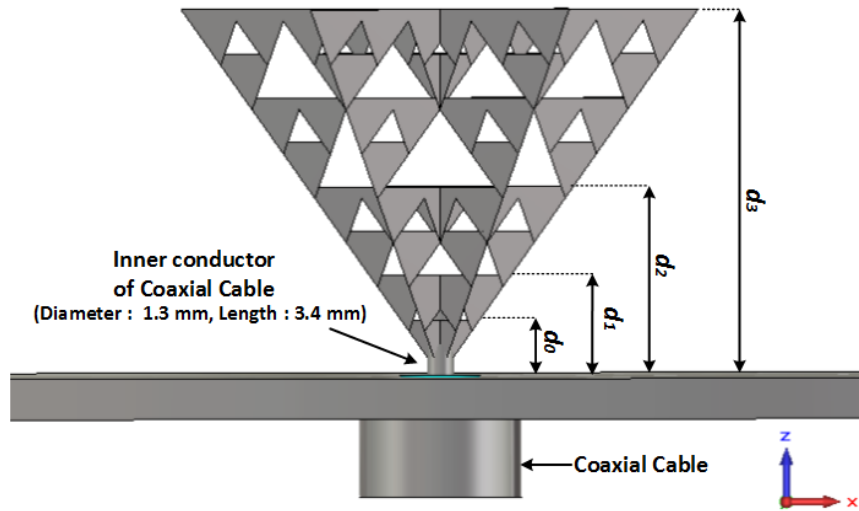
Figure 3.8 Dual fractal design connected to the coaxial feed line and the ground plane. The distances between repetitions n and the ground plane, d_n, are included

The antenna can be further analyzed in terms of the various distances d_n from the metallic ground to the tops of the repetitive tetrahedrons (Figure 3.8). The parameter d_n can be used to analyze the resonant characteristics of the levels of the repetitive patterns [18]. As discussed earlier, mechanical strength was the main reason for the overlap of 0.56mm in every repetition of the structure. Figure 3.9 shows the reflection coefficient when the antenna is cut at the different levels d_n. The results are summarized in Table 3.1. The various distances of the repetitions to the metallic ground (Figure 3.8), d_n (mm), can be calculated by the equation:

$$d_n = 2d_{n-1} - 0.56 \tag{9}$$

where d_0 is 2.75 mm.
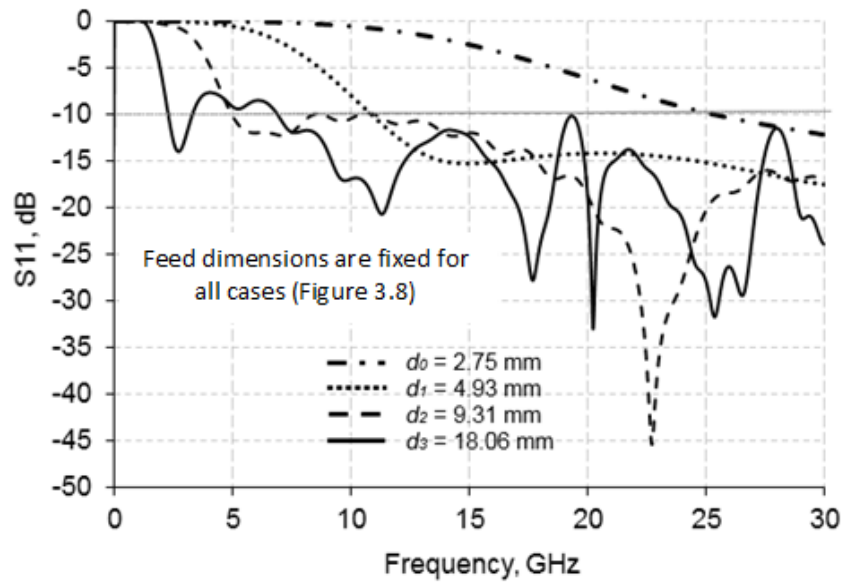
Figure 3.9 Simulated reflection coefficient of four different scaled 3D fractal antennas

TABLE 3.1

FOUR DIFFERENT SCALED 3D FRACTAL ANTENNA

	$d_0 = 2.75$ mm	$d_1 = 4.93$ mm	$d_2 = 9.31$ mm	$d_3 = 18.06$ mm
f_0	45.0 GHz	14.9 GHz	5.8 GHz	2.7 GHz
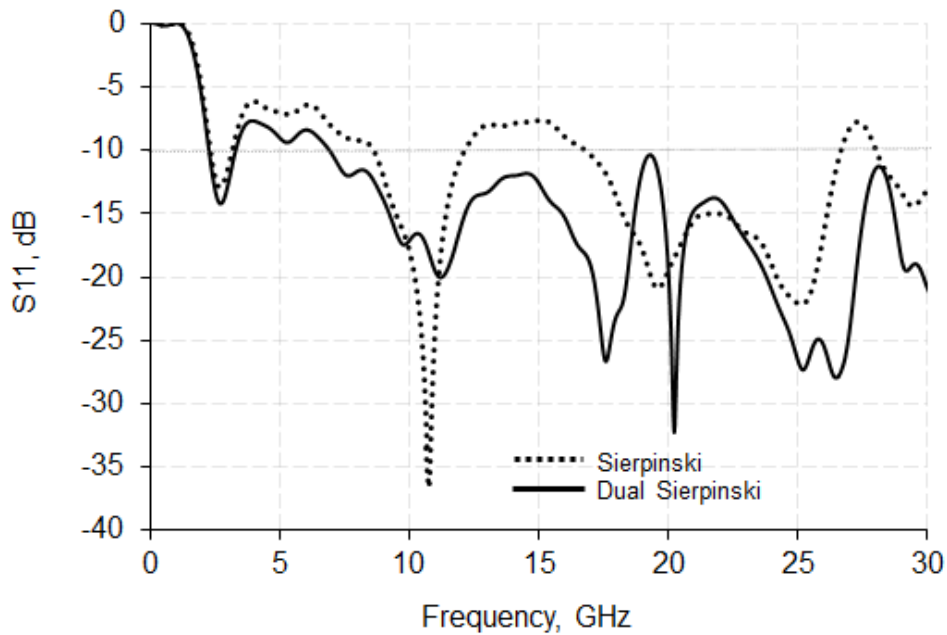
Figure 3.10 Simulated reflection coefficients of the initial Sierpinski (Figure 3.1(b))
and new dual fractal (Figure 3.8) antenna, both with overlap

Figure 3.10 shows the simulated S_{11} for the new antenna and its comparison with the initial Sierpinski design for a frequency range from 0GHz to 30GHz. The new structure has further improved impedance match, particularly at the higher bands. The -10dB input match now covers from 6.9GHz to over 30GHz. The first and second resonances are very similar for both the initial fractal design provides four bands, at 2.7GHz, 10.8GHz, 19.6GHz, and 25.2GHz. In contrast, the proposed dual fractal antenna has five different resonances, at 2.7GHz, 11.2GHz, 17.6GHz, 20.2GHz, and 25.2GHz, in the same range.

3.3.2 Measurement Results, Reflection Coefficient

Figure 3.11 shows a photograph of the 3D dual fractal antenna. A circular copper ground plane with a diameter of 140mm and the thickness of 2mm. The 3D surface profiles of the fractal structure are shown in Figure 3.12. The surface roughness was 1.92μm (*Sa, Arithmetical mean height*), and the RMS deviation of 2.46 μm (*Sq, Root mean square height*) measured in Centre for Process Innovation [24].
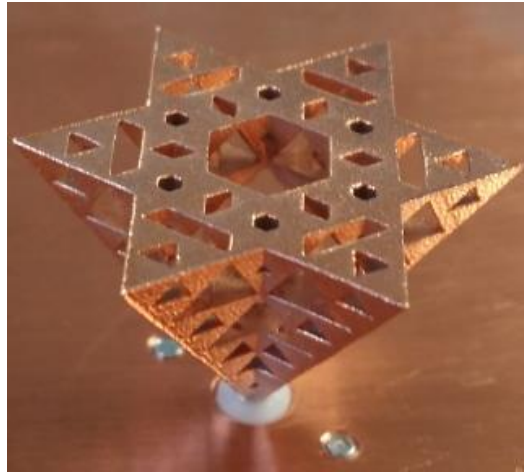
(a)

(b)

Figure 3.11 Photographs of the fabricated dual fractal antenna:

(a) oblique (b) top view

The measured reflection coefficients of the dual fractal antenna are compared with simulations in Figure 3.13. A Rohde & Schwarz®ZVL vector network analyzer was used for the experiments. Good agreement was found between simulations and measurements. There was a slight increase in the resonant frequency and decrease in the input match at the first mode. However, the measured S_{11} was lower than those simulated at the higher bands. The differences between simulations and measurements are likely due to additive fabrication tolerances.

(a)

Figure 3.12 (c)

(b)

Length = 884.3 µm Pt = 10.01 µm Scale = 20 µm
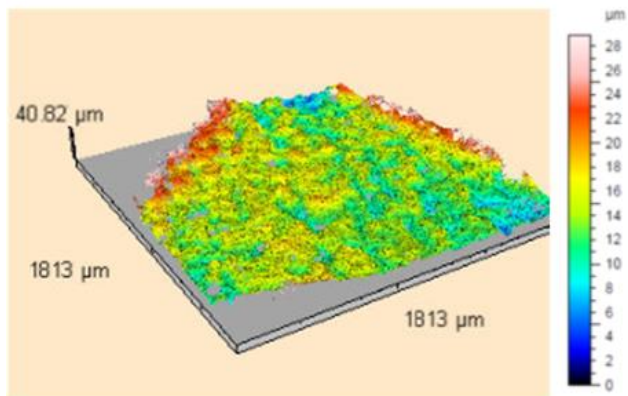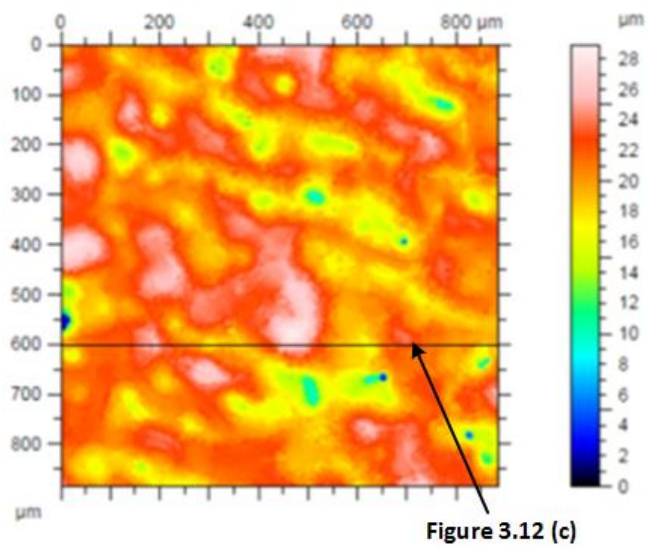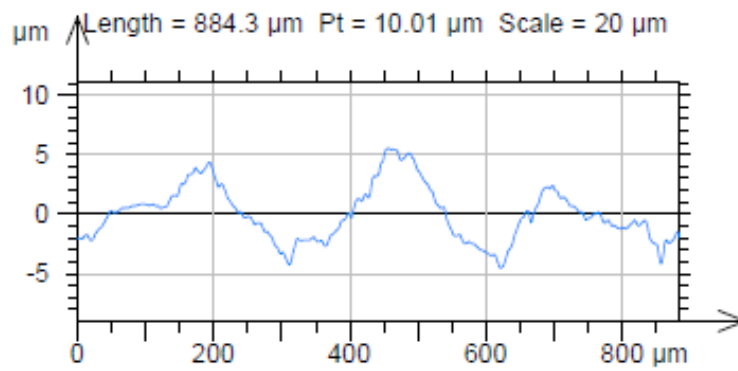
(c)

Figure 3.12 Measured surface profile:

(a) 3D profile, (b) zoomed profile, (c) profile 2D cut
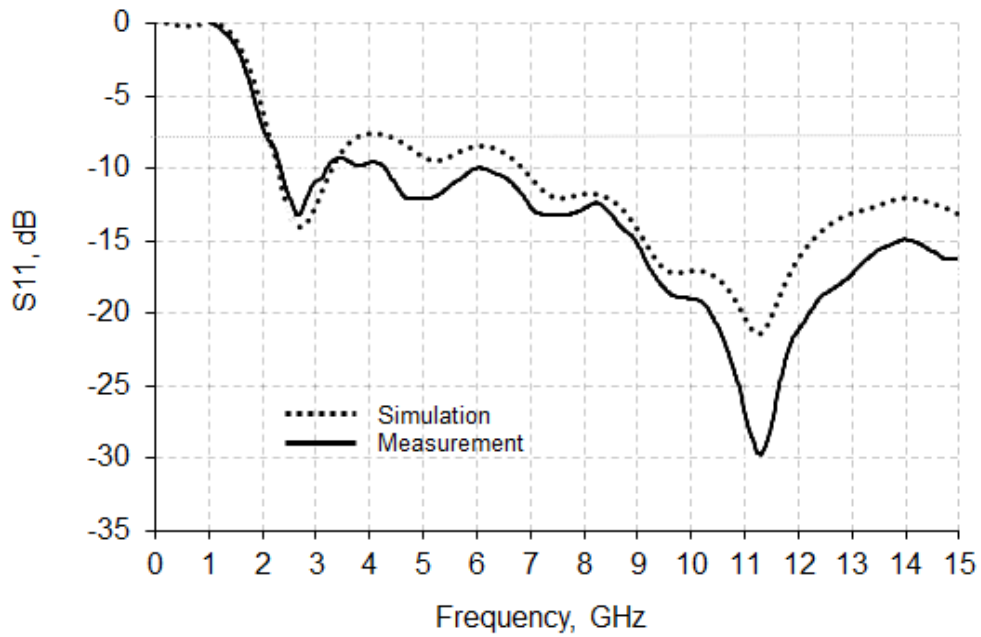
Figure 3.13 Reflection coefficient of the dual fractal antenna

3.3.4 Radiation pattern

Radiation patterns were measured at various frequencies in an anechoic chamber. Figure 3.14 shows the patterns in the *xy* and *xz* planes at 2.6GHz, 5.5GHz and 11.5GHz. The patterns were similar to those for a wideband monopole antenna on a large ground plane. They were omnidirectional in the *xy* plane with a null in the *z* axis. Low cross-polar levels were observed at the studied frequency bands, typically -20dB or below. The computed gains were 3.91dB, 4.54dB, and 4.46dB at 2.6GHz, 5.5GHz and 11.5GHz.
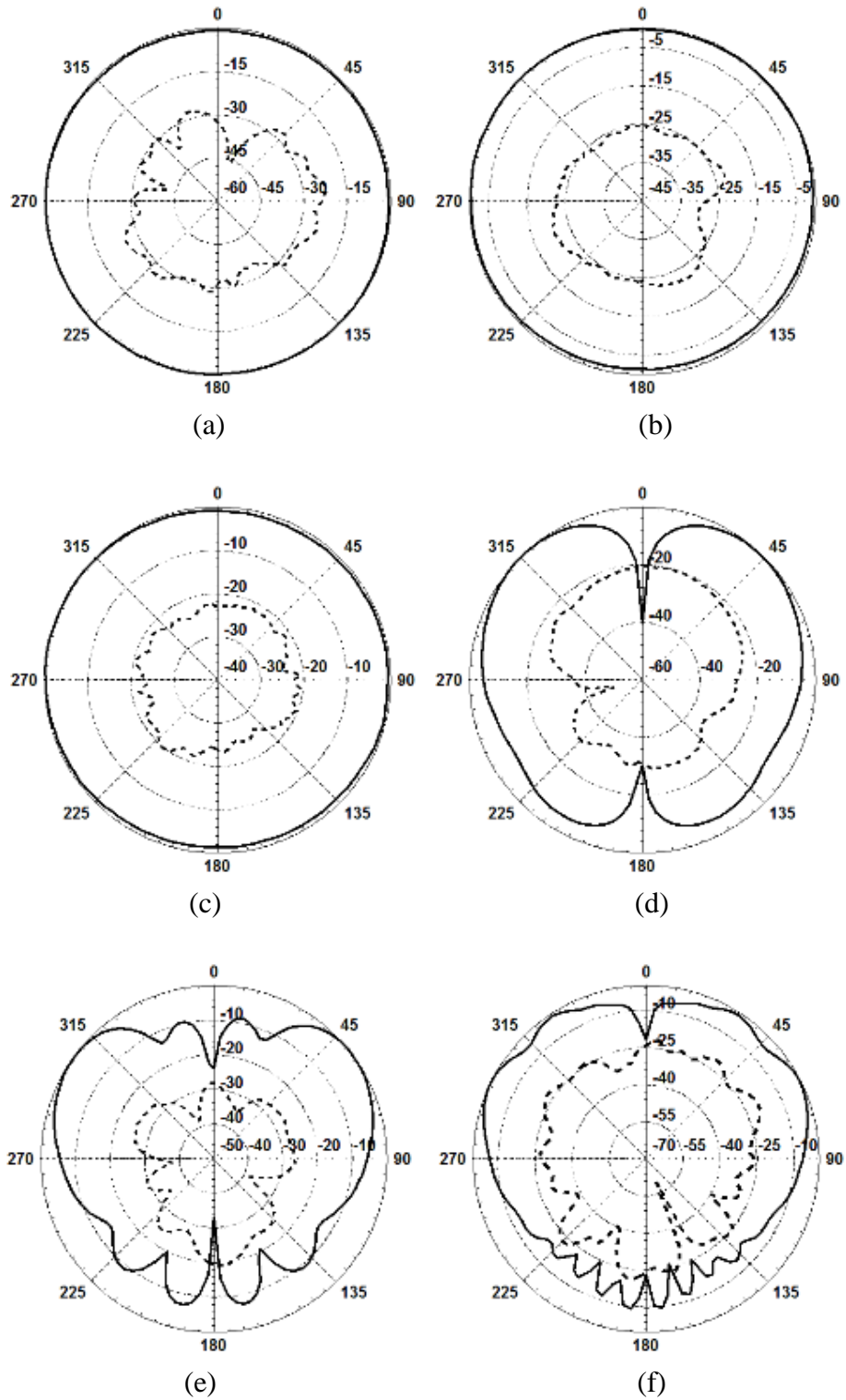
Figure 3.14 Measured radiation pattern characteristic of the dual fractal antenna at various frequencies (a) 2.6 GHz (*xy* plane) (b) 5.5 GHz (*xy* plane) (c) 11.5 GHz (*xy* plane) (d) 2.6 GHz (*xz* plane) (b) 5.5 GHz (*xz* plane) (c) 11.5 GHz (*xz* plane). Solid curves: co-polar, broken curves: cross polar

3.4 3D Inverse fractal antenna

3.4.1 Antenna Design and Analysis

The 3D fabrication of antennas based on the inverse fractal configuration (Figure 3.15(c)) has also been studied. The geometry of the inverse Sierpinski fractal antenna has most of the complex features in the external faces, and therefore its input matching is more likely to be sensitive to fabrication errors. This can provide a further assessment of the fabrication process. The antenna is developed as illustrated in Figure 3.15. Basically, the fractal design (Figure 3.15(b)) is subtracted from a non-fractal tetrahedron (Figure 3.15(a)), resulting in the structure in Figure 3.15(c). As a complement of the original designs, the new structure occupies about 77% of the volume of the equivalent tetrahedron.

(a)   (b)   (c)
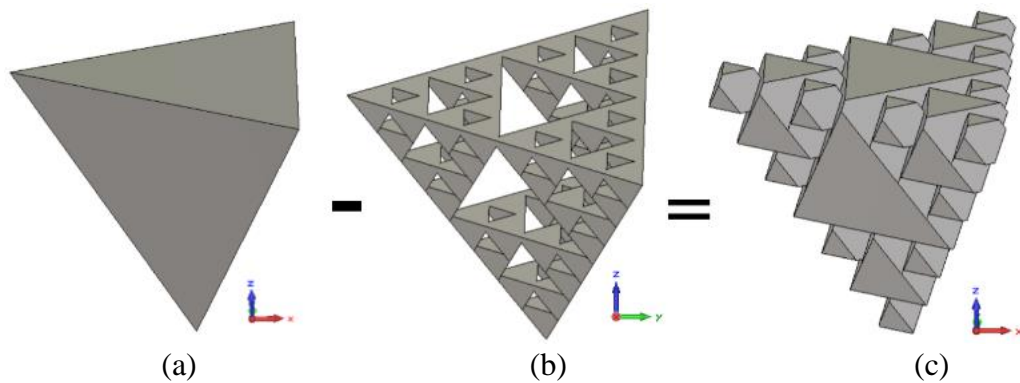
Figure 3.15 Design process for the inverse fractal antenna

(a) tetrahedron (b) Sierpinski fractal, and (c) inverse Sierpinski fractal

3.4.2 Measurement Results, Reflection Coefficient

Simulations of this new configuration (Figure 3.15(c)) resulted in a first resonant frequency of about 3.0GHz. As the main aim of this work was to construct antennas suitable for existing wireless systems, the dimensions were scaled by a factor of 1.27 in all directions. The height of the new design was 23mm. The same technique used to develop the dual fractal antenna in Section 3.3 was then applied, resulting in the configuration in Figure 3.16. Again, a copy of the structure was rotated by 60° about the z axis and then merged with the original design.

This antenna was fabricated by additive manufacturing using the same procedure described earlier. The feeding of the antenna was again via a 50Ω SMA connector through the center of the ground plane, as shown in Figure 3.17.

(a)   (b)
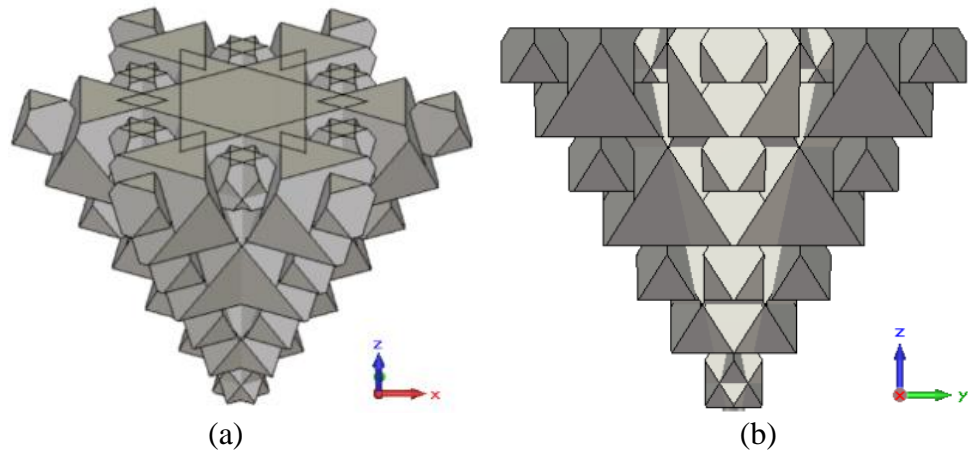
Figure 3.16 Dual inverse fractal antenna (a) perspective view and (b) side view

(a)   (b)
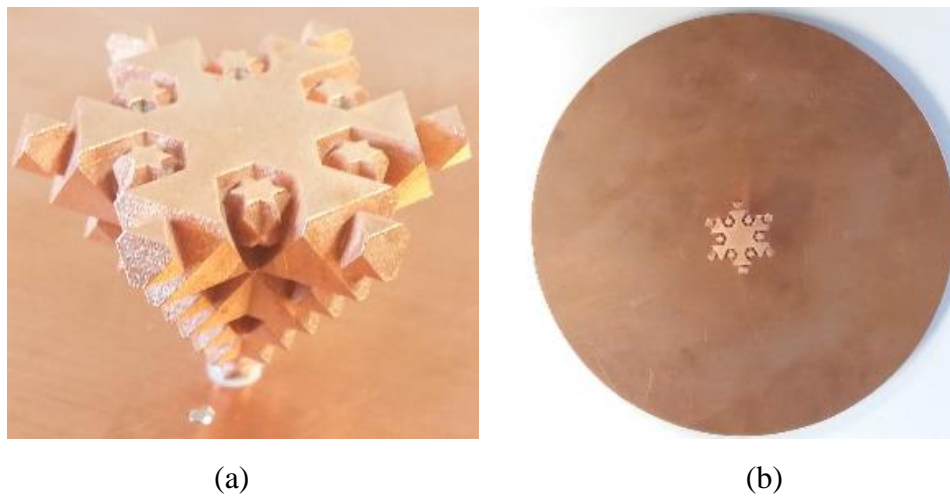
Figure 3.17 Photographs of the fabricated of dual fractal antenna:

(a) oblique (b) top view

The simulated and measured S_{11} of the dual inverse antenna, together with the simulated results for the initial inverse antenna (Figure 3.15(c)) are shown in Figure 13.18. The dual inverse fractal has improved impedance matched. Both simulated and measured results are in good agreement. In the measurement, the resonant modes

have shifted up by about 8% from the simulations. At the 2.4GHz and 5.5GHz WLAN bands, and up to about 10GHz, the S_{11} levels are -10dB or below.
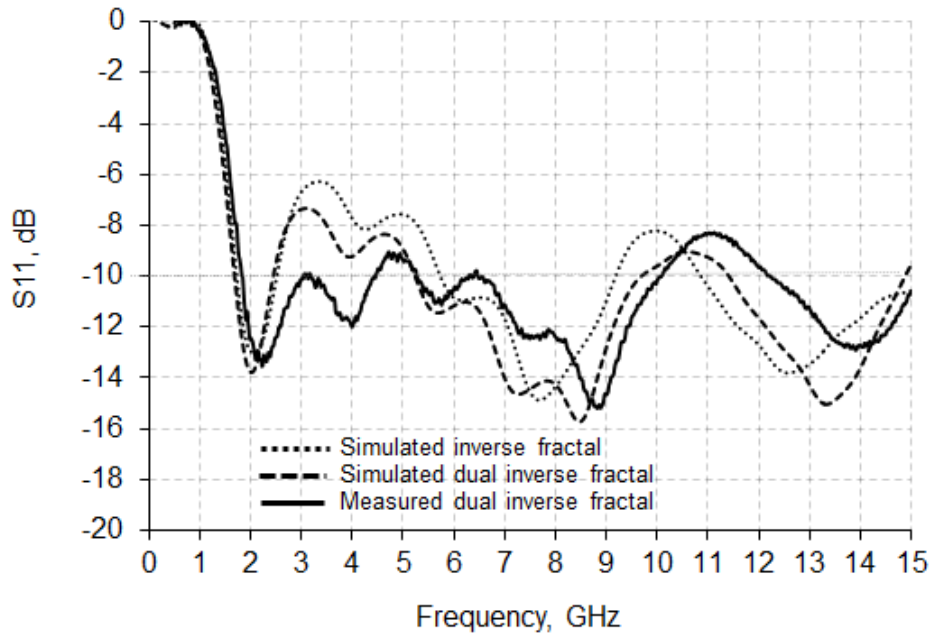
Figure 3.18 Reflection coefficients of the dual inverse fractal antenna (Figure 3.16) and the Inverse fractal (Figure 3.15(c))

3.4.3 Surface Current

The surface current distributions of the Inverse fractal antennas (Figure 3.15(c) and Figure 3.16) for three resonant frequencies are shown in Figure 3.19 and Figure 3.20. As expected, the surface currents are spread over a larger area at lower frequencies. Little current is found at the top of the structure, particularly at its center. This could be an indication that some of the material could be removed, reducing the content below the 77% of the equivalent tetrahedrons, without affecting the performance significantly.
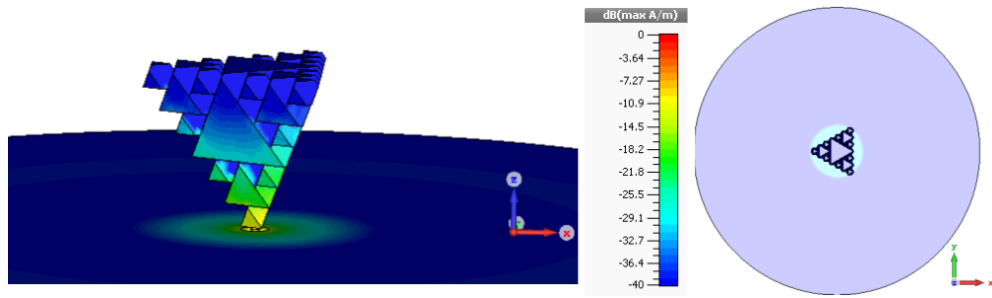
(a)
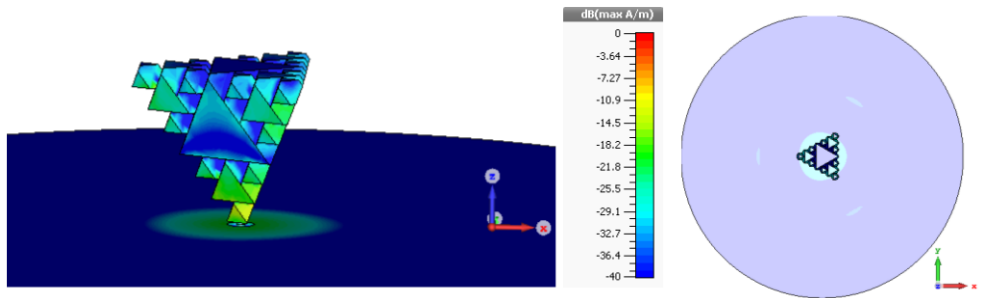
(b)
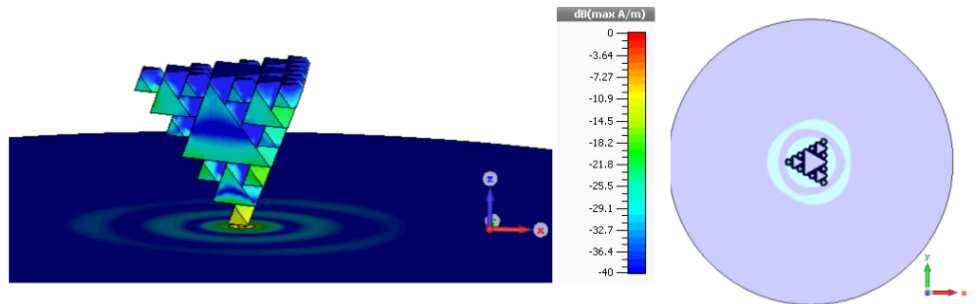
(c)

Figure 3.19 The surface current density of the Inverse fractal antenna at the
frequencies (a) 2.4GHz (b) 8.9GHz (c) 13.8GHz

(a)

(b)

(c)
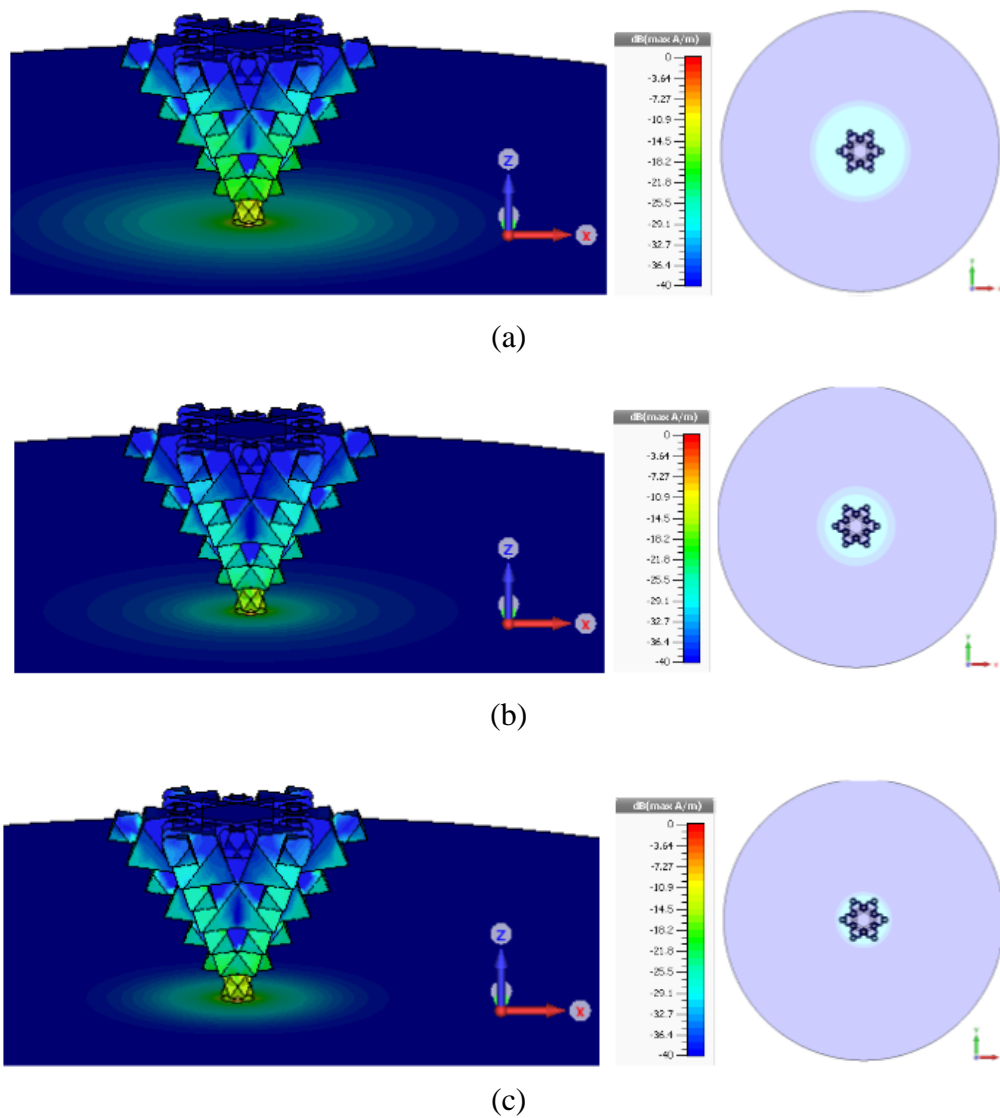
Figure 3.20 The surface current density of the Inverse dual fractal antenna at the frequencies (a) 2.4GHz (b) 5.5GHz (c) 8GHz

3.4.4 Radiation Patterns

The main sections of the measured radiation patterns of the dual inverse fractal design (Figure 3.16) at three resonant frequencies of 2.4GHz, 5.5GHz and 8GHz are presented in Figure 3.21. The patterns are mainly omnidirectional in the *xy* plane. For comparison, the patterns for the initial inverse fractal (Figure 3.15(c)) are presented in Figure 3.22, the patterns for the inverse dual fractal are more omnidirectional and with lower cross polar levels than those for the initial inverse fractal design.

(a)

(b)

(c)

(d)

(e)

(f)
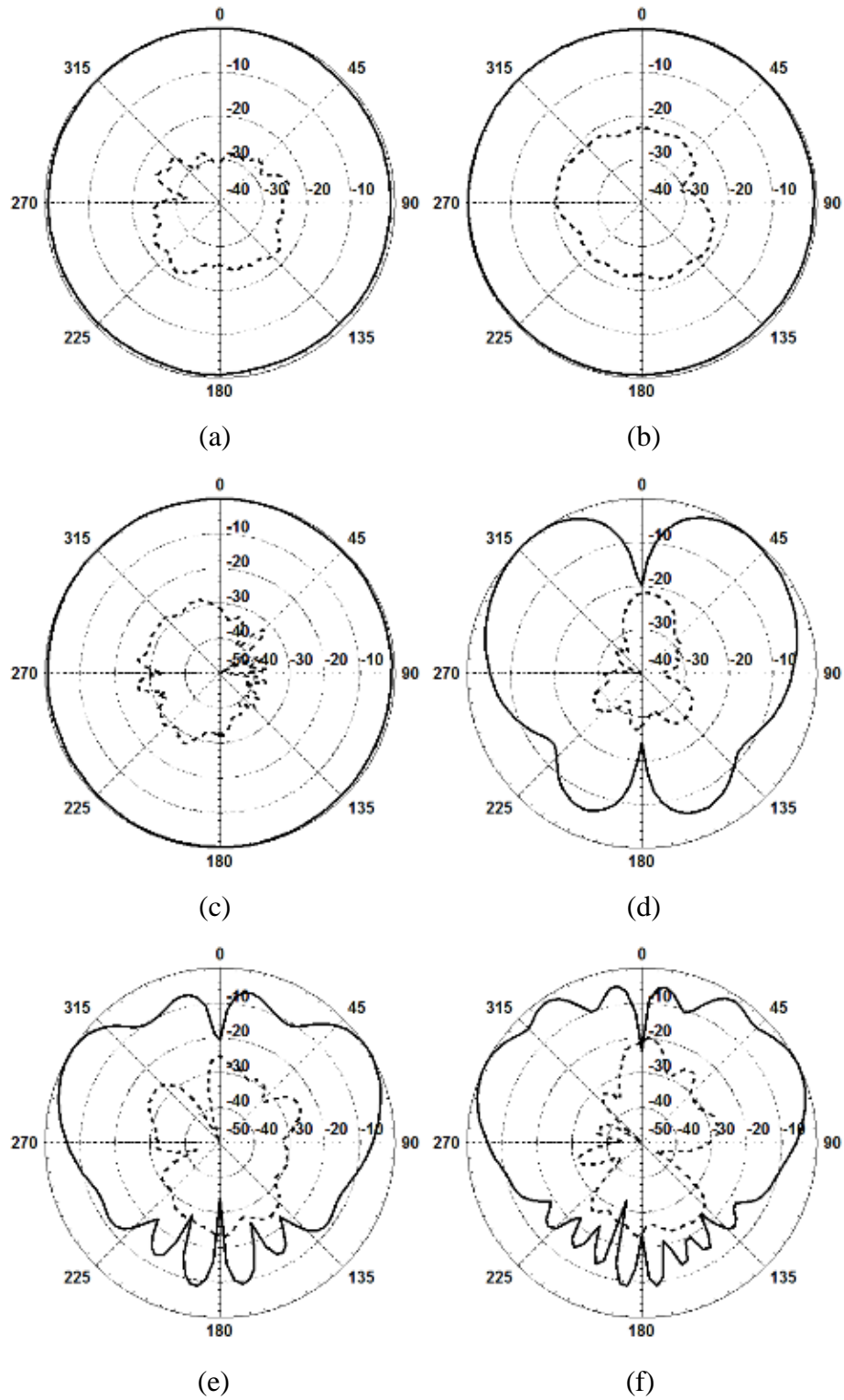
Figure 3.21 Measured Radiation pattern characteristic of the dual inverse Sierpinski fractal antenna (Figure 3.16): (a) 2.4 GHz (*xy* plane) (b) 5.5 GHz (*xy* plane) (c) 8 GHz (*xy* plane) (d) 2.4 GHz (*xz* plane) (b) 5.5 GHz (*xz* plane) (c) 8 GHz (*xz* plane)

54

(a)

(b)

(c)

(d)

(e)

(f)
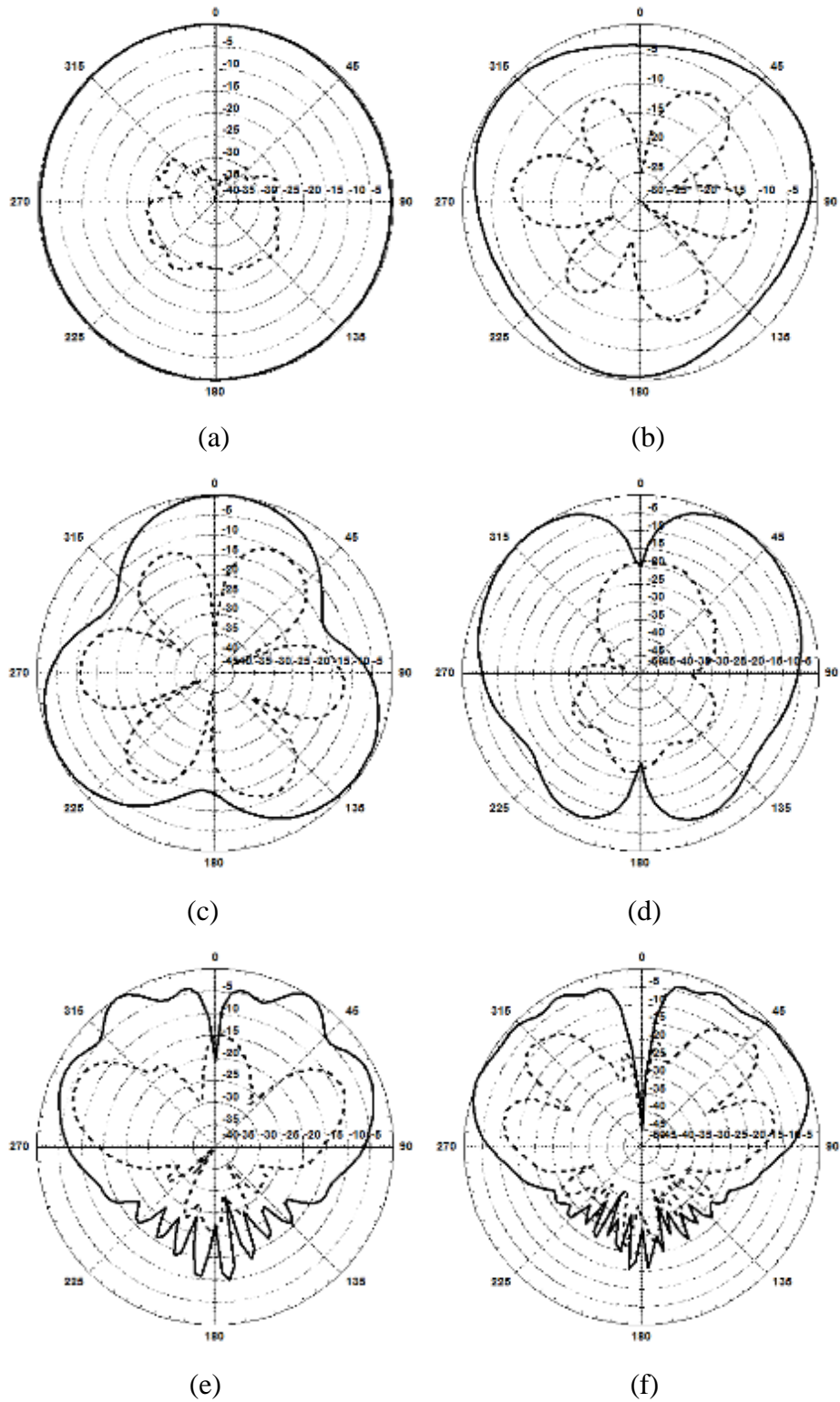
Figure 3.22 Measured radiation pattern characteristic of the Inverse fractal antenna (Figure 3.15(c)) at the frequencies (a) 2.4 GHz (*xy* plane) (b) 8.9 GHz (*xy* plane) (c) 13.8 GHz (*xy* plane) (d) 2.4 GHz (*xz* plane) (b) 8.9 GHz (*xz* plane) (c) 13.8 GHz (*xz* plane)

3.5 Conclusions

In this chapter additive manufacturing has been proven to be suitable for the development and fabrication of 3D fractal antennas. 3DP with metals gives mechanical strength, particularly in the joints between the various repetitions of the fractal elements. The antennas can be fabricated using Metal Powder Embinder Printing, and an additional electroplating process. The alternative option of plating printed dielectrics would have a mechanical weakness at the joints. The structures presented here offer attractive electromagnetic features and are also able to reduce the amount of material used in AM processes. A new dual fractal Sierpinski design improves antenna matching at higher bands compared with the original Sierpinski tetrahedron. More importantly, it decreases volume usage by over 75% compared with the equivalent non-fractal design. The study included here indicates that significant material reduction can be achieved using Sierpinski fractals or similar structures, potentially reducing costs of manufacturing.

The inverse Sierpinski tetrahedron fractal has less smooth external features and therefore is more sensitive to fabrication processes. The imprecision in the fabrication process produces a shift in the resonant frequencies of about 8% at all bands. However, the final dual inverse fractal design is still able to resonate at the 2.4GHz and 5.5GHz WLAN bands, while also providing operational capability at higher frequencies, both in simulation and measurements. It also offers a good omnidirectional pattern and low cross-polarization levels. The dual inverse fractal uses 23% less material than the equivalent non-fractal design. Moreover, current flow simulations indicate that there is potential to reduce the amount of material further without affecting electrical performance.

There are very slight differences between simulations and measurements which probably arose from fabrication inaccuracies. Nevertheless, this work demonstrates that this 3DP technique is a relatively accurate and reliable method for fabricating complex radiating structures required to operate at frequencies below 15GHz.

In summary, the dual fractal antenna (Figure 3.7(b)) and dual inverse fractal antenna (Figure 3.16) demonstrate improved impedance matching compared to the fractal antenna (Figure 3.7(a)) and inverse fractal antenna (Figure 3.15(c)), respectively. In the manufacturing process, fractal antennas use less material than the equivalent tetrahedrons. In particular, the dual fractal antenna has a smaller volume than the dual inverse fractal antenna and still covers the 2.4 GHz and 5.5 GHz WLAN bands. Therefore, the dual fractal antenna offers an effective design from an engineering perspective from the point of view of an engineer compared to other fractal antennas.

Fractal and complex antennas fabricated using 3DP with metals have applications in the defense and aerospace sectors where robustness as well as light weight are key. The antennas could be integrated with other additive manufactured parts. For example, the present structure is less than 2cm in height but for operation at longer wavelengths or structures with higher iterations, a non-conducting dielectric support could be formed integrally with the antenna.

In conclusion, this chapter describes that some very recent advances in AM include the direct fabrication using copper, a process that is yet to be commercialized. Nevertheless, 3DP has now been proved capable of providing a solution to the fabrication of light-weight 3D fractal antennas.

References

[1] R. Aziz, M. Alkanhal, and A. Sheta, "Multiband fractal-like antennas," Prog. Electromagn. Res. B, vol. 29, pp. 339–354, 2011.

[2] S. Rai, Y. Choukiker, and S. Behera, "Irregular circular fractal slot antenna for dual wideband applications," in Proc. Int. Symp. Devices MEMS, Intell. Syst. Commun. (ISDMISC), 2011, pp. 1–4.

[3] R. Liu and W. He, "A novel Sierpinski fractal antenna for wireless application," in Proc. 5th Int. Conf. Comput. Inform. Sci., Jun. 2013, pp. 1347–1348.

[4] E. A. Parker and A. N. A. El Sheikh, "Convoluted array elements and reduced size unit cells for frequency-selective surfaces," IEE Proc. H, Microw. Antennas Propag., vol. 138, no. 1, p. 19, 1991.

[5] C. Puente, J. Romeu, R. Pous, X. Garcia and F. Benitez, "Fractal multiband antenna based on the Sierpinski gasket", Electron. Lett., vol. 32, no. 1, p. 1, 1996.

[6] D. H. Werner and S. Ganguly, "An overview of fractal antenna engineering research," IEEE Antennas Propag. Mag., vol. 45, no. 1, pp. 38–57, 2003.

[7] K. Vinoy, J. Abraham and V. Varadan, "On the relationship between fractal dimension and the performance of multi-resonant dipole antennas using koch curves", IEEE Trans. Antennas Propagat., vol. 51, no. 9, pp. 2296-2303, 2003.

[8] L. Lizzi and A. Massa, "Dual-Band Printed Fractal Monopole Antenna for LTE Applications", IEEE Antennas Wirel. Propag. Lett., vol. 10, pp. 760-763, 2011.

[9] K. Hwang, "Dual-wideband monopole antenna using a modified half-Sierpinski fractal gasket", Electron. Lett., vol. 45, no. 10, p. 487, 2009.

[10] H. Oraizi and S. Hedayati, "Miniaturized UWB monopole microstrip antenna design by the combination of Giusepe Peano and Sierpinski carpet fractals," IEEE Antennas Wireless Propag. Lett., vol. 10, pp. 67–70, 2011.

[11] V.V.Reddy and N.V.S.N.Sarma,"Compact Circularly Polarized Asymmetrical Fractal Boundary Microstrip Antenna for Wireless Applications," IEEE Antennas Wirel. Propag. Lett., vol.13, no., pp.118-121, 2014.

[12] J. Romeu and Y. Rahmat-Samii, "Fractal FSS: a novel dual-band frequency selective surface", IEEE Trans. Antennas Propagat., vol. 48, no. 7, pp. 1097-1105, 2000.

[13] B. Sanz-Izquierdo, E.A. Parker, J. Robertson and J.C. Batchelor, "Singly and Dual Polarized Convoluted Frequency Selective Structures", IEEE Trans. Antennas Propagat., vol. 58, no. 3, pp. 690-696, 2010.

[14] X. Bao, G. Ruvio, M. Ammann and M. John, "A Novel GPS Patch Antenna on a Fractal Hi-Impedance Surface Substrate," IEEE Antennas Wirel. Propag. Lett., vol.5, no.1, pp.323-326, Dec. 2006.

[15] Y. Rahmat-Samii and H. Mosallaei, "Electromagnetic band-gap structures: Classification, characterization, and applications," in Proc. 11th Int. Conf. Antennas Propag. (ICAP), 2001, pp. 560–564.

[16] J. S. Petko and D. H. Werner, "Miniature Reconfigurable Three-Dimensional Fractal Tree Antennas", IEEE Trans. Antennas Propagat., vol. 52, no. 8, pp. 1945-1956, 2004.

[17] H. Rmili, O. Mrabet, J.-M. Floch and J.-L. Miane, "Study of an electrochemically deposited 3-D random fractal tree-monopole antenna", IEEE Trans. Antennas Propag. , vol. 55, no. 4, pp.1045 -1050, 2007.

[18] C. Puente-Baliarda, J. Romeu, R. Pous, and A. Cardama, "On the behavior of the Sierpinski multiband fractal antenna," IEEE Trans. Antennas Propag., vol. 46, no. 4, pp. 517–524, Apr. 1998.

[19] A. N. Jabbar, "Studying the effect of building block shape on Sierpinski tetrahedron fractal antenna behavior using FDTD-equivalent electric circuits," J. Microw. Optoelectron. Electromagn. Appl., vol. 11, pp. 162–173, Apr. 2012.

[20] I. Gibson, D. Rosen, and B. Stucker, Additive Manufacturing Technologies, 1st ed. New York, NY, USA: Springer, 2015.

[21] H. Chen and Y. Zhao, "Process parameters optimization for improving surface quality and manufacturing accuracy of binder jetting additive manufacturing process," Rapid Prototyping J., vol. 22, no. 3, pp. 527–538, 2016.

[22] Eichenberger Futuretech AG., http://www.eb-turetech.ch.

[23] [online] https:// en.wikipedia.org/wiki/Skin_effect

[24] Centre for Process Innovation (CPI), http://www.uk-cpi.com.

CHAPTER 4.

3D PRINTED ELECTROMAGNETIC BANDGAP STRUCTURES

4.1 Introduction

This chapter describes a novel procedure to detect liquids with different permittivity using an electromagnetic band gap (EBG) structure and the use of 3D printing (3DP) for the development of non-planar electromagnetic band gap (EBG) structures for antenna applications. A planar EBG structure is modified to introduce trenches between square unit cell elements, cut using a high precision milling machine. The created trenches are filled with liquids of different dielectric permittivities. These change the reflection phase of the EBG structure. A modified circular slot antenna with a coplanar waveguide (CPW) feed line is mounted above the center of the trenched array. By controlling the dielectric permittivities in the trenches, the resonant frequency of the antenna can be tuned. Moreover, a CPW fed antenna is tested on a non-planar EBG substrate, fabricated using additive manufacturing (AM) techniques. Inexpensive fuse filament fabrication (FFF) is used as the fabrication process. Silver loaded conducting ink is employed for the metallic components of the EBG.

EBG structures have been a popular research topic in the antenna and microwave electronics community ever since they were invented more than two decades ago [1]-[3]. EBG structures consist of periodic arrays of elements that are able to resonate at a wavelength significantly larger than the size of their unit cell. The structures are normally realized by periodic dielectric and metallic elements which interact to suppress surface waves generated by incident waves in a particular frequency band. The EBG structures are incorporated with an antenna for various modern wireless communication applications, such as wireless body area networks [4], telemedicine

applications [5], global positioning systems (GPS) [6], and UHF radio frequency identification (RFID) packaging [7], to improve the overall antenna performance. In addition, millimeter wave EBG structures for antennas are introduced in [8], [9].

Reconfigurable or tunable capability is generated by a phase change of an EBG structure using different techniques. Reconfigurable operating frequency [10], [11] and polarization reconfiguration [12], [13] are possible through variation of the EBG characteristics. A combination of them is presented in [14]. In the published literature, their reconfiguration is accomplished by using varactor diodes, PIN diodes or RF microelectromechanical systems (MEMS) switches. Moreover, phase variation across the EBG array has even been realized by employing the mechanical movement of the elements [15] and the use of liquid substrate [16].

Recently, reconfigurable or tunable antennas have been expanded to incorporate flexible devices with sensors and detectors as an important role. A dipole-type antenna is applied to a physical sensor through the permittivity changes of the substrate depending on environmental temperature [17]. The antenna filled with a distilled water is used as the sensing material for a temperature sensor. A switched-beam antenna for a wireless sensor network (WSN) node is incorporated as a power detector [18]. The reconfigurable radiation patterns were provided by controlling the feed lines of the antenna using a switching circuit. The complex dielectric permittivity of liquids is used for low-cost wireless sensing tags using planar substrate integrated waveguide (SIW) technology [19]. The sensor using the SIW structure operates at 4GHz for a wireless sensing system.

FFF has recently been proposed for the development of frequency selective surfaces (FSS) [20]–[21]. In [21], an FSS fabricated by partially metalizing 3D printed shapes was able to reduce the resonant frequency significantly and improve the angle of incidence performance compared with the same but fully metallized design [22].

The chapter is organized as follows. In Section 4.2, the details of the geometry of the unit cell element with trenches and its characteristics are described. After that, the wideband CPW antenna is designed and optimized on a planar EBG array. Section

4.3 studies the frequency tuning ability of the trenched EBG through investigations using a range of liquid permittivities. Simulated and measured results are also presented. Section 4.4 presents a non-planar EBG structure and CPW-fed antenna on additive manufactured substrates. Finally, the chapter concludes in Section 4.5. All designs of the antennas have been optimized and investigated using the finite integration technique (FIT) techniques included in CST Microwave Studio™.

4.2 EBG sensor/detector

4.2.1 Unit cell design with trenches

Figure 4.1 shows the geometry of the unit cell element with their trenches. The square patch is used as the unit cell element which is on the center of the substrate. The phase reflection response of the unit cell element geometry is typically determined by the thickness and relative dielectric permittivity of the substrate. It is designed on an RT/duroid 5870 substrate with dielectric constant of $\varepsilon_r = 2.33$, loss tangent of $tan\,\delta = 0.0005$ and thickness of 3.175mm. A conducting ground plane is on the other side of the substrate. Trenches are introduced by removing the substrate partially surrounding the square patch as shown in Figure 4.1(a). They interrupt surface wave propagation, thereby changing the reflection phase characteristics of the planar unit cell element [23]. Moreover, the depth of the trenches can modify the various surface-wave modes without changing the overall square patch size. By adjusting the patch size, the unit cell element on the planar substrate can be set to give a resonant frequency of 2.45GHz (see below). The gap distance between the conducting square patch sides and the edge of the unit cell element is 2mm in that case. Table 4.1 shows the main design parameters, including those of the unit cell, ie. the original planar EBG structure. In all cases, the conducting patch on the front (Figure 4.1) is 33.45mm square and the ground plane on the back is 37.45mm square.

The computational model for reflection phase characterization of the unit cell element with trenches, simulated using the periodic boundary condition (PBC) option in CST, is shown in Figure 4.1(b). Applying this condition (PBC) on the side walls

and waveguide port at the top provides an incident plane wave, enabling extraction of the dispersion diagram of the unit cell element in an infinite EBG array structure.

(a)

(b)
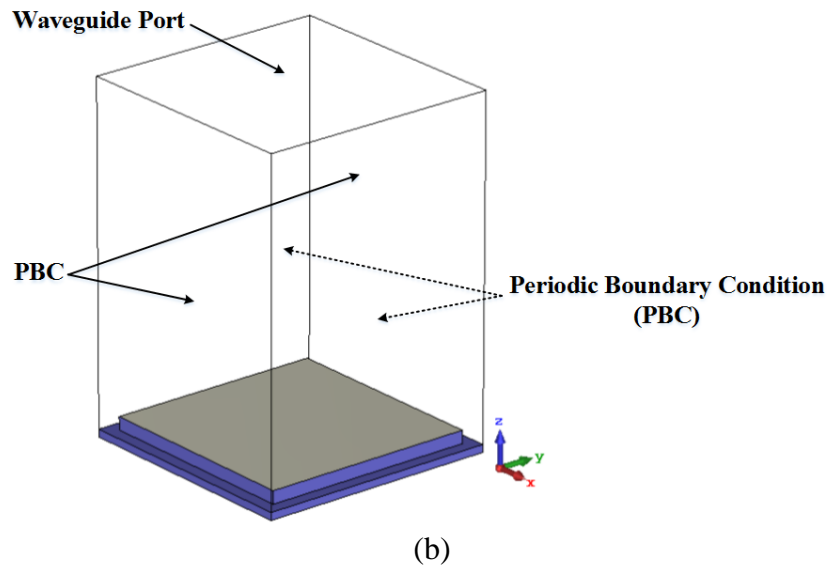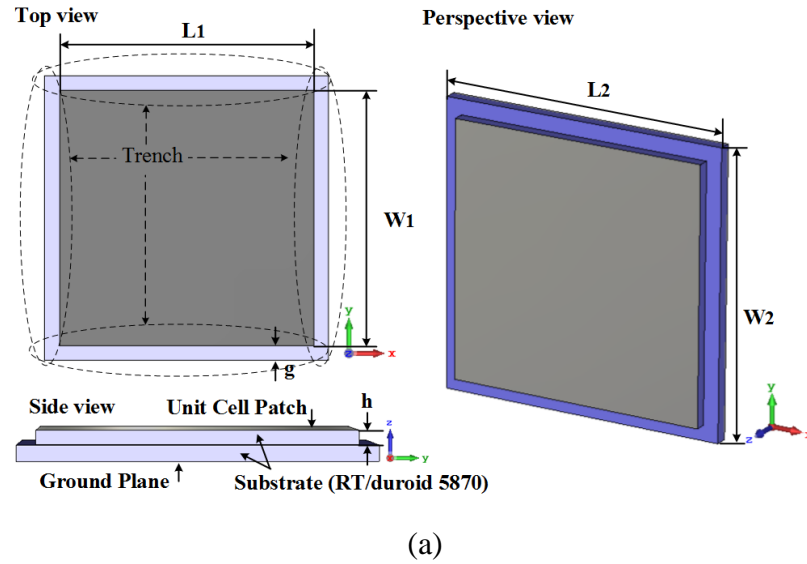
Figure 4.1 (a) Geometry and (b) Infinite model of the unit cell element with trenches.

TABLE 4.1

DIMENSIONS OF UNIT CELL GEOMETRY [mm]

L1	W1	L2	W2	g
33.4	33.4	37.4	37.4	2

63

A periodic structure consisting of square patches can be described by an inductance - capacitor (*LC*) circuit with distributed capacitors and inductors. The capacitor (*C*) is characterized from the gap between the square patches and the inductance (*L*) is determined by the distance between the square patches and the ground plane. The surface impedance and resonant frequency of the periodic structure are calculated respectively as follows [1]:

$$Z = \frac{j\omega L}{1 - \omega^2 LC} \tag{1}$$

$$\omega_0 = \frac{1}{\sqrt{LC}} \tag{2}$$

The resonant frequency can therefore be controlled by the gap between patches and the thickness of the substrate. The bandwidth of the periodic structure is also given by

$$BW = \frac{1}{\eta_0} \sqrt{\frac{L}{C}} \tag{3}$$

where η_0 is the free space impedance. The operational resonant frequency and the bandwidth provided by the unit cell element is normally taken as the frequency of zero degree reflection phase, and the frequency band corresponding to the phase range of -90° to +90°. Over this range, the phase does not critically influence the reflected signal power [24]. Therefore, the operating frequency band can be determined by the design of the square unit cell element.

Figure 4.2 shows the computed reflection phase response of the unit cell element, illustrating the effects of partially removing the substrate, ie. varying the depth of the trenches. The resonant frequency (zero degree phase) increases, but the bandwidth is not changed when the depth is varied from 0 to 2mm. This might be expected, since the effective dielectric permittivity of the substrate is reduced by the partial removal of the substrate from the periphery.
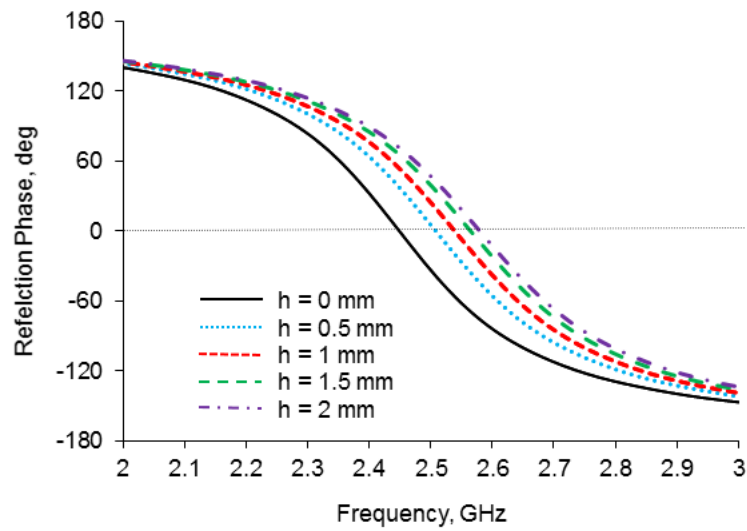
Figure 4.2. Unit cell with trenches: calculated dependence of reflection phase on trench depth (*h*).
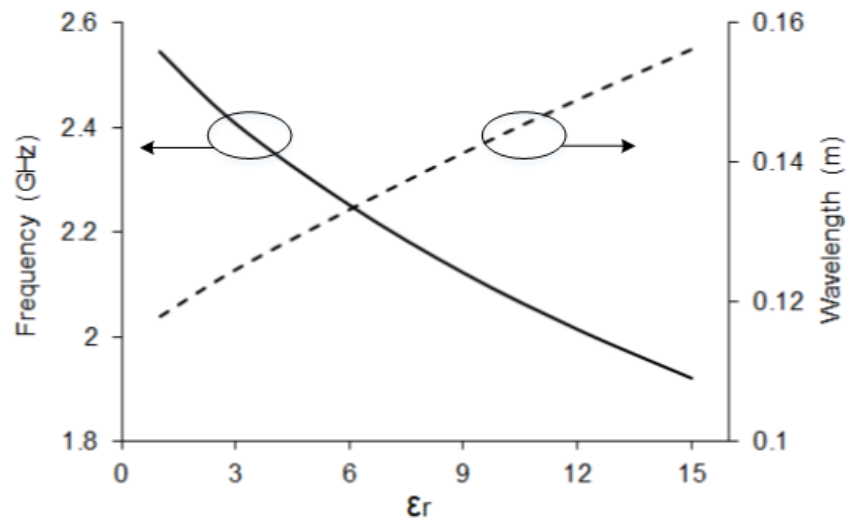
Figure 4.3 Sensitivity of the unit cell element with trenches filled with various dielectric constants (ε_r) on the resonant frequency of reflection phase response and wavelength.

Figure 4.3 shows the computed sensitivity of the unit cell element with the trenches filled with various liquids as indicated by the resonance frequency and wavelength in the reflection phase response. The loss tangent was set to 0 when the dielectric constant was changed from 1 to 15. The depth of the trenches was 1mm. The change

65

in permittivity led to a change in resonant frequency that fits to a quadratic equation. As a sensor, it is best to use a linear variation between the x and y variables. The change in operating wavelength can meet this requirement. This can be expressed by a linear equation of the form:

$$y = 0.0027x + 0.1162 \qquad\qquad (4)$$

where x is the dielectric constant and y is the wwavelength in meters. The R-squared obtained is about 99.7%.

4.2.2 Antenna on planar EBG substrate: preliminary trials

Before applying the unit cell element with trenches (Figure 4.1) to periodic array structures, a CPW antenna on the planar EBG structure is designed and tested in this section. Figure 4.4 shows the geometrical configuration of this antenna. The antenna is composed of a CPW feed line and a modified circular slot structure, on an RT/duroid 5880 substrate with relative permittivity of $\varepsilon_r = 2.20$, loss tangent of $tan\ \delta = 0.0004$ and thickness 1.575mm. Circular components on the CPW feed line generally provide a wide bandwidth [25]. The overall dimension of the antenna is 60 mm x 60 mm. The antenna is placed on the center of the planar EBG structure. This consists of 9 unit cell elements. The dimension of the square patch employed in the unit cell is 33.4mm x 33.4mm, as in Section 4.2.1 and in Figure 4.2. The overall dimension is 111mm x 111mm. The separation between the antenna and the EBG structure is set to 5mm, the optimum for the Bluetooth frequency of 2.45GHz.

The fabricated structure is shown in Figure 4.5. A 50 ohm SMA connector is attached to the feed line. To fix the distance between the antenna and the EBG structure, in initial trials rectangular non-conductive polystyrene formers $(\varepsilon_r \approx 1)$ with thickness of 5mm were attached behind the corners of the antenna and topside of the EBG structure, using double sided adhesive tapes.

(a)   (b)

(c)
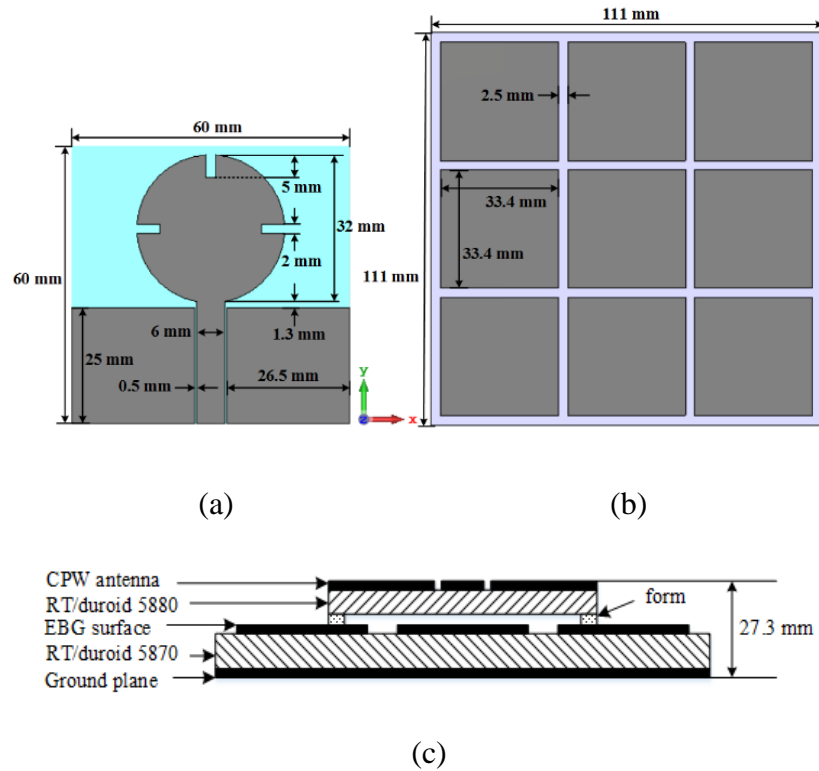
Figure 4.4 (a) Top view of CPW antenna and (b) EBG structure (c) Side view of
CPW antenna on planar EBG structure.
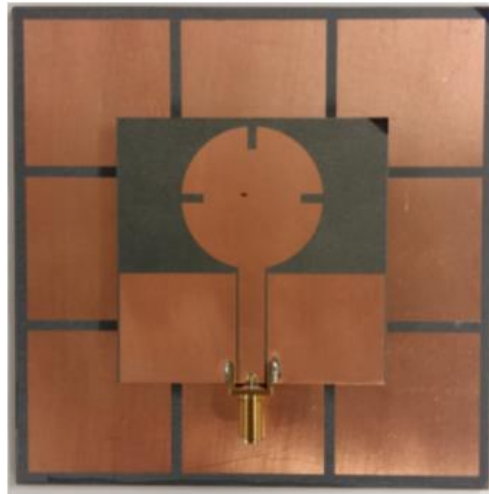
Figure 4.5 Photograph of the fabricated CPW antenna on planar EBG structure.

Figure 4.6 shows a comparison of the reflection coefficient of the antenna, with and
without the EBG structure. An Anritsu 37397C vector network analyzer was used for
the reflection coefficient measurement. The measured frequency range of the antenna

alone is from 1.9GHz to 3.3GHz regarding -10dB of the reflection coefficient response. It has a broad bandwidth of about 52%.
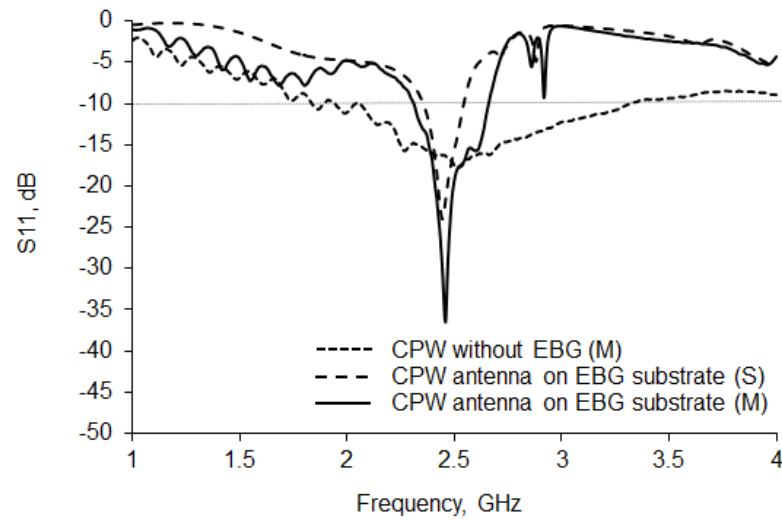
Figure 4.6 Reflection coefficient (*S11*) of the CPW antenna on planar EBG structure.

(S: Simulation result, M: Measurement result)

(a) (b)
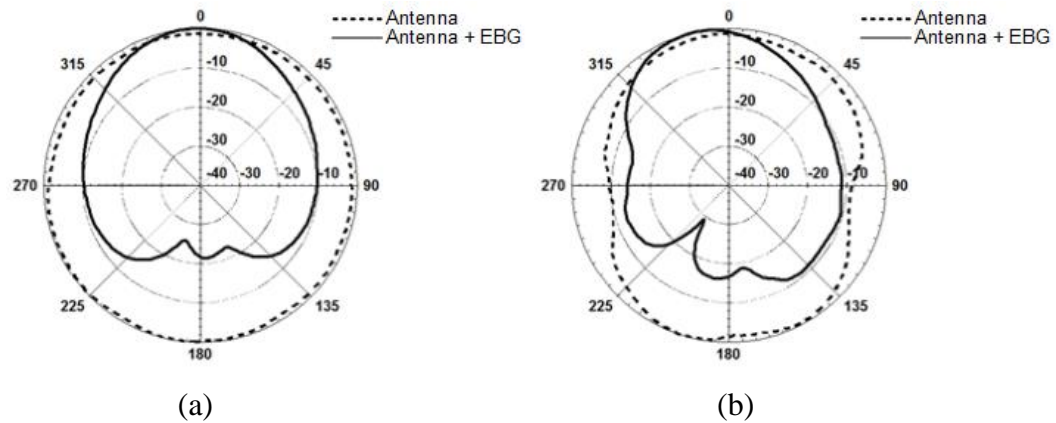
Figure 4.7 Measured radiation pattern of the CPW antenna on planar EBG structure

at 2.45GHz (a) *xz* plane (b) *yz* plane.

On the other hand, the antenna on the planar EBG structure has a measured -10dB bandwidth of 14%, from 2.3GHz to 2.7GHz. The null is at 2.45GHz: -36.5dB. As the results show, the EBG structure provides a narrow bandwidth and deeper resonance compared with the antenna alone. Figure 4.7 presents the measured normalized radiation patterns. They are also compared with the radiation pattern of the antenna alone. They were measured at 2.45GHz in the *xz* and *yz* planes in an anechoic

chamber. As shown in the results, the antenna alone has omnidirectional radiation patterns in all planes. As shown in the results, the antenna alone has omnidirectional radiation patterns in all planes. However, the radiation pattern of the antenna on the planar EBG structure is more directional. The front-to-back ratio of the radiation pattern is improved by about 20dB. Moreover, the gain of the antenna combined with the EBG structure is enhanced by 6.8dB as compared with that of the antenna alone.

4.3 EBG sensor/detector antenna

4.3.1 EBG structure design with trenches

Figure 4.8 presents the geometry of the antenna on the EBG structure with trenches. The concept of a unit cell with trenches (Figure 4.1) is extended to the periodic EBG structure. The overall dimensions of the new array are 111mm x 111 mm, consisting of 9 unit cell elements each of size 33.4mm x 33.4mm, the same dimensions as the previous trial array (Figure 4.4). The difference between them is the presence of the trenches. As mentioned in Section 4.2, these are made by removing material from the substrate. The width and depth of the trenches are referred to as w and h. As shown in Figure 4.2, the unit cell element with 1mm trench depth has zero phase reflection response at 2.54GHz. The same CPW antenna (Figure 4.4) is placed over the trenched array at the height of 5mm.

Figure 4.9 shows the computed reflection coefficients of the antenna for different trench depths (h) ranging from zero to 1.5mm. The width (w) of the trenches is fixed at 2.5mm for the investigation. As the results show, the planar EBG structure ($h = 0$) provides a resonant frequency of 2.45GHz. On the other hand, this frequency changes when the depth of the trenches increases. It increases, but the -10dB bandwidth is almost unaltered, when the depth of the trenches is changed from 0mm to 1.5mm. In the following sections, the width and depth of the EBG structure with the trenches are set to 2.5mm and 1mm. The corresponding resonant frequency and -10dB bandwidth of the EBG structure are 2.54GHz and 7.9% (2.4GHz - 2.6GHz).
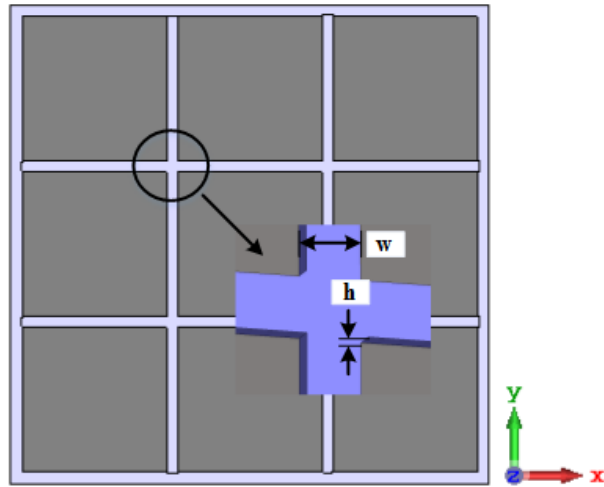
(a)
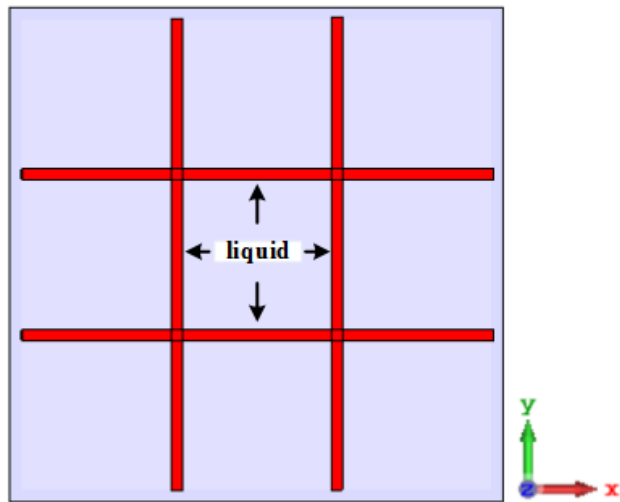
(b)
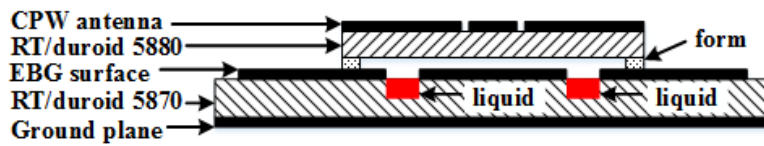
(c)

Figure 4.8 (a) Top view of the CPW antenna and (b) the EBG structure with trenches
(c) Side view of CPW antenna on the EBG substrate with trenches.
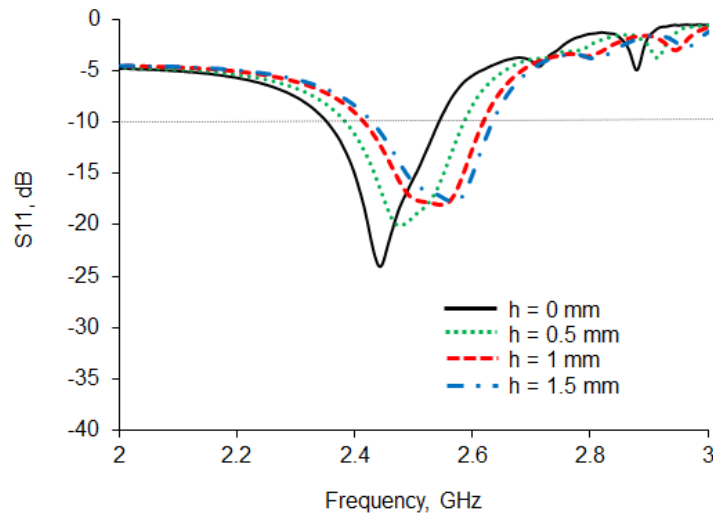
Figure 4.9 Reflection coefficient (*S11*) of the CPW antenna on the EBG structure at different depths (*h*) of the trenches.

4.3.2 Liquids sensor/detector EBG antenna

The empty trenches (ie. air-filled) may be filled with liquids of different dielectric permittivities, to operate the EBG structure as a wireless sensing system, as shown in Figure 4.8(b). A liquid can be characterized by its dielectric constant and loss tangent. To assess its frequency tuning capabilities, the antenna performance of the structure with trenches has been simulated for several trench dielectric constants and loss tangents, as shown in Figure 4.10. Investigations of the influence of these are important for the understanding electromagnetic properties of the overall structure. The dielectric constant of the trenches is varied from 1 to 15, and the loss tangent is fixed to 0. The loss tangent of the trenches is varied from 0 to 0.9, while the dielectric constant is set to 2. As shown in the results, the resonant frequency tunes down when the dielectric constant increases. The -10dB bandwidths are almost unaltered regardless of the changes. On the other hand, the -10dB bandwidths is wider when the loss tangent increases.

Figure 4.11 shows the fitted curve of the sensitivity of the resonance frequency to various trench dielectric constants, covering the range $\varepsilon_r = 1$ to 15. This can be expressed by a linear equation of the form:

71

$$y = 0.0023x + 0.1165 \qquad (5)$$

The dependence is almost linear, with an R-squared of 99.6%. However, the resonant frequency was almost unaffected by the various loss tangents. Four sample liquids giving a range of permittivities were used for the EBG sensor/detector: butan-1-ol, propan-2-ol, and ethanol.
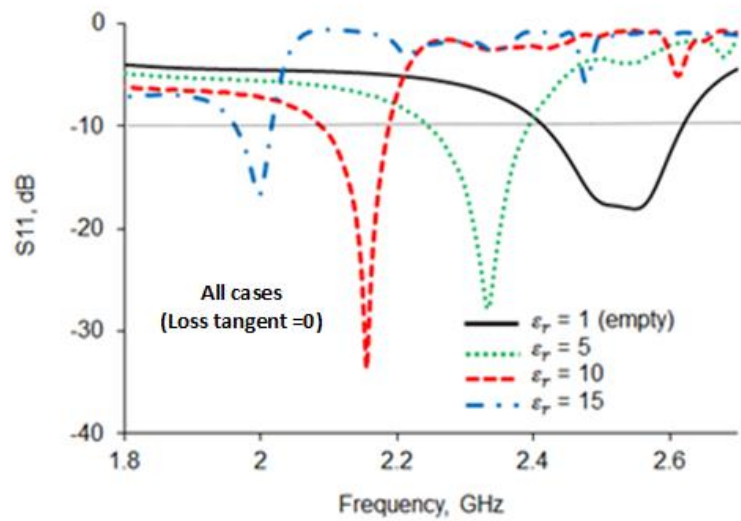
(a)
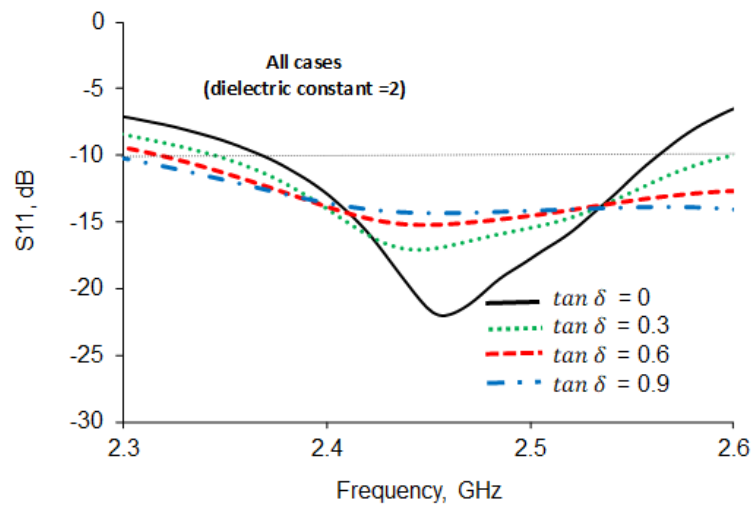
(b)

Figure 4.10 Dependence of reflection coefficient (*S11*) of the CPW antenna on (a) dielectric constant (ε_r) and (b) loss tangent ($tan\ \delta$) of the trenches.

Figure 4.11 Sensitivity of the CPW antenna on the EBG structure: simulated dependence of the resonant frequency and wavelength on trench dielectric constant.

Three sample liquids giving a range of permittivities were used for the EBG sensor/detector: butan-1-ol, propan-2-ol, and ethanol. Their dielectric properties were chosen from the report [26]: $\varepsilon_r = 3.57$ and $tan\ \delta = 0.47$ for Butan-1-ol, $\varepsilon_r = 3.80$ and $tan\ \delta = 0.64$ for Propan-2-ol and $\varepsilon_r = 6.57$ and $tan\ \delta = 0.96$ for ethanol, at 2.5GHz and 20ºC. Figure 4.12 shows the simulated reflection coefficients when the trenches were filled with the three liquids.
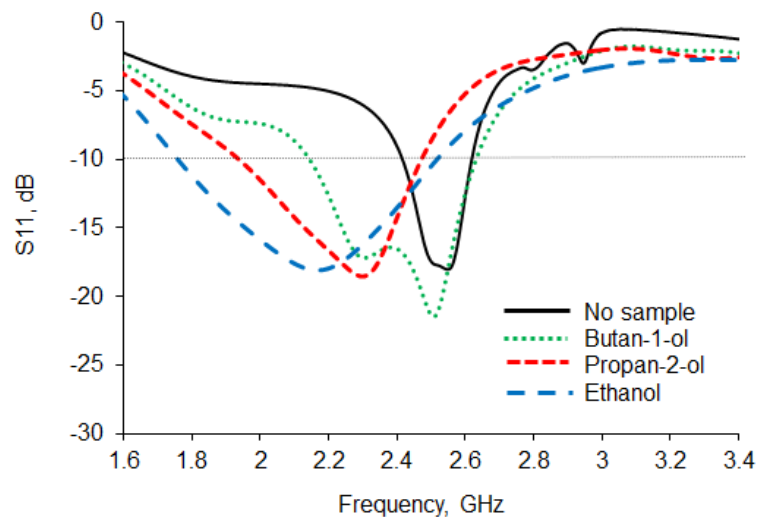
Figure 4.12 Reflection coefficient ($S11$) of the antenna with trenches filled with different sample liquids.

73

In the CST Microwave Studio^{TM}, the trenches not filled with any liquid (empty) assume the $\varepsilon_r = 1$, $tan\,\delta = 0$. As shown by the results, the resonant frequency changes according to the different sample liquids. There is a significant effect. As might be expected, the null frequencies with butan-1-ol, propan-2-ol and ethanol are on the left side compared to the one (empty). In particular, ethanol provides the greatest frequency shift but the worse bandwidth.

4.3.3 Fabrication and Measurement

To verify the EBG sensor/detector technique based on the sensitivity to liquid permittivity, the structure with trenches was fabricated. Figure 4.13 shows a photograph of it. The gaps between the square patches on a substrate were cut out and the depth of trenches adjusted using a 2.5mm cutter on the high precision milling machine. The trench dimensions were 2.5mm x 105.4mm with depth 1mm. The CPW antenna was placed over the EBG structure. The distance between the antenna and the EBG structure with trenches is 5mm fixed by rectangular non-conductive polystyrene formers on the edges of the antenna substrate using double-sided adhesive tapes.

The reflection coefficients from the empty trenches were measured and are compared with simulated results in Figure 4.14. They also are investigated with the results of the CPW antenna on the planar EBG structure. The difference between the simulated and measured results at the resonant frequency is less than 1%. However, the -10dB measured bandwidth is wider than the simulated one. The measured reflection coefficient is also deeper than the simulated one. The discrepancy between the simulated and measured results may be due to fabrication errors related to accuracy of the trenches made by a milling machine. The trenched EBG structure provides a resonant frequency of 2.53GHz and a -10dB bandwidth of 10.3%. The corresponding value of the planar structure is 2.45GHz and 13.7%.
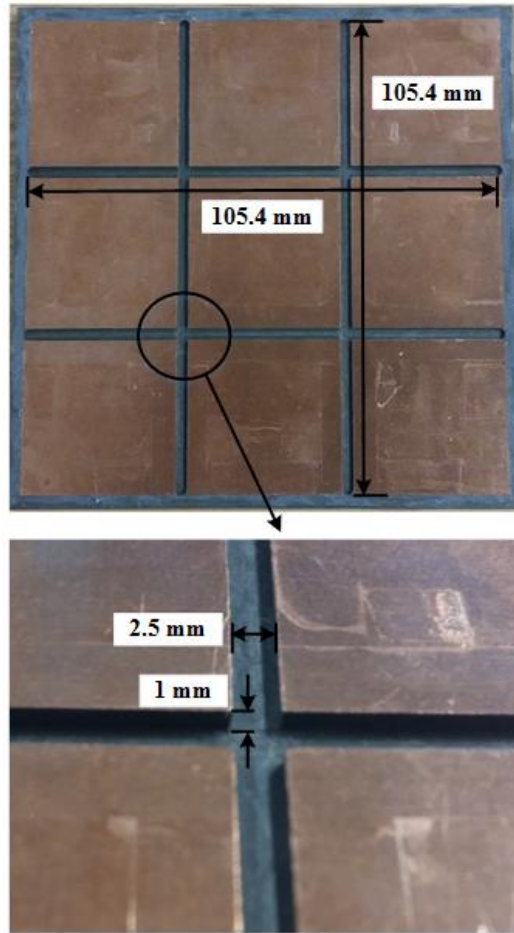
Figure 4.13 Photograph of the fabricated EBG structure with empty trenches.
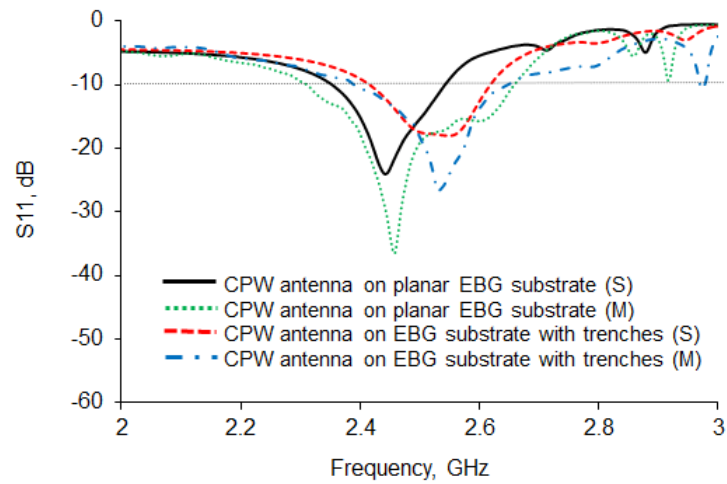
Figure 4.14 Reflection coefficient (*S11*) of the CPW antenna on the EBG substrate
with trenches not filled with sample liquids. (S: Simulation, M: Measurement)

For the EBG sensor/detector, preventing liquid leakage from the trench is a significant issue. Figure 4.15 shows the fabricated structure. A thin adhesive masking tape (*Tesa® 51408* Orange Masking Tape) with a thickness of 60μm was used to seal the liquids in the trenches. In the measurement, there was no apparent difference with and without attached adhesive tapes.
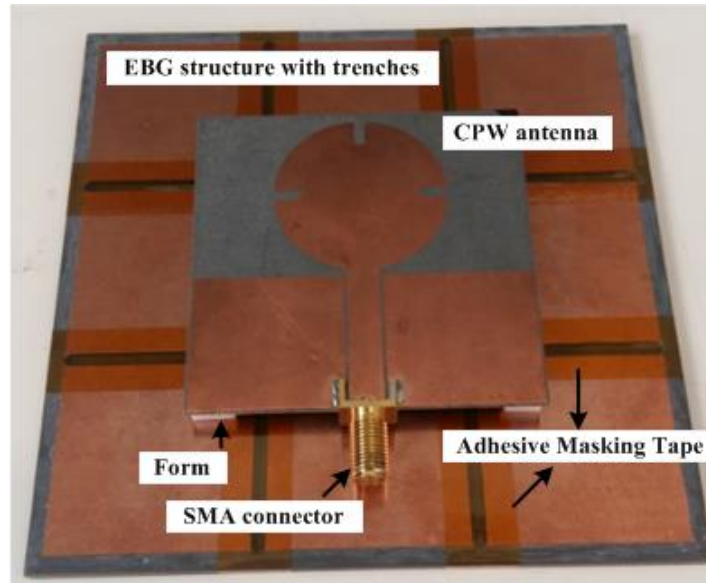
Figure 4.15 Photograph of the fabricated antenna on the trenched EBG structure.

Three different dielectric permittivities of liquids (butan-1-ol, propan-2-ol, and ethanol) are used for the analysis of the EBG array, and each of them has different dielectric constant and loss tangent. The three different liquids were put into the trenches using a disposable syringe, at room temperature. The radiation patterns were measured in anechoic chamber. The entire setup was kept at a constant room temperature to ensure constant permittivities of the liquids. The input reflection coefficients of the antenna with the three liquids were measured using an Anritsu 37397C vector network analyzer and the results are presented in Figure 4.16. With butan-1-ol, propan-2-ol, and ethanol, the measured resonant frequencies were 2.53GHz, 2.40GHz, and 2.26GHz with a reflection coefficient of 21.95dB, 16.07dB, and 17.70dB respectively, ie. as might be expected the frequencies decline as ε_r increases.

There was no appreciable shift of the resonant frequency between no sample (empty) and butan-1-ol, while a frequency shift of 130MHz was observed between butan-1-ol and propan-2-ol. The shift between propan-2-ol and ethanol was 140MHz. It is clear that the different liquids provided a reflection frequency tuning capability for the antenna. The *S11* profile is noticeably different in term of null depth and bandwidth as well as null frequency allowing different material to be identified. However, it is also observed that the measured results differ from the simulated ones (Figure 4.12). The differences may be due to errors in the fabrication process and in the quantity, quality and temperature of the filling liquids in the trenches compared with ideal simulated cases.

Figure 4.17 presents measured normalized antenna radiation patterns for two liquids (propan-2-ol, and ethanol). It is observed that the EBG structure improves the directivity in all cases. However, there are measured losses. The peaks of the patterns were reduced. Compared with the unfilled case the maximum value with the liquids is reduced by about 15dB.
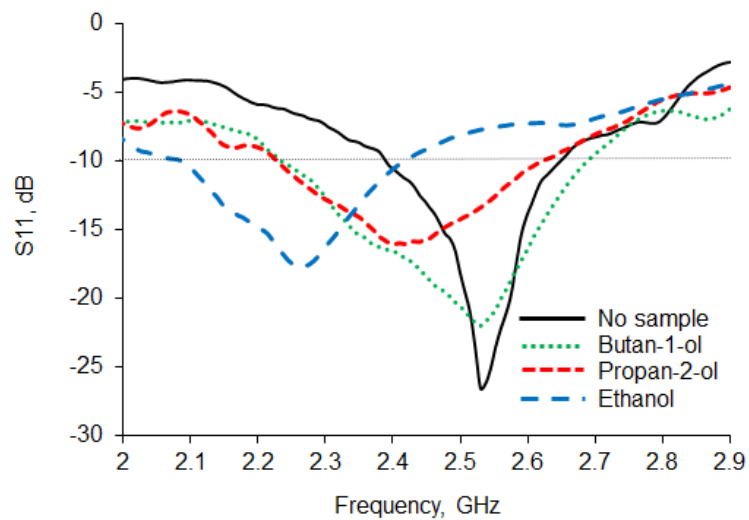
Figure 4.16 Measured reflection coefficient (*S11*) of the CPW antenna on the EBG substrate with trenches filled with different liquids.

(a)   (b)
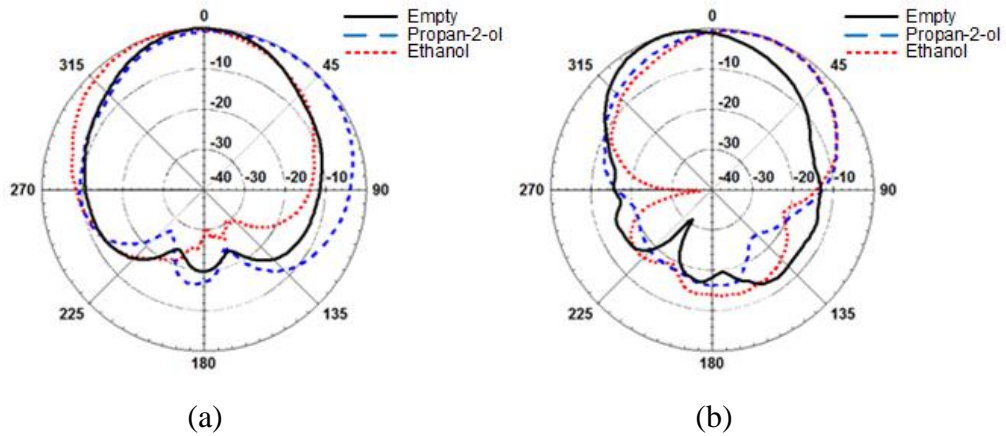
Figure 4.17 Measured radiation patterns of the CPW antenna on the EBG structure
with trenches (a) unfilled (b) Propan-2-ol (c) Ethanol.

A possible use is illustrated in Figure 4.18. In this case, the sensor is placed in a
flooring or drainage system where liquids may fall by precipitation and may be
guided towards the EBG sensor. This liquids will fall into the trenches which will be
filled. The filling of the tranches will lead to a change in the resonant frequency of
the EBG. This change could be picked up through the change of S_{11} of the antenna
and also through the radiation pattern.
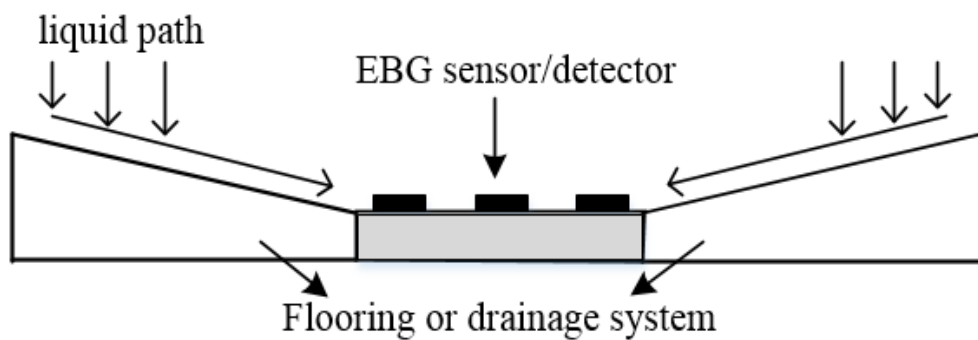
Figure 4.18 Arrangement of the potential EBG sensor/detector.

4.4 3D printing technique for the development of non-planar EBG for antenna applications

In this section, an AM technique is proposed for the development of non-uniform EBG substrates for antenna applications. A relatively simple structure consisting of flat metallic patches and trenches between the patches illustrates the principle. A commercial FFF machine with low-cost polylactic acid (PLA) plastic is used for the fabrication of the substrate and silver loaded paint for the metallic patches. A 3D printed stencil allows the patterning of the patches on the substrate. A CPW antenna is tested on the EBG substrate. The PLA material has $\varepsilon_r = 2.47$ and $tan\,\delta = 0.007$ [28]. All simulation results have been carried out with CST Microwave Studio$^{\text{TM}}$. The emphasis in this Section is on the demonstration of a simple AM process for the fabrication of complex EBG geometries for antenna applications.

4.4.1 Antenna and EBG design

The EBG is a periodic array of flat square patches with trenches between them. Figure 4.19(a) shows the geometry of the unit cell. Each upper patch has side dimensions of 35 mm, and is arranged on a unit cell of 37×37 mm^2. The depth of the trenches is 0.4 mm and the total thickness of the substrate is 2 mm. Figure 4.19(b) shows the simulated reflection phase of the EBG structure. The unit cell was designed for a resonance frequency of 2.45GHz, where the phase angle is zero. The depth of the trenches (h) can control the resonance frequency without changing the overall patch size.

79
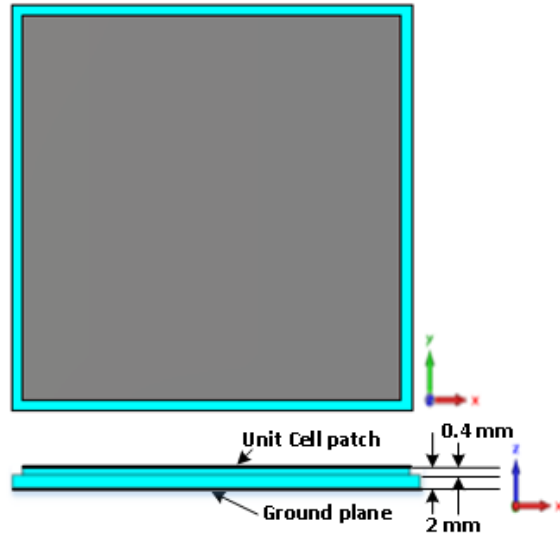
(a)
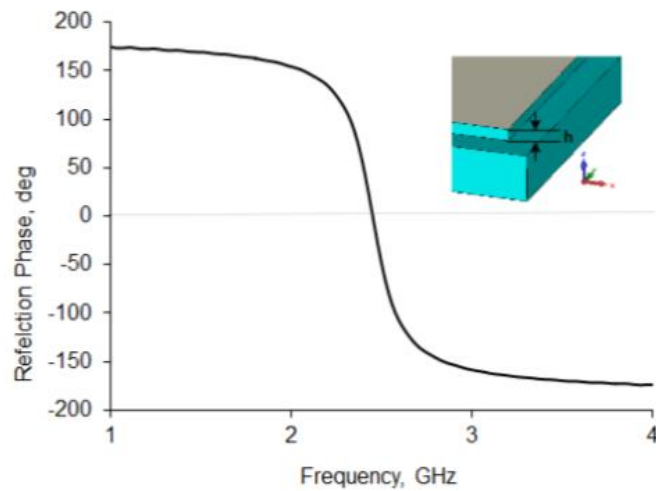
(b)

Figure 4.19 Non-planar EBG structure (a) geometry, (b) calculated reflection phase

To test the effect of such an EBG, a wideband CPW antenna was set at the center and at a distance of 1 mm over 3×3 patch cells of the EBG structure as shown in Figure 4.20(a). The overall size of the EBG substrate was 120×120 mm^2. The antenna was designed to cover frequencies higher than 2GHz in free space with reflection coefficient levels (S11) of < -10 dB. The CPW antenna's overall size is 60×60 mm^2, the ground plane patches are 26.5×25 mm^2, and the feed line 6×28.3 mm^2. The radius of the circular radiator is 6.25 mm^2, and the gap between the feed line and the ground was 0.5 mm. The PLA substrate had a thickness of 2 mm.

(a)   (b)

(c)
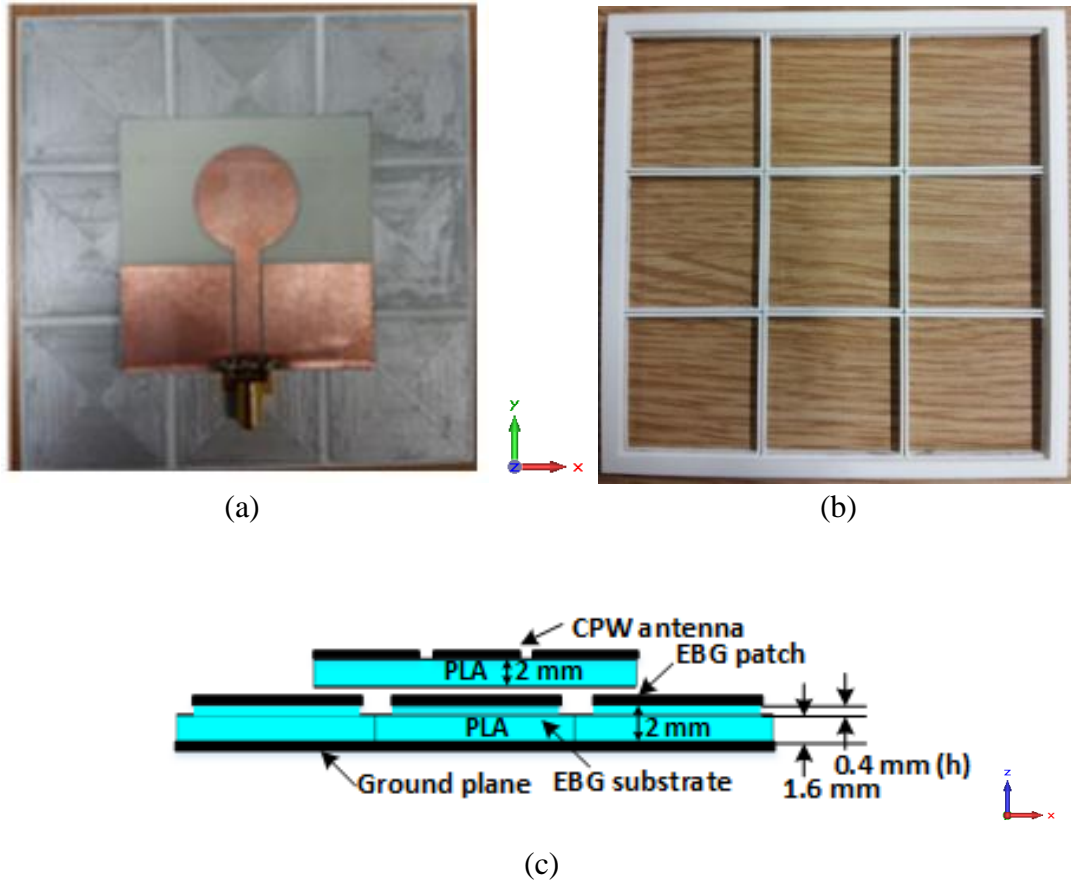
Figure 4.20 Coplanar waveguide (CPW) fed on EBG structure
(a) configuration, (b) EBG stencil, (c) side view with dimensions.

The metallic components of the antenna were etched on a copper clad Mylar®
polyester film and attached to the PLA substrates using double sided tape. These
substrates were made with an Ultimaker2 3D printer. Their density was set to 100%
in the machine data. The stencil shown in Figure 4.20(b) was also 3D printed. This
fitted tightly on the EBG's substrate. Silver-loaded conducting ink was evenly spread
on the latter by hand, using the stencil. The measured average resistance between the
ends of the nine patches was 1 Ω. Curing the EBG in an oven for about 15 min and
90° temperature was able to reduce the resistance to <0.5 Ω. The side view of the
CPW antenna on the non-planar EBG structure is illustrated in Figure 4.20(c). The
antenna substrate had four printed 2×1 mm^2 spacers to keep the 1 mm distance
between the antenna and EBG substrate.

4.4.2 Dielectric properties of commonly used plastics in 3D printing

In the section, the dielectric properties of two materials commonly used in 3D printing are analysed using the transmission/reflection method with a waveguide (Figure 4.21). The measurement configuration and the overall process follow the description provided in [27]. Figure 4.22 presents the experimental set-up and the 3D printed materials. Polylactic acid (PLA) and stereolithography (SLA) slabs fabricated by an Ultimaker 3D printer and a Form 1+ printer, respectively, were used as the experimental samples. A sample dielectric slab that completely fits the cross-section of the waveguide was placed at its centre. The transmission coefficient (S_{21}) were measured at the two SMA ports of the waveguide, with the frequency range set at 4-5 GHz. The dielectric constant and the loss tangent were obtained from the amplitude and the phase of S_{21} [27].
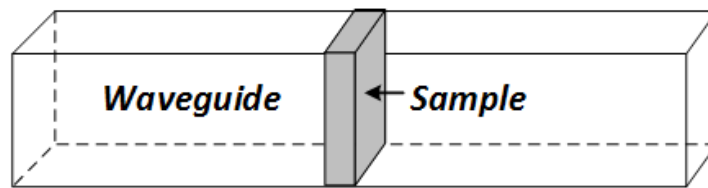
Figure 4.21 Transmission/reflection method using a waveguide

(a)   (b)
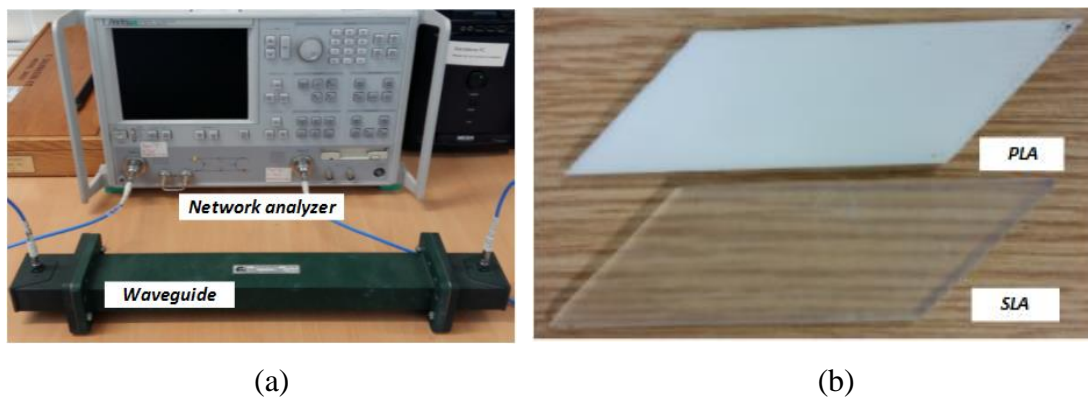
Figure 4.22 Measurement configuration. (a) Network analyzer and waveguide. (b) 3D printed materials.

Figure 4.23 illustrates that, based on the experimental measurements, the dielectric constants of PLA and SLA were approximately 2.4 and 3.0, respectively, over the entire frequency range. In addition, the loss tangents for PLA and SLA were at 0.000045 and 0.000036, respectively. The measurement results of the loss tangent were not reliable for PLA and SLA.
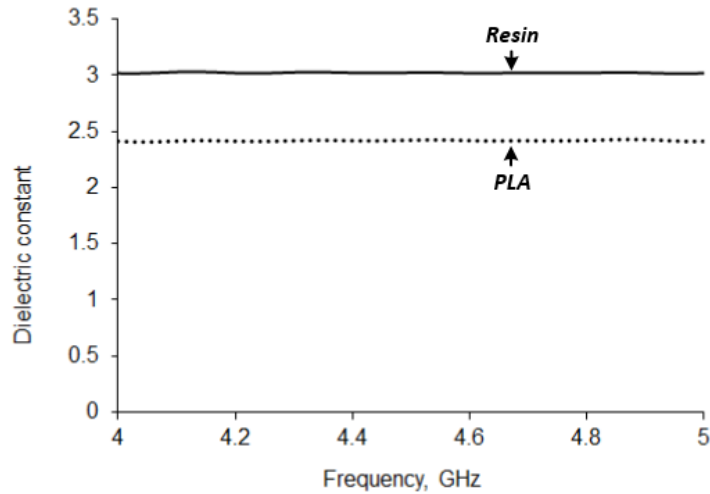
Figure 4.23 Dielectric constants for PLA and SLA

Recently, four dielectric materials regularly used for 3D printing were investigated by using a contact probe method [28]: polylactic acid (PLA), stereolithography (SLA), acrylonitrile butadiene styrene (ABS), and selective laser sintering (SLS). Their dielectric constants and loss tangents were reported as $\varepsilon_r = 2.47$ and $tan\,\delta = 0.007$ for PLA, $\varepsilon_r = 2.48$ and $tan\,\delta = 0.006$ for ABS, $\varepsilon_r = 2.83$ and $tan\,\delta = 0.038$ for SLA and $\varepsilon_r = 2.6$ and $tan\,\delta = 0.001$ for SLS. As can be seen, the dielectric properties of PLA and SLA reported in [28] differed slightly compared with the values obtained from the transmission/reflection method using a waveguide presented in the current study. This indicates that the dielectric properties of commercially available materials can vary and change during the manufacturing process. Therefore, the properties of dielectric materials need to be examined carefully in the fabrication of antennas.

4.4.3 Antenna performance

Figure 4.24 presents the simulated and measured reflection coefficient (S_{11}) of the antenna in free space, on the EBG structure, and on an equivalent perfect metallic ground (PEC). Simulated and measured results compare very well. In free space, the -10 dB bandwidth spans from 2.01GHz to 3.15GHz. On the perfect metallic ground (PEC) the antenna is clearly mismatched. On the other hand, the combined CPW antenna and EBG spans from 2.32GHz to 2.53GHz, filtering out most frequencies beyond the 2.4GHz WLAN band. At 2.45GHz the impedance match shows an improvement of more than 10dB compared with that of the antenna in free space.
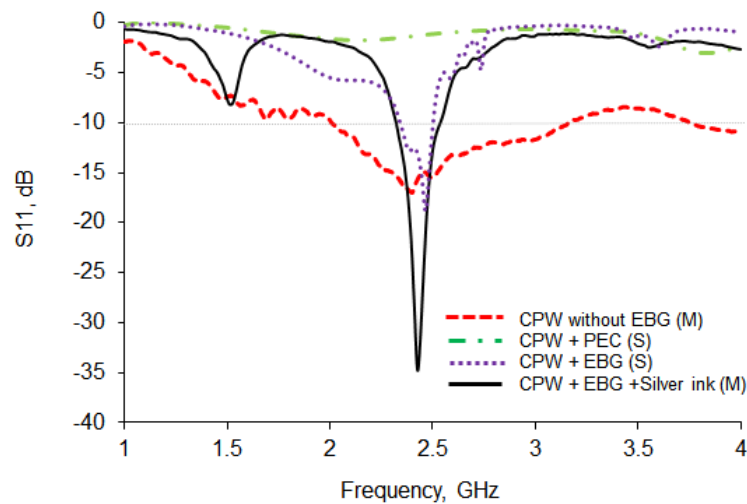
Figure 4.24 Measured (M) and simulated (S) reflection coefficient (S_{11})

The measured *xz* and *yz* plane radiation patterns for the antenna in free space and on the EBG structure are shown Figure 4.25. The back lobe of the radiation pattern decreased by over 10 dB while the maximum gain increased by 2.44 dB when the antenna was on the EBG substrate. The squinting from the beam in Figure 4.25(a) arises from the non-symmetry of the structure in Figure 4.20(a) about the (*x, z)* plane and the effect of the feed cable.
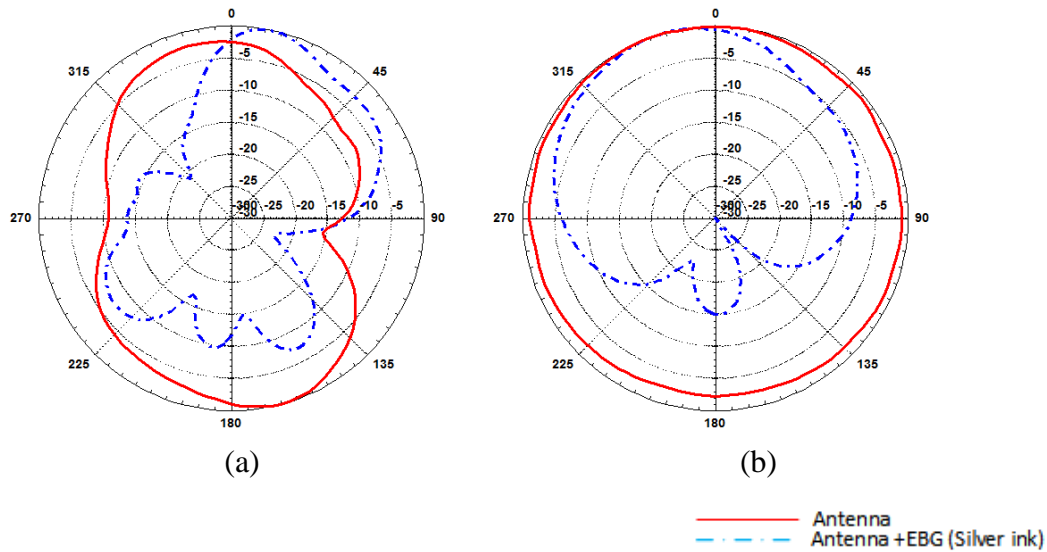
Figure 4.25 Measured radiation pattern for the CPW antenna in free space and on the non-planar EBG structure (a) *xz* plane, (b) *yz* plane

4.5 Conclusions

First of all, a novel reconfigurable EBG technique suitable for sensing applications has been demonstrated in the chapter. The reconfigurable behavior of the EBG is obtained by creating trenches between the unit cells and filling them up with liquids of different permittivities. The changes in permittivity of the liquids produce a change in the resonant frequency of EBG structure. This EBG sensor could be used as a standalone solution where the reflective signal can be evaluated. An alternative solution is to use an antenna in close proximity of the EBG structures. The latter was investigated in the chapter. A CPW antenna was designed and located on the center of the EBG structure, with the trenches filled with the three different sample liquids: butan-1-ol, propan-2-ol, and ethanol. The frequency tuning range obtained was from 2.26GHz to 2.53GHz. The sensor/detector technique can be integrated as part of a wireless sensor network.

Secondly, the applicability of inexpensive AM technologies to the development of non-planar EBG substrates for antenna applications has been described. A relatively simple structure consisting of metallic patches with trenches has been used for this demonstrator. PLA plastic is a low-cost material suitable for this application. Silver-

loaded conducting ink was painted on the 3D printed non-planar EBG structure using an also printed EBG mask. Measurements and simulations showed that this particular demonstrator is capable of providing significant antenna matching and gain improvements that in turn can deliver significant improvements in wireless communications. Results could be further improved by using inks with higher conductivity. This technique could be applied to more complex 3D EBG structures, an issue that the authors are currently investigating.

References

[1] D. Sievenpiper, L. Zhang, R. F. Broas, N. G. Alexopolous, and E. Yablonovitch, "High-impedance electromagnetic surfaces with a forbidden frequency band, " IEEE Trans. Microw. Theory Tech.., vol. 47, no. 11, pp. 2059–2074, Nov. 1999.

[2] D. Sievenpiper, J. Colburn, B. Fong, J. Ottusch, J. Visher, "Holographic artificial impedance surfaces for conformal antennas", in IEEE Antennas and Propagation Symposium Digest, 2005.

[3] A. P. Feresidis, G. Goussetis, S. Wang, and J. C. Vardaxoglou, "Artificial magnetic conductor surfaces and their application to low-profile high gain planar antennas, " IEEE Trans. Antennas Propag., vol. 53, no. 1, pp. 209–215, Jan. 2005.

[4] S. Zhu and R. Langley, "Dual-Band Wearable Textile Antenna on an EBG Substrate," IEEE Trans. Antennas Propag., vol. 57, pp. 926-935, 2009.

[5] H. R. Raad, A. I. Abbosh, H. M. Al-Rizzo, and D. G. Rucker, "Flexible and Compact AMC Based Antenna for Telemedicine Applications," IEEE Trans. Antennas Propag., vol. 61, pp. 524-531, 2013.

[6] X. L. Bao, G. Ruvio, M. J. Ammann, and M. John, "A novel GPS patch antenna on a fractal hi-impedance surface substrate," IEEE Antennas Wireless Propag. Lett., vol. 5, no. 1, pp. 323–326, Dec. 2006.

[7] B. Gao, C. H. Chen, and M. M. F. Yuen, "Low-cost passive UHF RFID packaging with electromagnetic band gap (EBG) substrate for metal objects," in Proc. Electronic Components and Technology Conf. ECTC'07, 2007, pp. 974–978.

[8] M. J. Al-Hasan, T. A. Denidni, and A. R. Sebak, "Millimeter-Wave EBG-Based Aperture-Coupled Dielectric Resonator Antenna," IEEE Trans. Antennas Propag., vol. 61, pp. 4354-4357, 2013.

[9] M.J. Al Hasan, T.A Denidni and A. R. Sebak, "Millimeter-wave EBG antenna pattern diversity", in IEEE Antenna Propag. Soc. Inter. Symp., Orlando, FL, USA, 2013, pp 272-273.

[10]   H. J. Lee, K. L. Ford, and R. J. Langley, "Dual band tunable EBG," Electron. Lett., vol. 44, no. 6, pp. 392–393, Mar. 2008.

[11]   B. Schoenlinner, A. Abbaspour-Tamijani, L. C. Kempel, and G. M. Rebeiz, "Switchable low-loss RF MEMS Ka-band frequency-selective surface," IEEE Trans. Microw. Theory Tech., vol. 52, pp. 2474-2481, 2004.

[12]   F. Yang and Y. Rahmat-Samii, "Polarization-dependent electromagnetic bandgap surfaces: Characterization, designs, and applications," in 2003 IEEE AP-S Dig., 2003, pp. 339–342.

[13]   W. Yang, W. Che, H. Jin, W. Feng, and Q. Xue, "A Polarization-Reconfigurable Dipole Antenna Using Polarization Rotation AMC Structure," IEEE Trans. Antennas Propag., vol. 63, pp. 5305-5315, 2015.

[14]   B. Liang, B. Sanz-Izquierdo, E. A. Parker, and J. C. Batchelor, "A Frequency and Polarization Reconfigurable Circularly Polarized Antenna Using Active EBG Structure for Satellite Navigation," IEEE Trans. Antennas Propag., vol. 63, pp. 33-40, 2015.

[15]   D. Sievenpiper, J. Schaffner, J. J. Lee, and S. Livingston, "A steerable leaky-wave antenna using a tunable impedance ground plane," IEEE Antennas Wireless Propag. Lett., vol. 1, pp. 179-182, 2002.

[16]   A. C. d. Lima, E. A. Parker, and R. J. Langley, "Tunable frequency selective surface using liquid substrates," Electron Lett., vol. 30, pp. 281-282, 1994.

[17]   F. Yang, Q. Qiao, J. Virtanen, A. Z. Elsherbeni, L. Ukkonen, and L. Sydänheimo, "Reconfigurable sensing antenna: A slotted patch design with temperature sensation," IEEE Antennas Wireless Propag. Lett., vol. 11, pp. 632–635, 2012.

[18]   L. Catarinucci, S. Guglielmi, R. Colella, L. Tarricone, "Compact switched-beam antennas enabling novel power-efficient wireless sensor networks", IEEE Sensors J., vol. 14, no. 9, pp. 3252-3259, Sep. 2014.

[19] H. Lobato-Morales, A. Corona-Chávez, J. L. Olvera-Cervantes, R. A. Chávez-Pérez, and L. José, "Wireless Sensing of Complex Dielectric Permittivity of Liquids Based on the RFID," IEEE Trans. Microw. Theory Tech., vol. 62, pp. 2160-2167, 2014.

[20] B. Sanz-Izquierdo and E. A. Parker, "3D printing technique for fabrication of frequency selective structures for built environment," Electron Lett., vol. 49, pp. 1117-1118, 2013.

[21] B. Sanz-Izquierdo and E. A. Parker, "Frequency selective surfaces formed by partially metalising 3D printed shapes," in Antennas and Propagation (EuCAP), 2015 9th European Conference on, 2015, pp. 1-4.

[22] B. Sanz-Izquierdo and E. A. Parker, "3-D printing of elements in frequency selective arrays," IEEE Trans. Antennas Propag., vol. 62, pp. 6060-6066, 2014.

[23] S. B. Yeap and Z. N. Chen, "Microstrip Patch Antennas With Enhanced Gain by Partial Substrate Removal," IEEE Trans. Antennas Propag., vol. 58, pp. 2811-2816, 2010.

[24] A. P. Feresidis, G. Goussetis, W. Shenhong, and J. C. Vardaxoglou, "Artificial magnetic conductor surfaces and their application to low-profile high-gain planar antennas," IEEE Trans. Antennas Propag., vol. 53, pp. 209-215, 2005.

[25] J. Liang, L. Guo, C. C. Chiau, X. Chen, and C. G. Parini, "Study of CPW-fed circular disc monopole antenna for ultra wideband applications," IEE Proc. Microw. Antennas Propag., vol. 152, pp. 520-526, 2005.

[26] A. P. Gregory and R. N. Clarke, "Tables of the complex permittivity of dielectric reference liquids up to 5 GHz," CETM, Teddington, U.K., Nat. Phys. Rep. 33, Jan. 2012.

[27] O. O. Rakibet, 'Epidermal and Body-Worn Antennas', University of Kent, 2015.

[28] Index SAR, http://www.indexsar.com/, accessed Aug 2017.

CHAPTER 5.

INKJET PRINTED ANTENNAS FOR DISPOSABLE UNMANNED AERIAL VEHICLES

5.1 Introduction

Disposable drones are currently attracting significant research interest [1], [2]. These drones should be made of inexpensive and degradable materials such as paper or cellulose based materials. Components such as inertial sensors and elevons can be integrated into such drones using AM techniques [2]. Furthermore, actuators and potential motors have been developed for this application [3]. Unmanned aerial vehicles (UAVs), otherwise known as drones, are receiving increased interest within various applications and fields including the food and agricultural sector, industry electronics, intelligent transportation systems and safety and security [4]-[11]. Recently, scenarios of reliable communication and networking have been investigated for improving the coverage and capacity of the wireless system [10], [11] used in drones. For large coverage capabilities, drones sometimes require omnidirectional antennas where signal levels are mostly equal in all directions. Therefore, antennas are selected, designed and developed to meet these specifications in both commercial and defense applications. The antennas are mounted either on the inside or the outside of drones. One or more elements are used to operate at the wireless communications bands related to the GPS, WIFI and LTE technologies [12]-[20]. A simple, low profile and wide-beam width conformal antenna on a UAV is presented in [16]. The vertically polarized monopole antenna is installed on the shell structure of a drone made of carbon fiber materials. A simple structure with a radiation, feeding strips and a reflector is applied to UAVs in [17]. In this case, the antenna radiation is polarized horizontally and is similar to a dipole

antenna. Conducting plates are used as an antenna and a reflector. A planar segmented loop patch antenna on a FR4 substrate for UAV application is presented in [18]. The antenna has omnidirectional and quasi-omnidirectional radiations over the wide bandwidth. The experimental performance of a lightweight blade antenna has recently been proposed for UAV application [19].

This chapter presents an investigation of inkjet-printed antennas for foldable and disposable drones. Inexpensive fabrication equipment, and silver nanoparticle ink is used for the fabrication of the antenna which is deposited on photo paper to make the structure of the drone. This chapter is organized as follows: Firstly, a basic design concept for foldable antenna on UAVs is provided in Section 5.2. The antenna is tested unfolded and then folded when integrated onto the airplane in order to examine the effect of bending on performance. Two configurations of the folded antenna on the plane are analyzed. Ongoing work is to optimize the antenna for different remote controller locations and also apply new origami folding techniques for paper UAVs in Section 5.3 and Section 5.4. They present an optimized antenna design for a more general case and discusses its output performance. It includes a surface analysis of the deposited metallic layers on the paper substrate. Finally, a conclusion is included in Section 5.5. The design of the antennas and their optimization have been carried out using the finite integration technique (FIT) included in CST Microwave Studio$^{\text{TM}}$.

5.2 Folded antenna on paper Airplane

This section presents an inkjet-printed dual-band antenna on paper substrate for origami paper UAVs. The antenna pattern is printed directly onto photo paper using inexpensive inkjet printing technology. The planar antenna is first printed and tested. Then, the antenna is tested when folded on a larger paper sheet, which takes the form of a paper airplane. The antenna is folded on the inside and then to the outside, to investigate the effect of folding on antenna performance and also to find the best condition for communication.

5.2.1 Initial design of folded antenna design

Figure 5.1 shows the geometry of the dual band CPW-fed antenna. The target frequencies of the proposed antenna are 2.4 GHz and 5.2 GHz for the wireless LAN band. The antenna consists of a CPW line and a semicircle with an inner square slot. The semicircle produces the wide bandwidth necessary for the higher frequency bands. The square shifts the lower mode to the 2.4 GHz and filters intermediate bands. The dielectric constant and thickness of the paper used as substrate were set at 3 and 0.177±12μm mm respectively. A coaxial cable is used in the simulations in order to replicate the measurement conditions [20].

(a)   (b)
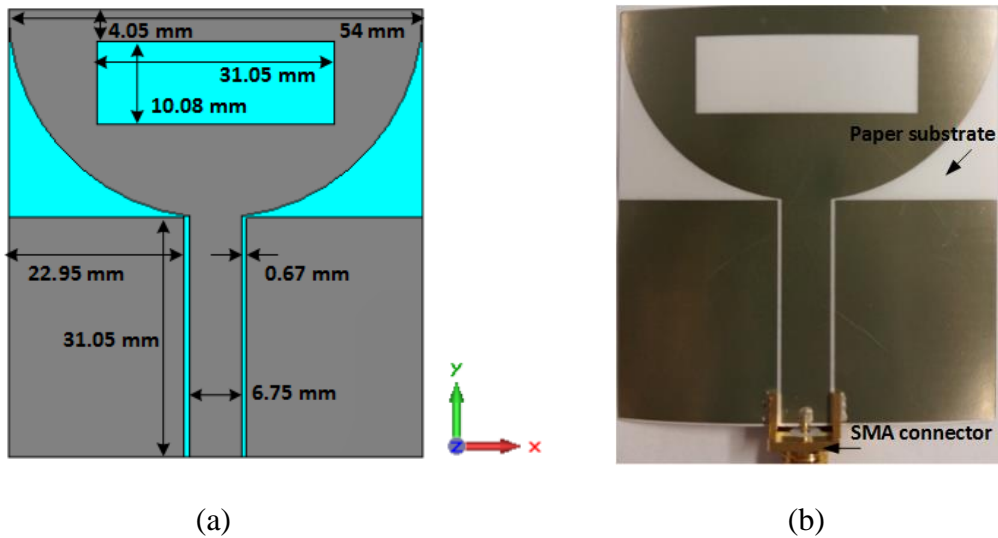
Figure 5.1 Dual band inkjet-printed CPW-fed antenna on paper substrate (a) antenna dimensions (b) photograph of fabricated antenna with SMA feed connector

The substrate of the designed dual band CPW-fed antenna was extended to enable the folding to the shape of a paper airplane. The overall area was 210 mm × 282.5 mm. The dimensions of the antenna were as described in Figure 5.1(a). Two cases were first investigated and are shown in Figurer 5.2. The first one (Figure 5.2(a)) is the planar antenna in Figure 5.1 with the paper substrate extended to about an A4 sheet. The second (Figure 5.2(b)) is the same antenna folded on the inside as part for the origami paper airplane.
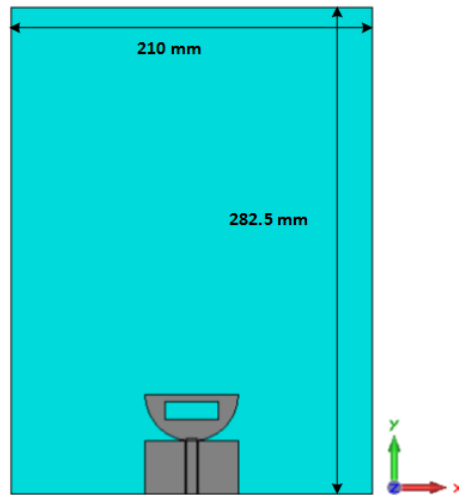
(a)
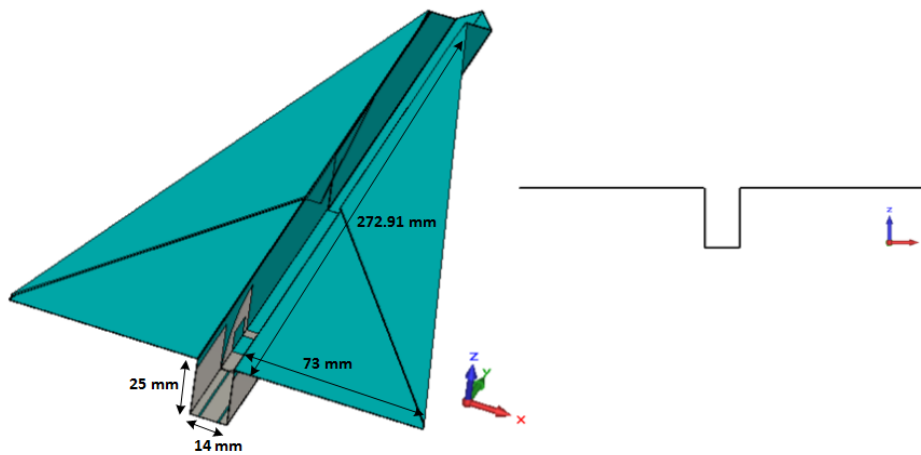
(b)

Figure 5.2 Modelling of Foldable dual band inkjet-printed CPW-fed antenna on the paper substrate: (a) extended planar (b) folded type 1 antenna

Figure 5.3 presents the reflection coefficient (S_{11}) for the three cases: the planar antenna (Figure 5.1(a)), the planar antenna with extended paper sheet (Figure 5.2(a)), and the folded antenna (Figure 5.2(b)). The overall increase in dimensions of the paper substrate had almost no influence on the antenna performance. When the antenna is folded, the resonant frequency very slightly reduced, and bandwidth also decreased. The matching of the antenna (S_{11}) improved at the lower band but degraded slightly at the higher band.
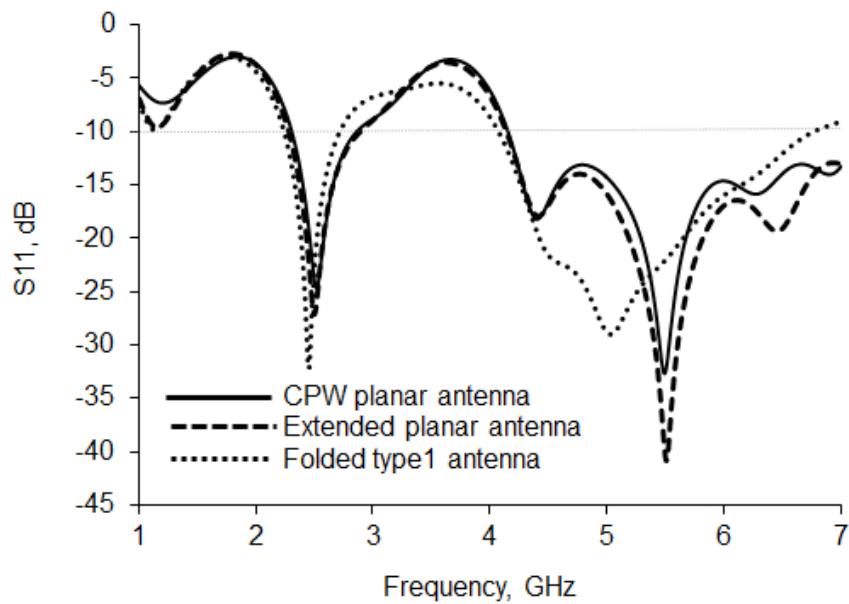
Figure 5.3 Case studies of foldable dual band inkjet-printed CPW-fed antenna on the paper substrate

5.2.2 Fabrication and Measurement

The model of the antenna was exported from CST Microwave Studio[TM] to ViewMate. It was then converted to a *.gbr file at a 1:1 scale to create a PDF file that could be ready for printing. A Brother MFC-J5910DW inkjet printer was used with AgIC-CP01A4 paper and AgIC-AN01 Silver Nano Ink [21]. The Silver Nano Ink on the special coated paper provides conductivity of about 0.2Ω/sq [21]. An MFC-J5910DW desktop inkjet printer from Brother Industries Ltd, USA was used. Conductive ink cartridges provided by AgIc Inc. replaced the normal color ink cartridges in the printer. Conductivity emerges after a few seconds when the patterns were printed on the paper sheet. Heat resistance related to thermal stability is allowed up to 30 minutes at 100 ° C. The mechanical stability of the conductive pattern was investigated by ISO 2409 bending strength [22]. The test result was 0 to 1 (with 0 is the best, 5 is the worst), indicating good mechanical stability.

Figure 5.1(b) shows the fabricated antenna on the paper substrate. The antenna was fed by a 50 ohm SMA connector which was attached using silver epoxy conductive

glue. The antenna was placed in an oven at 70°C for an hour to improve the conductivity of the glue and ink. The resistance between the furthest two ends of the antenna was found to be less than 0.5 ohm.

A very simple and traditional origami folding airplane was used for this first demonstrator. The unfolded and the initial folded antennas fabricated are shown in Figure 5.4. The measured S_{11} of the two antennas is presented in Figure 5.5. As with the simulation, the measured reflection coefficients of the folded antennas at lower frequency is worse than for the planar antennas. Nevertheless, the two designs were able to cover the 2.4 GHz and 5.2 GHz WLAN bands with an S_{11} level of at least -10dB. The simulated radiation patterns at 2.4 GHz and 5.2 GHz are shown in Figure 5.6 and 5.7 respectively. The simulated radiation patterns of the folded antennas are similar to the planar antenna except in the positive z direction. The antenna becomes more directional when folded, particularly at the higher band. The peak gain of 3.74 and 4.96 dB are obtained at 2.4 GHz and 5.2 GHz respectively.

(a)   (b)
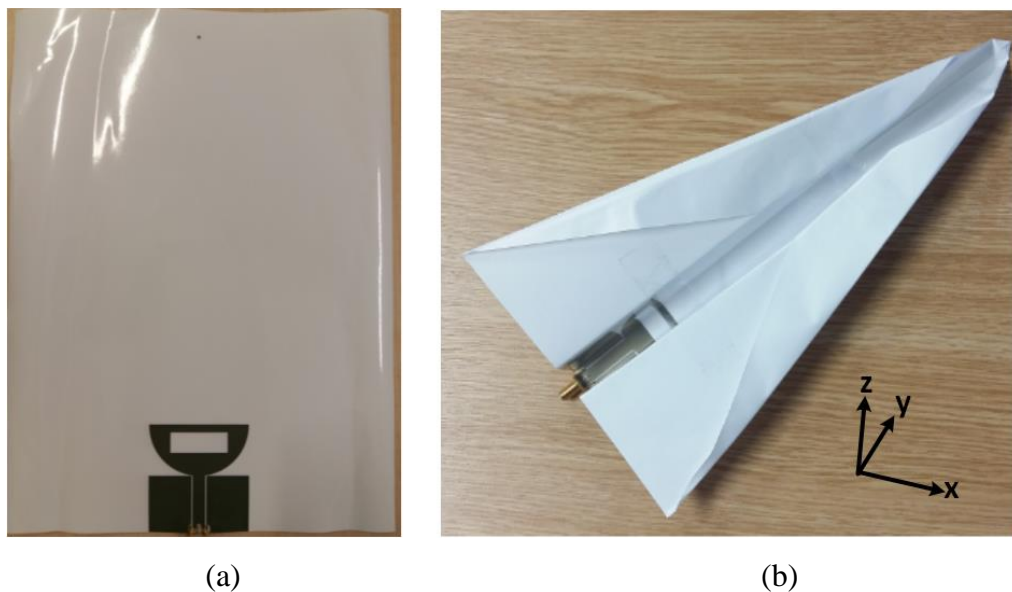
Figure 5.4 Photographs of (a) the planar antenna on the extended paper substrate, and (b) the folded type 1 antenna
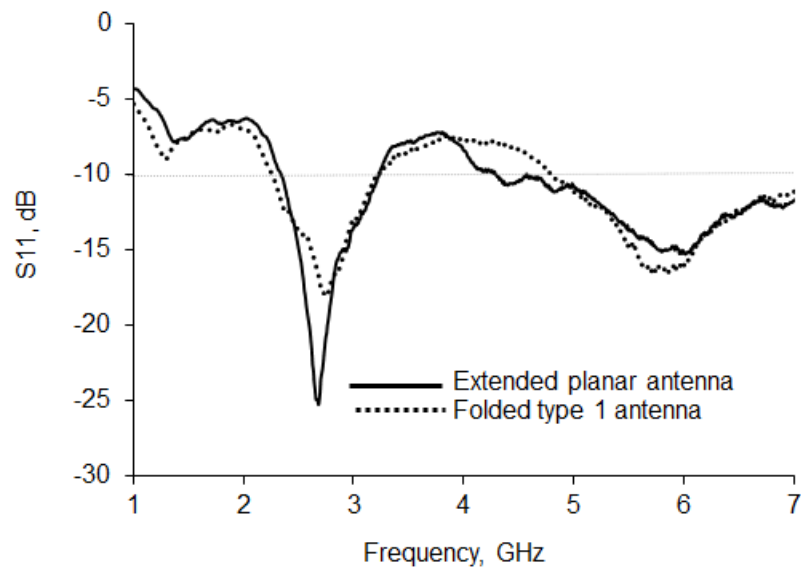
Figure 5.5 Measured S_{11} of the extended planar and foldable antennas on the paper substrate

Phi / Degree vs. dB

(a)

Theta / Degree vs. dB

(b)

Theta / Degree vs. dB

(c)
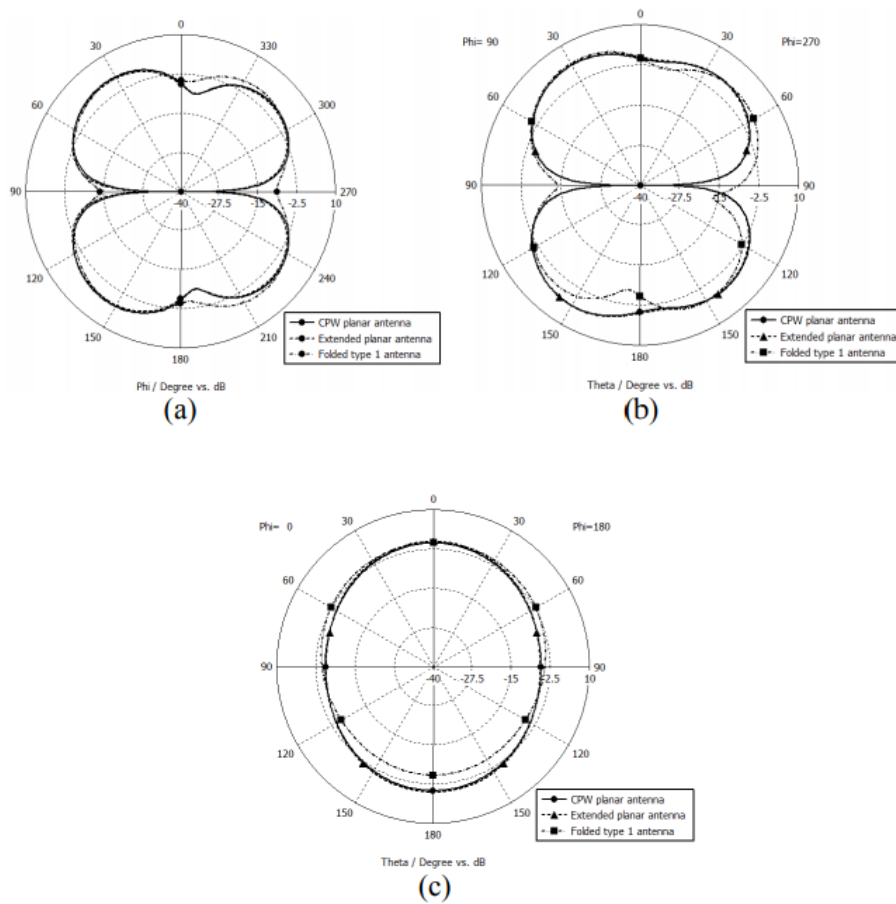
Figure 5.6 Simulated radiation patterns at 2.4 GHz (a) *xy* plane (b) *yz* plane (c) *xz* plane
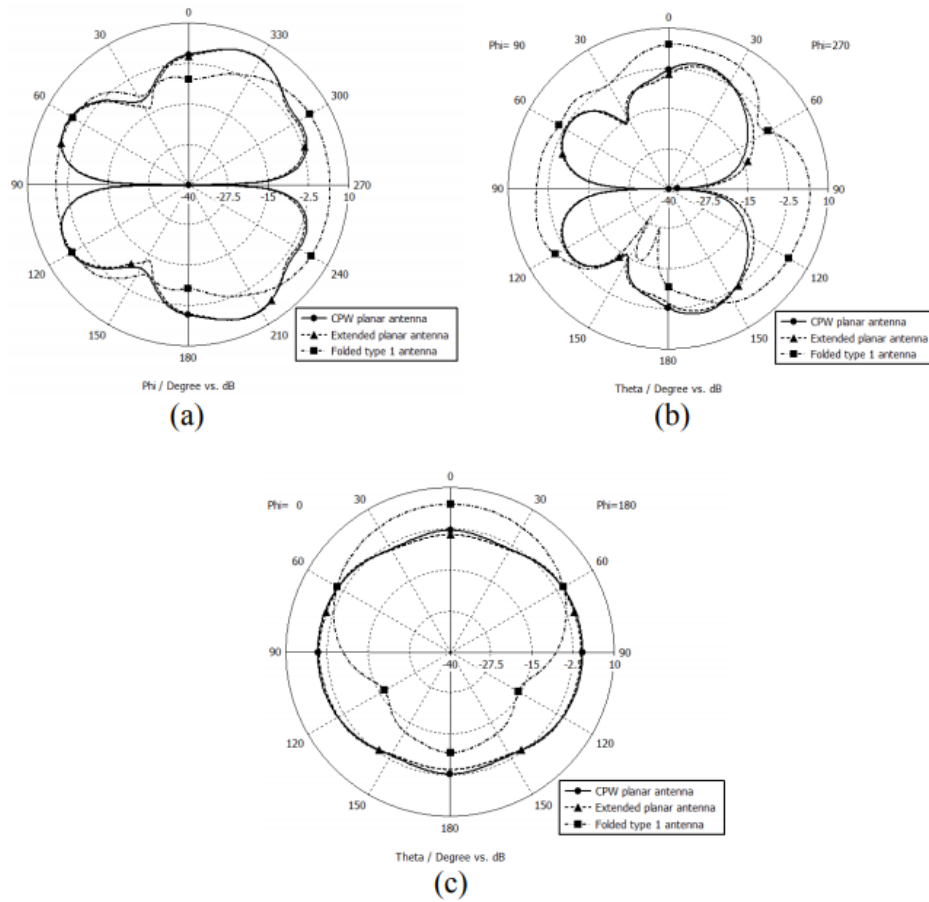
Figure 5.7 Simulated radiation patterns at 5.2 GHz (a) *xy* plane (b) *yz* plane (c) *xz* plane

5.2.3 Towards an optimised origami plane antenna design

Ideally, the antenna on the paper UAV should transmit efficiently and the radiation pattern should point towards the remote controller. The initial folded antenna design (Type 1) had a radiation pattern which pointed slightly upwards (Figure 5.6, Figure 5.7). This may not be the best solution when the controller is positioned at lower height than the airplane. This section describes a potential technique for modifying the pattern of the antenna.

Figure 5.8 shows the same antenna with a new folding technique for the origami airplane. The new folded antenna (folded type 2) gave very similar S_{11} (Figure 5.9)

to the first folding design ((Figure 5.2(b)). Figure 5.10 shows the fabrication prototype while Figure 5.11 presents the measured S_{11}. The higher band is clearly more sensitive to folding than the lower band. The new design was able to cover the desired 2.4 GHz and 5.2 GHz WLAN bands. Moreover, the radiation pattern (Figure 5.12 and 5.13) is pointing downwards which prove to be more efficient in the case of the controller being at a lower height than the UAVs.
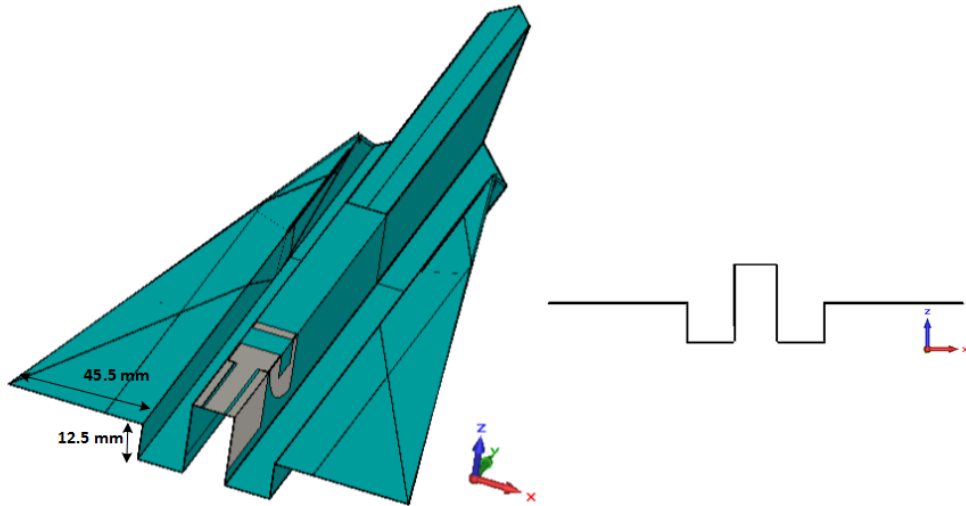
Figure 5.8 Foldable dual band inkjet-printed CPW-fed antenna on the paper substrate (Type 2)
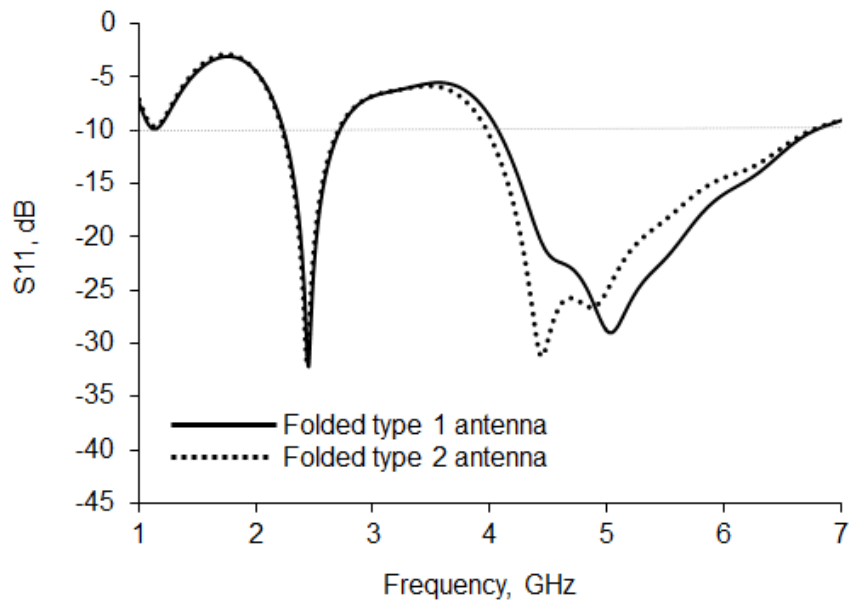
Figure 5.9 Simulated S_{11} of the foldable dual band inkjet-printed CPW-fed antennas on the paper substrate

97

Figure 5.10 Photographs of the foldable dual band inkjet-printed CPW-fed antenna
on the paper substrate (Type 2)
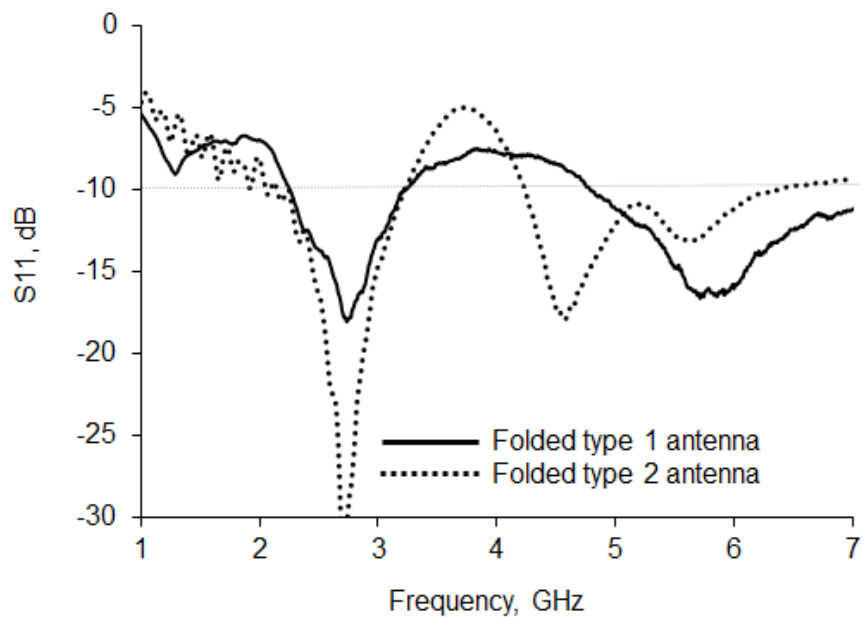
Figure 5.11 Measured S_{11} of the foldable dual band inkjet-printed CPW-fed antennas
on the paper substrate
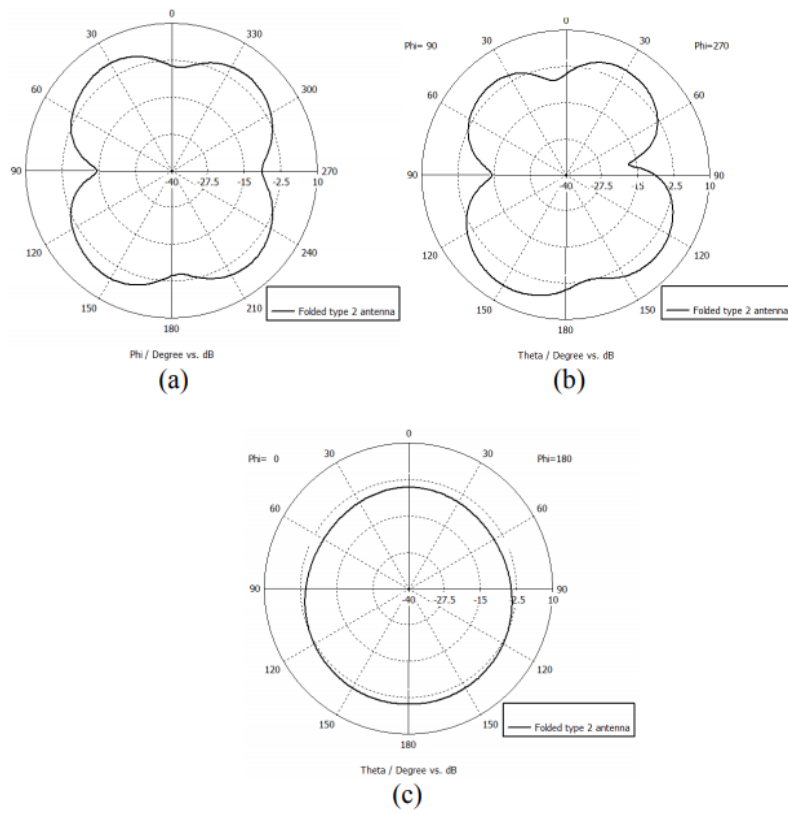
Figure 5.12 Radiation patterns at 2.4 GHz (a) *xy* plane (b) *yz* plane (c) *xz* plane
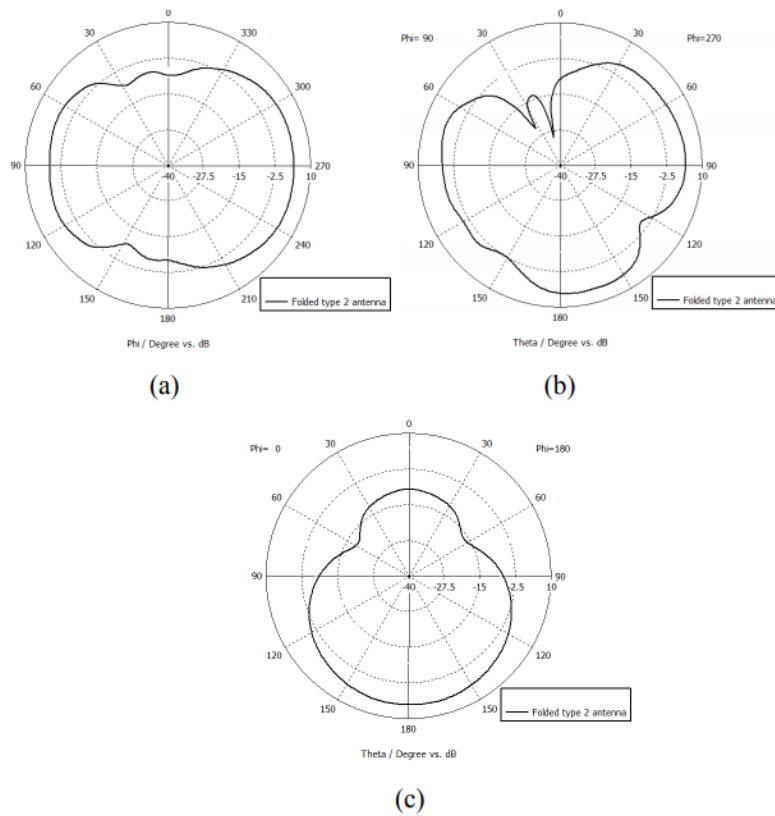
Figure 5.13 Radiation patterns at 5.2 GHz (a) *xy* plane (b) *yz* plane (c) *xz* plane

5.3 Investigation of Antennas integrated into Disposable UAVs

The performance of two antennas based on a similar design concept is assessed in Sections 5.3 and 5.4. The antennas are optimized for two conditions. The first is when all electronic components and the ground plane are located on the wings. The second is a when the electronic components are at the bottom of the drone and the antenna needs to be feed from bottom up. The latter uses a coplanar waveguide fed line which is used for the analysis of the deposited metallic layers. Inexpensive fabrication equipment, and silver nanoparticle ink has been employed for the fabrication of the antennas. The antennas are designed to cover the 2.4 GHz and 5 GHz bands currently specified in the communication of drones [23], [24]. This includes transmission of large amount of data for potential video recording applications at 5.8GHz. This is the first time that antennas are studied for integration with disposable origami drones, particularly involving inkjet printing and realistic scenarios with vertically polarized antennas. The antennas have been designed taking into account the limitations of inkjet printing technologies such as the potential damage and cracks of conducting tracks when folding the printing layers. Therefore, any folding of the antennas has been avoided.

5.4.1 Antenna design and integration with drone's electronics

One the simplest forms of disposable drone can be developed using origami techniques where a piece of paper starting as in Figure 5.14(a) can be folded to produce the drone in Figure 5.14(b). This type of drone provides the capability of the aerodynamics that can steer the wing using small elevation tabs integrated electronics [1], and an additional structure for the propelling and control [25]. The dash lines in Figure 5.14(a) indicate where the drone is folded and the corresponding dimension are given in Table 5.1. The overall size of the paper sheet is 210 mm $\times$ 290 mm which is that for an A4 sheet. As described in [26], [3], the large part of the electronics, subsystems and components for UAVs are positioned on the body and wings of the paper airplane. In Figure 5.14(b), the back of the wings has been made conductive to simulate this condition. In such case, a vertically polarized monopole is ideal with the potential locations indicated in Figure 5.15. The target frequencies of the antenna are 2.4 GHz, 5.2 GHz and 5.8 GHz wireless bands [23], [24] which

100

means a multiband antenna is desirable.
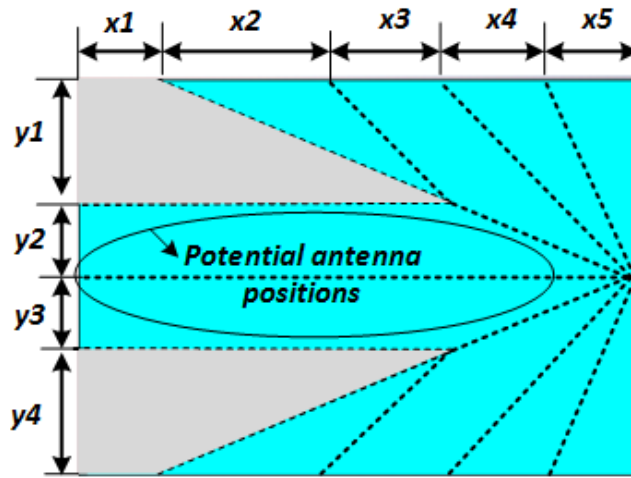
(a)
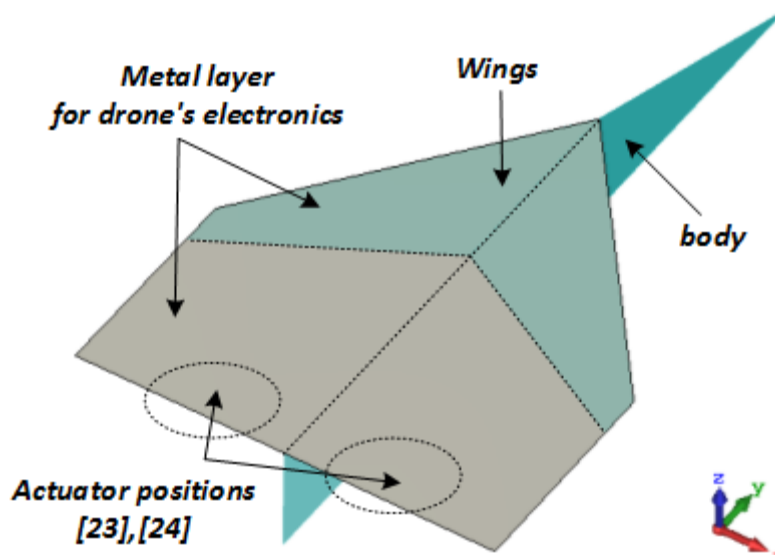
(b)

Figure 5.14 Realized paper drone geometry of (a) the unfolded planar photo paper sheet and (b) perspective view of 3D paper plane drone shape

TABLE 5.1
UNFOLDED PLANAR SHEET [mm]

x1	x2	x3	x4	x5	y1	y2	y3	y4
40	60	50	90	50	70	35	35	70

Figure 5.15 also shows the first antenna design capable of achieving this requirement. The design guideline of the antenna is provided in Figure 5.16. The antenna is based on a modified semicircle with a rectangular shape and a resonant element added at the top. The semicircle provides the large bandwidth necessary at the higher band, and the additional T-shape element is used to provide the lower band while not significantly increasing the size of the antenna. The dimensions are shown in Table 5.2. The change in operating wavelength can be expressed by a linear equation of the forms:

$$\lambda 1 = 1.8W + 0.0724 \tag{1}$$

$$\lambda 2 = 4.7L2 + 0.0048 \tag{2}$$

where W and $L2$ are the length of a resonant element and a rectangular shape and $\lambda 1$ and $\lambda 2$ are the lower and higher wavelength band respectively. The R-squared obtained is about 96% and 99% at the lower and higher wavelength band respectively. The main ground plane is positioned horizontally across the overall top surface as shown in Figure 5.14(b).
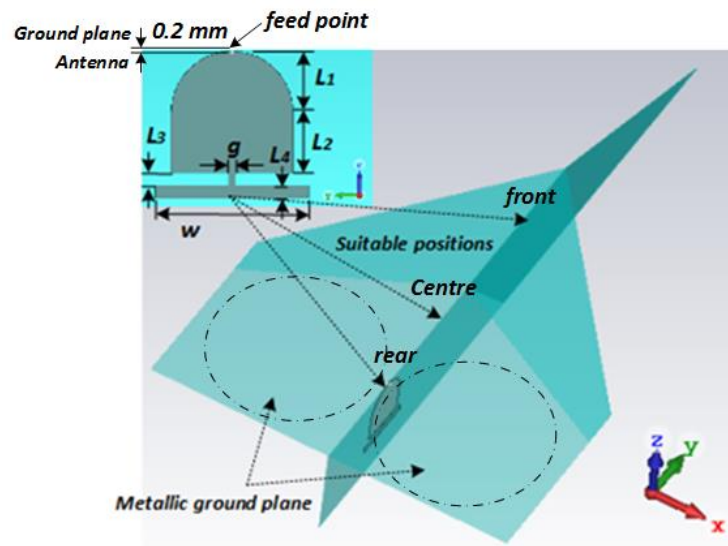
Figure 5.15 Antenna dimension of the realized origami paper drone.

102

TABLE 5.2
INITIAL ANTENNA DIMENSION WITH LARGE GROUND PLANE [mm]

L1	L2	L3	L4	g	w
9.5	9.5	2	2	1	24

Figure 5.17 show the S_{11} of the antenna when the radiating element is placed at 3 different positions: centered, at the back and at the front of the conductive ground plane. In all conditions, the antenna is able to cover the intended frequency bands for a S_{11} level less than -10dB. The depth of S_{11} and the width of the frequency band varies slightly for the three locations.
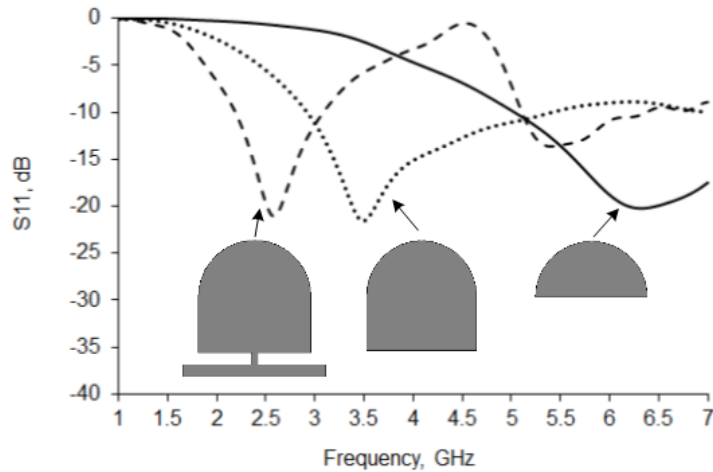
Figure 5.16 Design guideline of the antenna on S_{11}
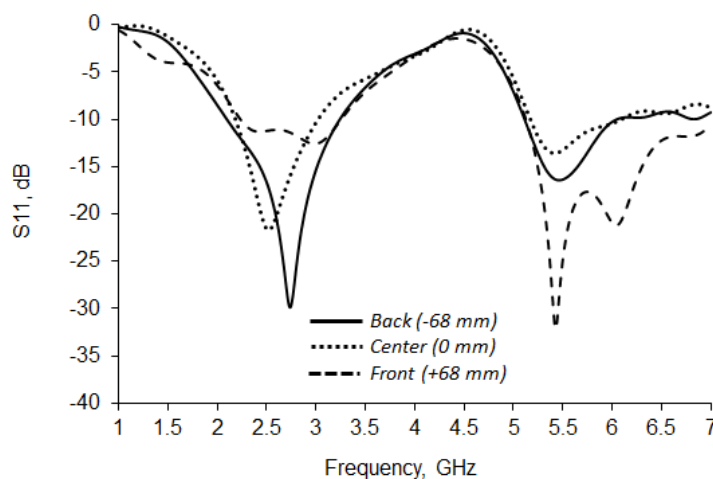
Figure 5.17 Effect of antenna location on S_{11}

5.4.2 Simplified design and effect of smaller ground

In order to simplify the fabrication process and to analyze the case where the electronics components occupy a smaller area on the wing of the plane, the metallic ground plane was reduced as shown in Figure 5.18. The antenna design is the same (Figure 5.15) but the geometry has been optimized for the smaller ground. The new dimensions are given in Table 5.3.

The reflection coefficients (S_{11}) of the two configurations of the same design are shown in Figure 5.19. At the 2.4 GHz band, the input matching of the antenna with the small ground plane is lower than that for the large ground plane. The small ground and large ground plane have the bandwidth (< -10 dB) of 280 MHz and 820 MHz respectively. By contrast, the antenna on the small ground plane offers better matching at the higher band. Nevertheless, the two models can cover the desired frequencies of 2.4 GHz, 5.2 GHz and 5.8 GHz wireless bands with an S_{11} level of less than -10dB. The bandwidth with less than -10 dB has 1670 MHz on small ground plane and 1260 MHz at large ground plane.

The surface current distributions of the antenna with small ground at three resonant frequencies (2.4 GHz, 5.2 GHz and 5.8 GHz) are depicted in Figure 5.20. At 2.4 GHz, the current flows around the overall antenna (the modified semicircle with a rectangular shape and the top resonant element) and the ground plane. By contrast, the surface current distribution concentrates around the feed of the radiating element and the bottom of the resonant element at 5.2 GHz and 5.8 GHz, as shown in Figures 5.20(b) and 5.20(c) respectively.

(a)

(b)
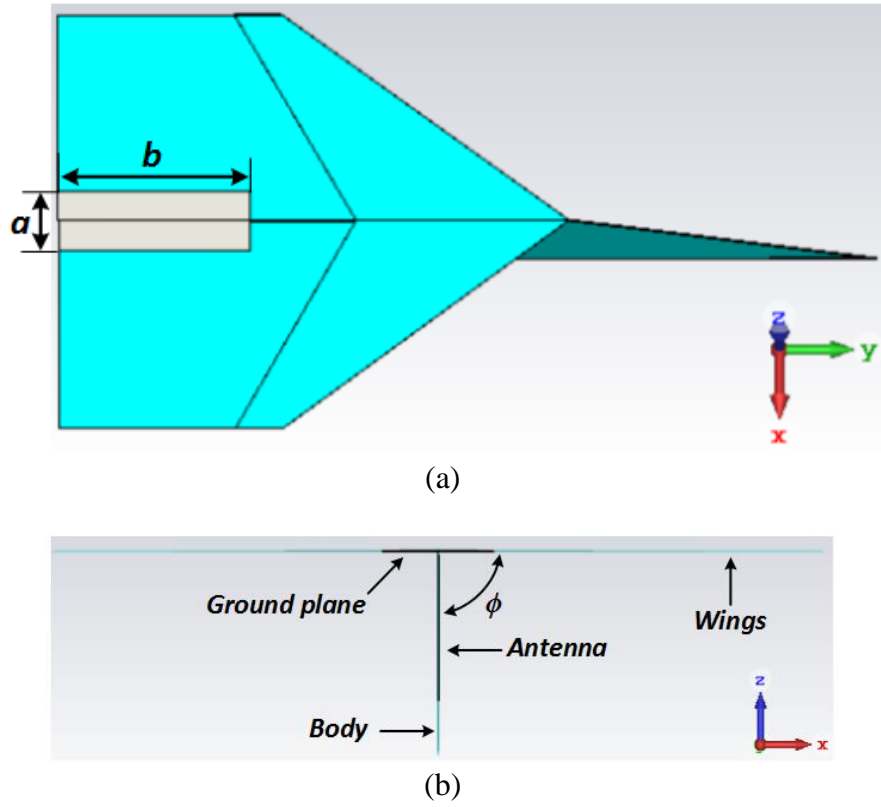
Figure 5.18 Optimized antenna with small ground plane on a realized origami paper
drone (a) top view (b) back view

TABLE 5.3

OPTIMIZES ANTENNA DIMENSION WITH SMALL GROUND PLANE [mm]

L1	L2	L3	L4	g	w	a	b
8.5	12	2	3.5	1	24	20	60
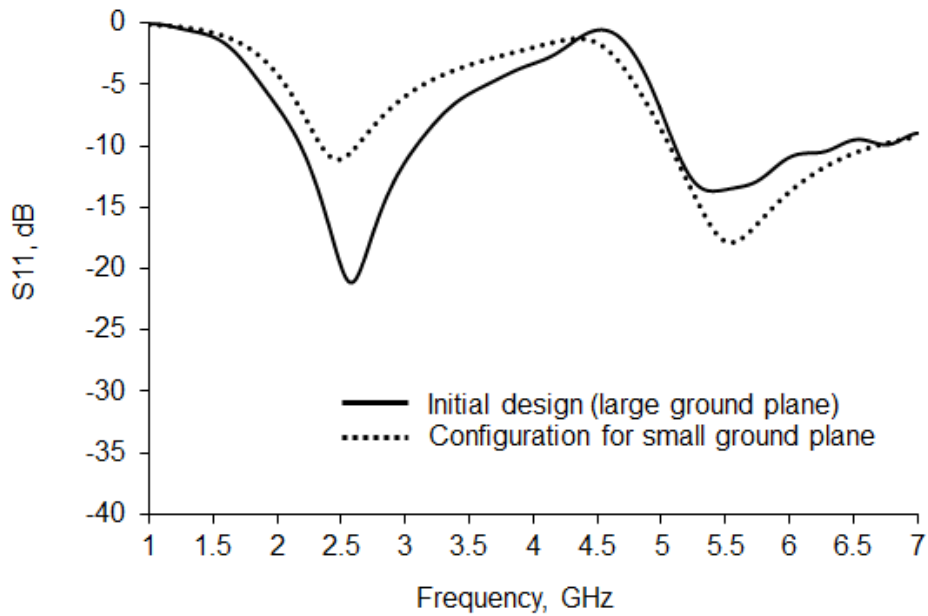
Figure 5.19 Reflection coefficient (S_{11}) of the antennas for large (Figure 5.15) and small (Figure 5.18) ground

5.4.3 Effect of Wing deformation on antenna performance

The wings of a drone are typically exposed to tensions and deformations during flight operations. This can be significant in the case of paper drones. In addition, paper drones are expected to be folded by hand and therefore the wings may not be at exactly 90° from the base after the plane has been folded. For this reason, a study of the effect of changes in the angle ϕ (Figure 5.18) on S_{11} and the radiation patterns has been carried out. Figure 5.21 presents the S_{11} of the antenna for values of ϕ of 60°, 90° and 120°. According to the different angles of the folding of the wings indicates the change of the ground plane of the antenna. The matching of the antenna changes for different angles of the folding of the wings. The frequency of operation and the input matching decrease when ϕ is decreased. The -10dB bandwidth narrows at lower band but becomes wider at higher band. Further analysis indicates that the antenna is able to cover the 2.4 GHz, 5.2 GHz and 5.8 GHz bands (S_{11} < -10dB) for angles of ϕ between 77° and 103°. The xz plane was used to analyze the effect on the radiation pattern at 2.4 GHz and 5.2 GHz as shown in Figure 5.22. All radiation patterns are very similar for the folding angle studied.
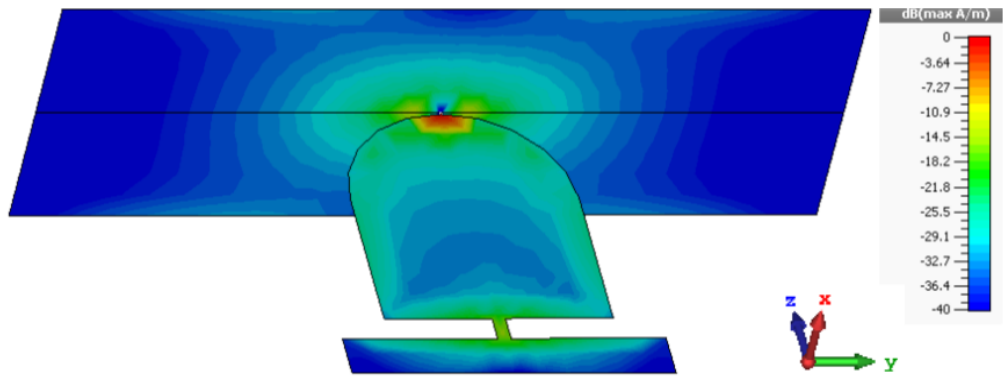
(a)
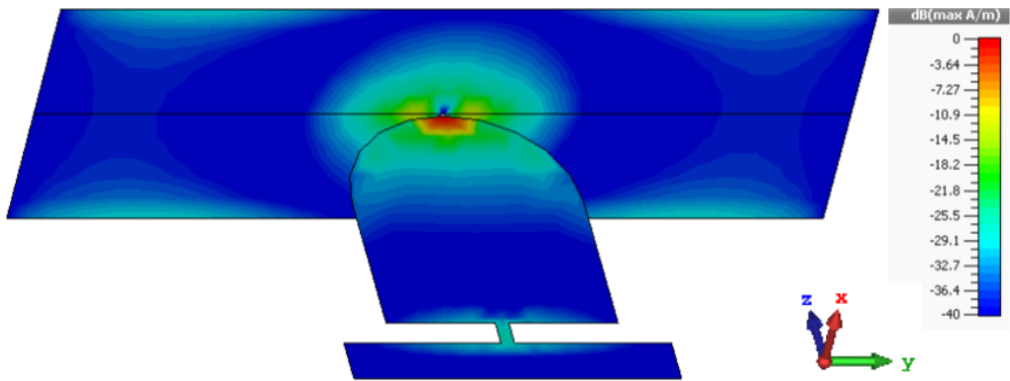
(b)
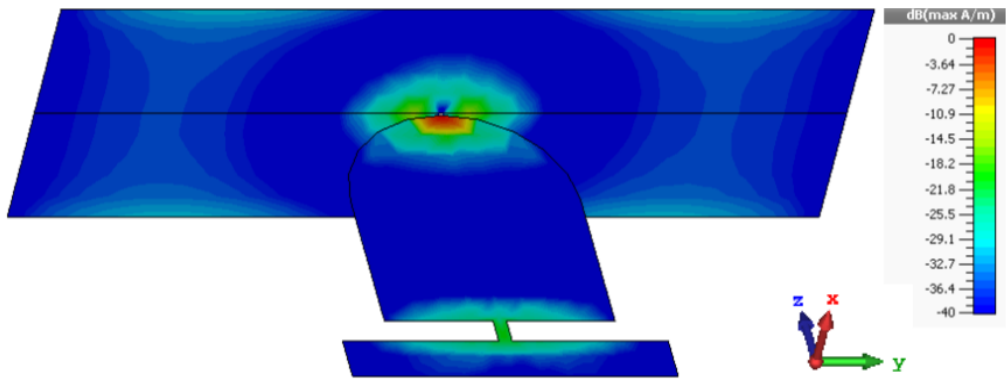
(c)

Figure 5.20 Surface currents for the antenna design in Figure 5.15

(a) 2.4 GHz, (b) 5.2GHz and (c) 5.8GHz

107
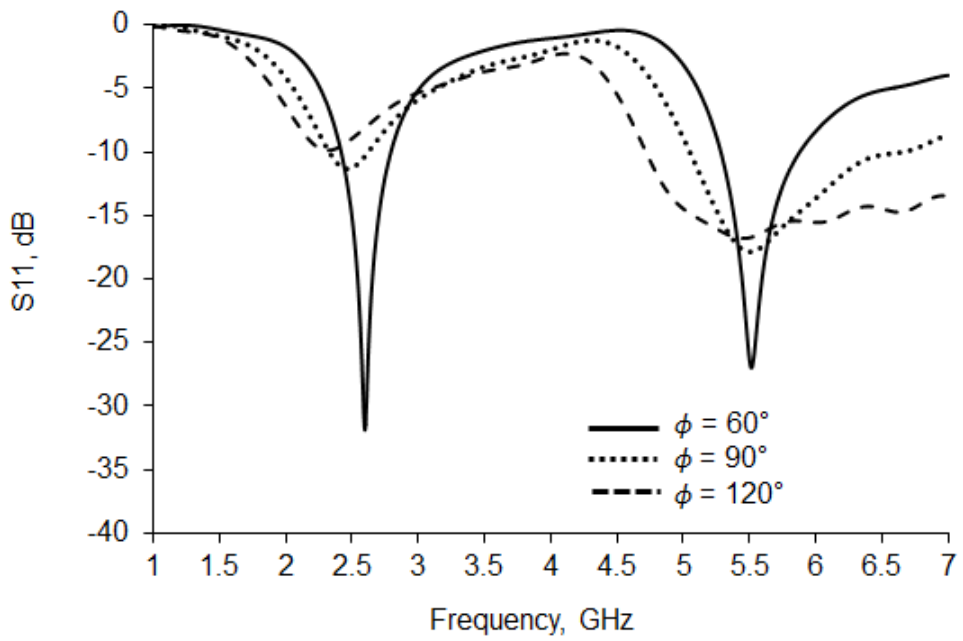
Figure 5.21 Effect of changes in angle ϕ on S_{11}

(a)   (b)
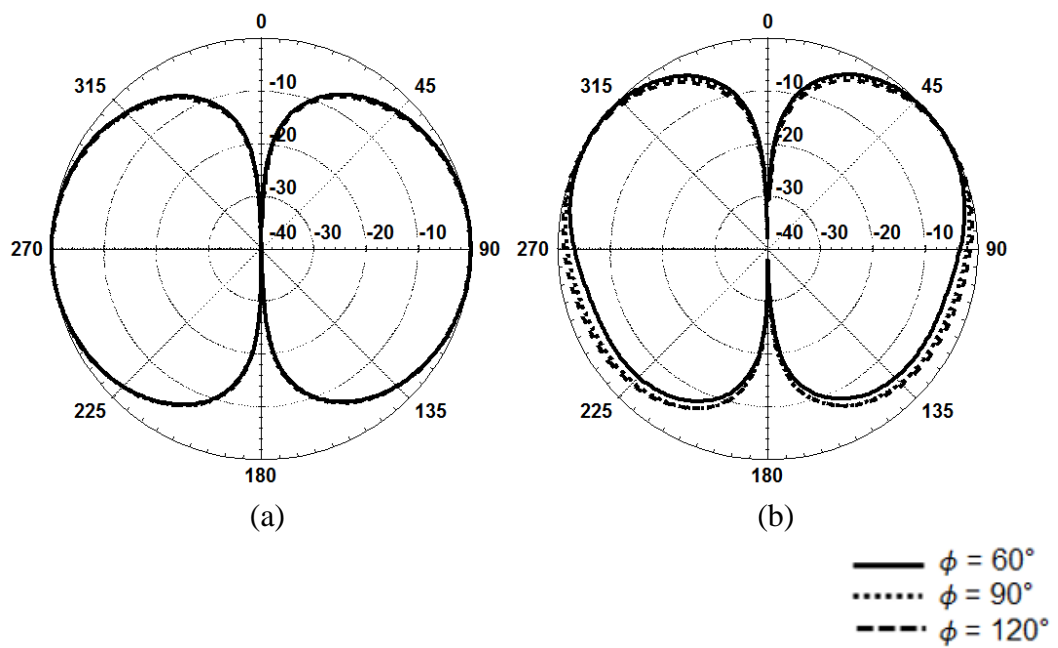
Figure 5.22 Effect of changes in angle ϕ on the *xz* plane of the radiation pattern

(a) at 2.4GHz and (b) at 5.2GHz

5.4.4 Fabrication and Measurement

For the fabrication, the 3D model with the radiation elements and the ground plane were changed to a 2D model and positioned on a planar substrate as shown in Figure 5.23(a). The 2D model with the antenna and the ground plane was exported to ViewMate from CST Microwave Studio^{TM} with Gerber file (single layer). It was then converted to a PDF file. The dimensions of the antenna and the ground plane were printed directly onto the AgIC_CP01A4 photo paper with AgIC-AN01 Silver Nano Ink [21].

A photograph of the fabricated paper plane drone is presented in Figure 5.23(b). A 50 ohm SMA connector was attached to the center of the ground plane using silver epoxy conductive glue. Similarly to the simulation model, the antenna was vertically positioned on the drone. In order to keep ϕ at 90° during the measurement, two rectangular blocks made of Styrofoam ($\varepsilon_r \approx 1$) were attached at the back sides of the wings.

Styrofoam

SMA connector

Ground
plane

Paper plane drone

silver epoxy conductive glue

(a)   (b)
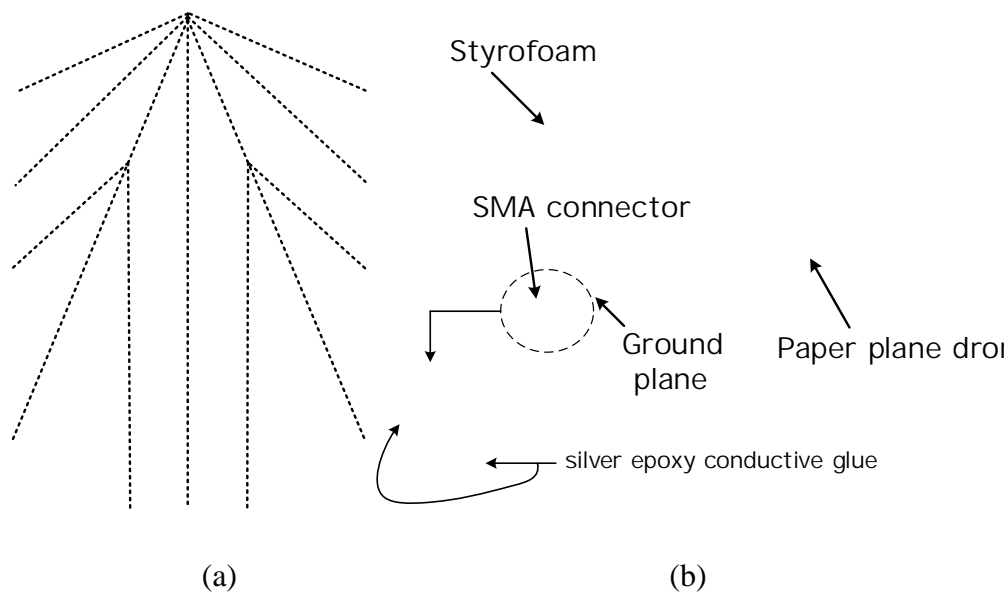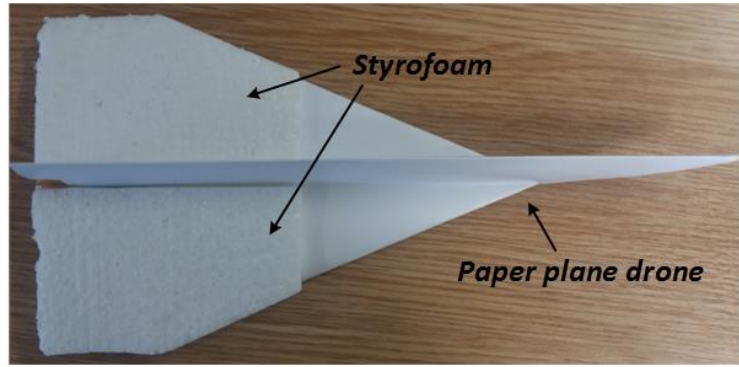
(c)

Figure 5.23 Photograph of (a) printed planar photo paper sheet (b) the origami paper drone and (c) front view of the drone

Figure 5.24 shows the reflection coefficient (S_{11}) of the optimized antenna with a small ground plane. The measured reflection coefficient was carried out using an Anritsu 37397C vector network analyzer. The measured S_{11} is about -11 dB, -17 dB and -15 dB at 2.4 GHz, 5.2 GHz and 5.8 GHz respectively with the bandwidth (<-10dB) of 400 MHz at lower band and 2200 MHz at higher bands.
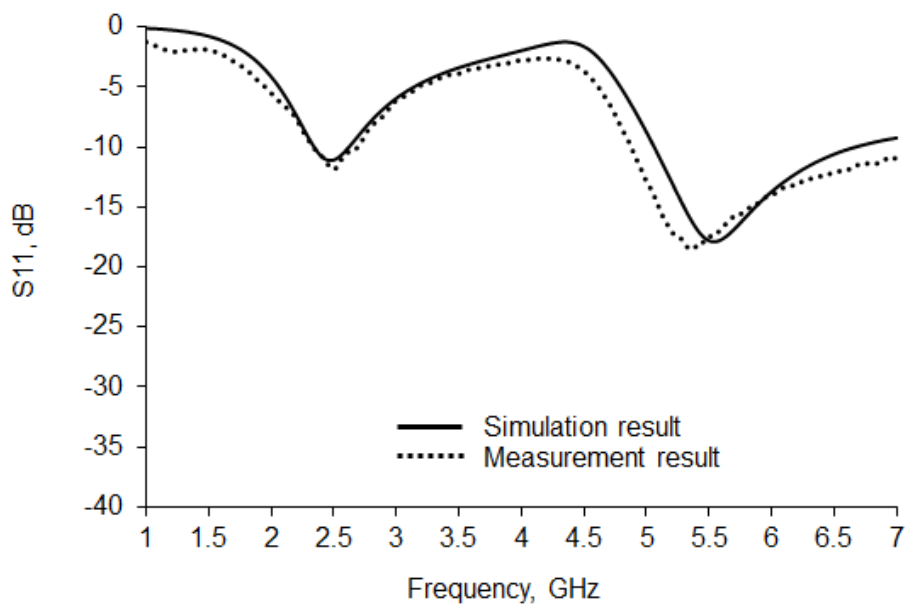
Figure 5.24 Reflection coefficient (S_{11}) of the optimized antenna with a small ground plane

The differences between the simulated and the measured results are probably due to fabrication and measurement related errors. These include the non-uniform deposited silver conductive ink of the printed antenna and ground plane, the bending of the thick photo paper substrate, and the SMA connector. Detailed fabrication issues related to the conductive layers are discussed in Section 5.4.

The measured radiation patterns at 2.4 GHz, 5.2 GHz and 5.8 GHz are shown in Figure 5.25. The patterns are dipole-like and mostly omnidirectional at the 2.4GHz band. At the 5GHz bands, the patterns become more monopole-like with mostly omnidirectional behavior in the *xy* plane but with a downward direction in the *yz* plane.

(a)

(b)

— — — ·	Meas Co-pol
·············	Meas Cro-pol
———	Sim Co-pol
— · — · —	Sim Cro-pol
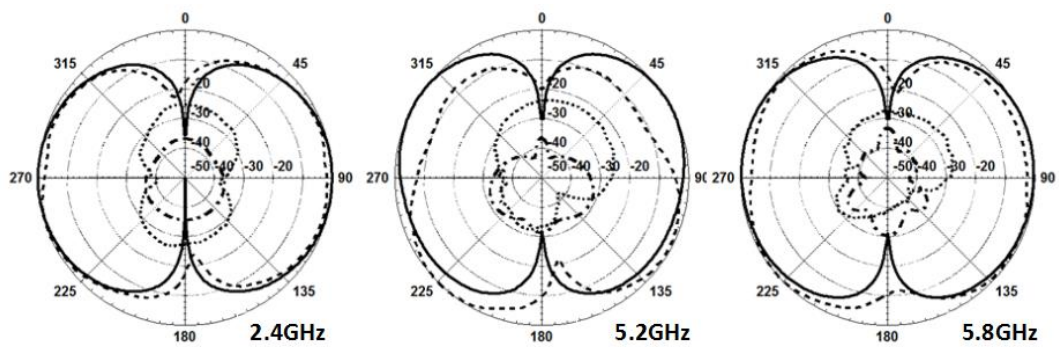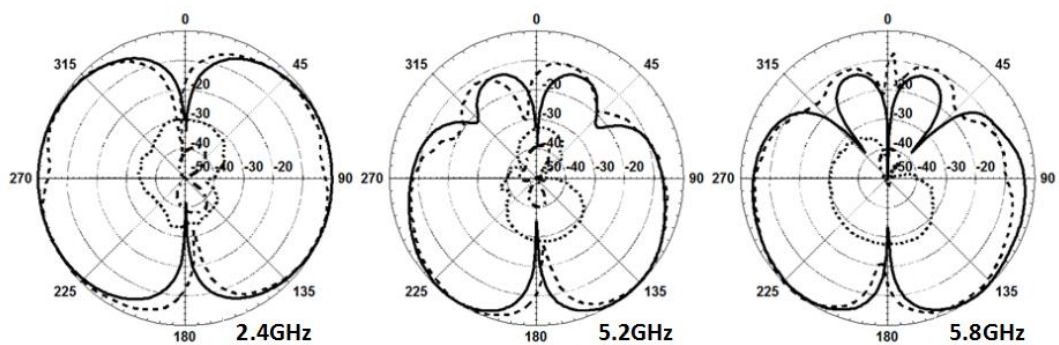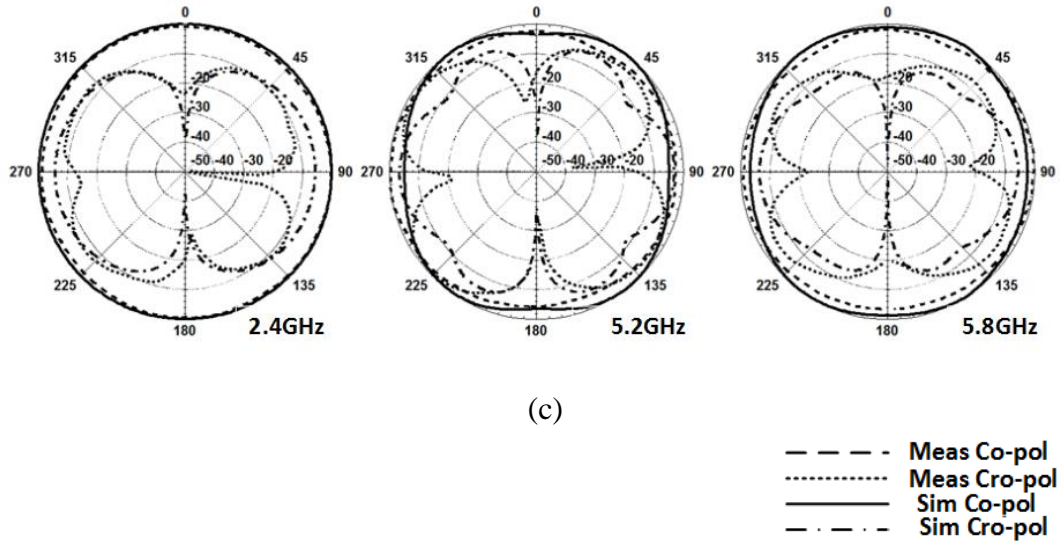
Figure 5.25 Radiation patterns of the antenna on small ground plane (a) at *xz* plane (b) at *yz* plane and (c) at *xy* plane

The measured gains calculated by gain substitution method are 2.6 dB, 7.9 dB and 6.9 dB at 2.4 GHz, 5.2 GHz and 5.8 GHz respectively. The downward direction at the higher frequency band may be useful in the cases were the controller of the drone is positioned below the antenna. However, this could reduce the range of the control or potential data transmission when flying at positions where the controller is at the same height or higher than the drone. As indicated earlier, this first antenna configuration is ideal for situations when most of the electronic components are located on the wing section of the drone which limits the possibility for improving the radiation patterns at the higher frequency band.

5.4 Second Antenna Solution and Analysis of the Printed Conductive Layers

5.4.1 Antenna design

This section proposes a vertically polarized antenna where the antenna connection is at the base of the paper drone. This antenna is also used to assess the metallic ink layers deposited in the fabrication process. Figure 5.26 shows the antenna design and

its placement within the drone. The antenna is small enough to be hidden inside the vertical section of the plane and isolated from the external environment that could damage the inkjet printed metallic tracks [25]. The radiator consists of a semicircle with an additional rectangular resonant element separated by a gap and connected by a small rectangular track. The radiating component is fed by a coplanar waveguide transmission line. The dielectric constant, tangent loss and thickness of the substrate are the same as the earlier design. The desired resonant frequency and bandwidth were obtained by adjusting the size and the length of the radiation elements and the gap between feed line and the ground plane surfaces. The dimensions of the ground plane were crucial for the optimization for the radiation pattern. The final dimensions of the antenna are given in Table 5.4.

The surface current distribution at 2.4 GHz, 5.2 GHz and 5.8 GHz are shown in Figure 5.27. At 2.4 GHz, the surface current is strong and evenly distributed through the feed line, the semicircle and the top resonant element while it is small in the middle sections of the ground plane. At 5.2 GHz, the currents are spread more uniformly in the ground plane and towards the edges of the radiator. At 5.8 GHz, the currents tend to concentrate more towards the center of the antenna and the gap between the radiator and the ground plane.
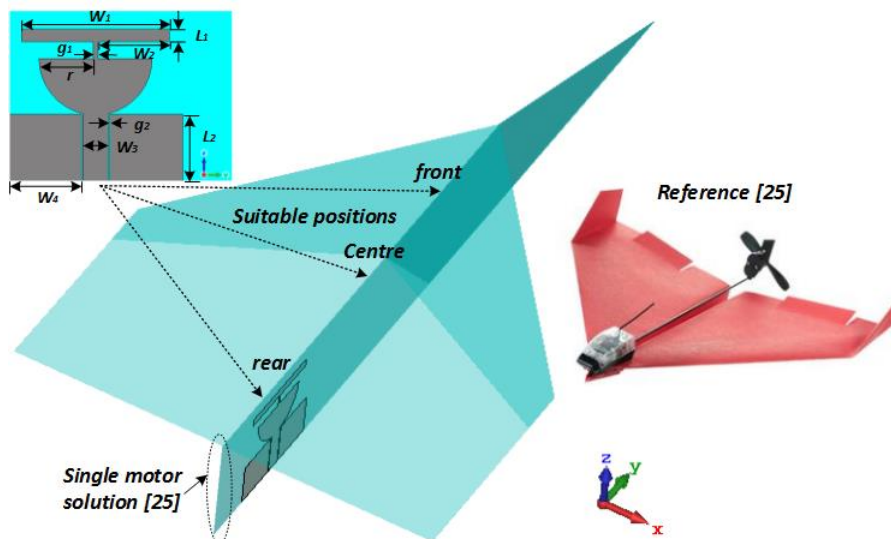
Figure 5.26 Configuration of the realized optimized paper plane drone

TABLE 5.4

OPTIMIZED ANTENNA DIMENSION [mm]

L1	L2	W1	W2	W3	W4	g1	g2	r
2.5	13	30	14	5.2	14	1	0.2	11

(a)   (b)

(c)
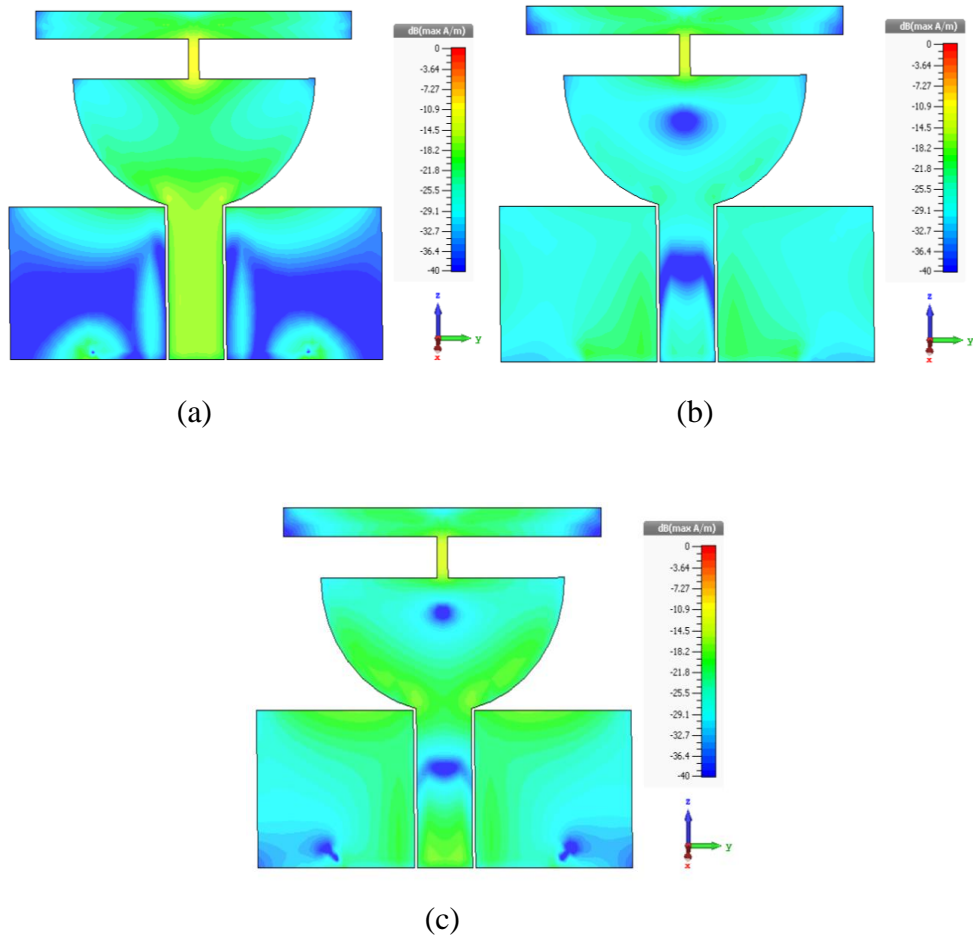
Figure 5.27 Surface currents for the antenna design in Fig. 4.23. (a) 2.4 GHz,
(b) 5.2 GHz and (c) 5.8GHz

5.5.2 Fabrication and Measurement

The antenna was realized using the same fabrication procedure described in Section
5.4.4. The procedure is relatively low cost and suitable for disposable origami paper
drones. A study of the printed layers and, in particular, in the gaps of the

transmission line should provide a further insight of the fabrication process and its potential limitations. Figure 5.28 provides a photograph showing the conductive layers in a sample taken of the CPW transmission line of the antenna. As can be seen, there are a many traces of silver ink in the channel and the edges of the tracks are non-uniform. A surface profile measured using the Veeco Dektak Stylus Profiler is shown in Figure 5.29. The green area is the top of the silver surface, the red area is the bottom of the channel. The measured height difference is 825.69 nm. The additional texture to the right is likely to be caused by variation in the substrate surface and the stray silver particles.
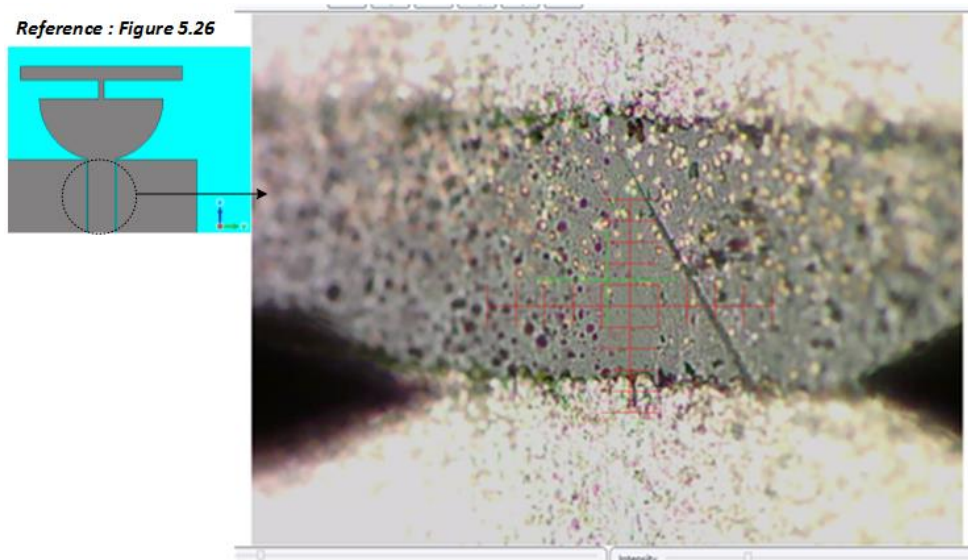
Figure 5.28 Photograph of the printed metallic layers in the CPW transmission line
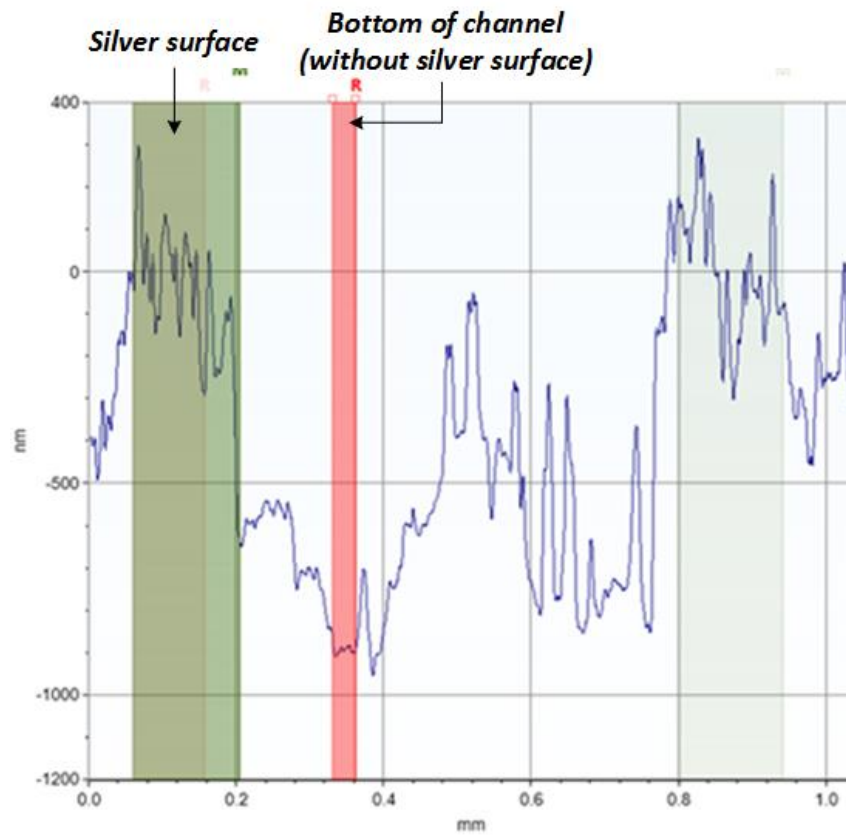
Figure 5.29 Surface profile in the CPW transmission line

Figure 5.30 presents photographs of the printed antenna on the planar paper substrate and the folded origami drone. The folding lines are included in Figure 5.30(a). The new antenna position on the paper substrate was calculated considering the sections where the drone needed to be folded. The same origami airplane and folding method as for the previous design were used.

The antenna was designed so that it fit between the necessary fold lines, thus avoiding a potential cracks in the conductive layers. A 50 ohm SMA connector was attached to the bottom of the body of the drone. Styrofoam blocks ($\varepsilon_r \approx 1$) were placed on the left and right sides of the drone to hold the paper drone in shape while carrying out the measurements.

(a)   (b)
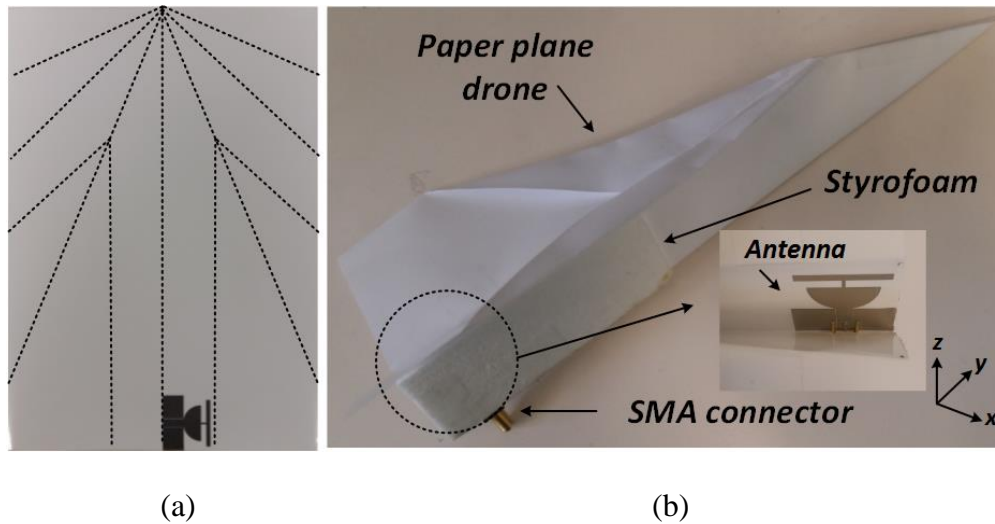
Figure 5.30 Photograph of (a) printed planar photo sheet, and (b) the folded origami
paper plane drone

The simulated and measured S_{11} are shown in Figure 5.31. The measured resonant
frequencies shifted slightly to the right. The measured first mode resonates at about
2.61 GHz with -10 dB impedance bandwidth of 23.5%. The second resonance can be
found at approximately 5.57 GHz with -10 dB bandwidth of 25.36%. The
discrepancy between simulation and measurement are probably due to the fabrication
issues discussed earlier as well as possible measurement errors. Table 5.5 gives the
comparison of resonant frequency, gain, bandwidth, and size between the proposed
antenna and the other previous antenna. From the comparison, it can be seen that the
proposed antenna presents a relatively small size at corresponding frequency bands.
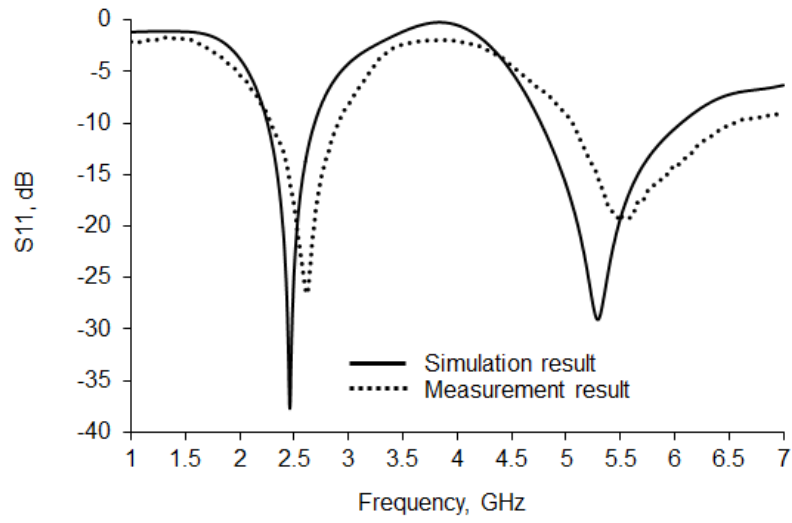
Figure 5.31 Reflection coefficient (S_{11}) of the antenna for the optimized origami paper plane drone

TABLE 5.5

Comparison between the proposed antenna and other previous antennas

Ref.	Freq. (GHz)	Gain (dB)	Bandwidth (GHz)	Size (mm^2)
[27]	2.45	1.3	0.1	50 x 50
	5.5	4.8	1	
[28]	2.4	1.3	0.5	50 x 75
	5.2	5. 15	0.2	
[29]	2.45	2.75	0.08	37.45 x 13
	5.8	5. 54	0.67	
This work	2.4	1.4	0.6	35.4 x 30.8
	5.2	7.7	1.5	
	5.8	6.2		

118

Figure 5.32 shows the radiation pattern measurement set up. Figure 5.33 shows a comparison between simulated and measured radiation patterns at 2.4 GHz, 5.2 GHz and 5.8 GHz respectively. The patterns in the *xz* plane are similar to the ones in *yz* plane with nulls along the *z*-axis. The patterns in the *xy* plane are mostly omnidirectional. The gain was 1.4 dB at 2.4 GHz, 7.7 dB at 5.2 GHz and 6.2 dB at 5.8 GHz. The measured radiation patterns were slightly distorted due to the coaxial cable.
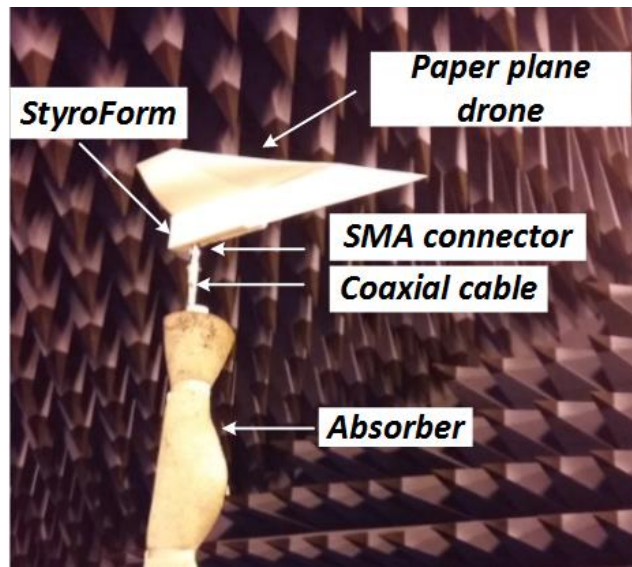
Figure 5.32 Measurement setup for the origami paper drone antenna in anechoic chamber
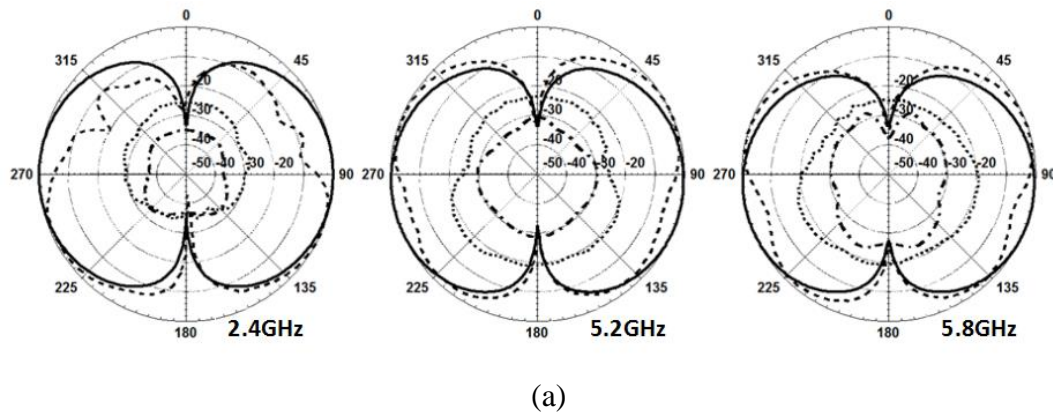
(a)
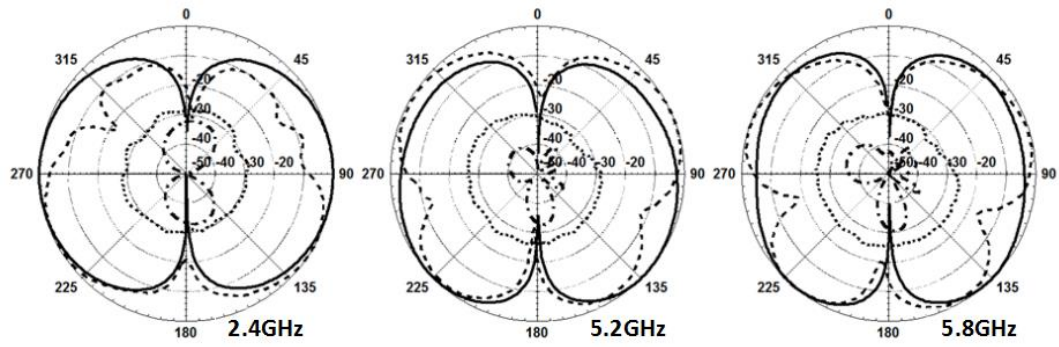
(b)
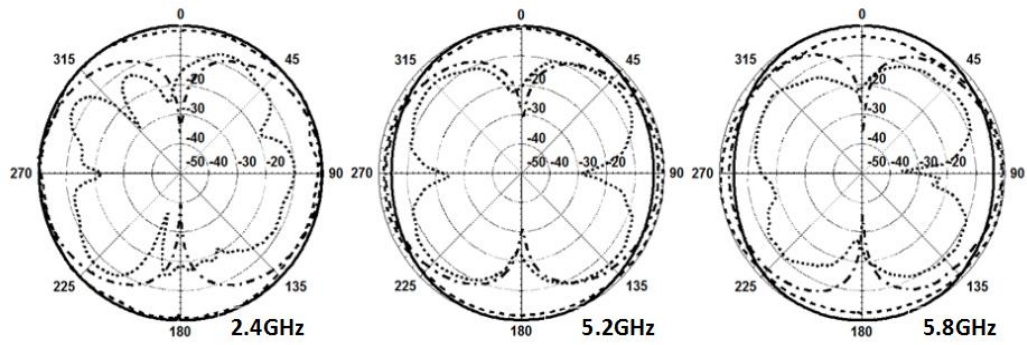
(c)

— — — - Meas Co-pol
·············· Meas Cro-pol
———————— Sim Co-pol
— · — · — Sim Cro-pol

Figure 5.33 Radiation patterns patterns (a) at *xz* plane (b) at *yz* plane (c) at *xy* plane

5.5 Conclusion

Antennas suitable for integration with low cost inkjet printing electronics on disposable paper drones have been demonstrated. The paper-based antenna has acceptable performance in planar and folding conditions. The folding should be very smooth as there is a potential for cracking the silver conductive traces. Folding the antenna increases its directivity. This may steer the beam towards an unwanted direction. By changing the folding technique and the design of the airplane, it is possible to optimize the direction of the radiation pattern.

The best antenna solution for drone communication tends to be when the antenna is vertically polarized and omnidirectional. Different antenna positions are possible when considering paper drones. One possible scenario is when the electronics are located on the wings. In this case, an antenna can be located facing downwards and using the wings as a ground plane. A second case is when the electronics are in the lower section of the plane, in which case a CPW fed antenna can be hidden inside the plane. A CPW fed antenna can also be considered a more general solution as it can be rotated as required by the other electrical components of the drone.

A commercial desktop inkjet printer with silver nanoparticle conductive ink cartridges can be used for the antenna fabrication. It has been proven to be an inexpensive and fast method with sufficient printed quality for this application. The fabricated antennas have acceptable performance for efficient communication between the plane and a remote controller.

As a low cost fabrication procedure, inkjet printing with off the shelf printers, with cartridges containing silver conductive ink may produce tracks with discontinuity at the edges and also unwanted deposition of inks across any channel. However, these fabrication errors do not seem to significantly affect the performance of the antennas at the frequency of operation of commercial drones.

In the future, disposable origami drones may include other electronic components which are also inkjet printed along the antenna. This will create a fully integrated disposable drone solution. There is enough evidence from ongoing work by various research groups [18], [21] – [25] to support this vision. This paper has now contributed to this new field from the antenna perspective.

References

[1] P. Pounds, "Paper plane: Towards disposable low-cost folded cellulose-substrate UAVs," in Australasian Conference on Robotics and Automation, 2012.

[2] Evan Ackerman, "Swarms of Disposable Drones Will Make Critical Deliveries and Then Vanish." IEEE Spectrum. Web. 1 Feb 2017. [online]:

Available:http://spectrum.ieee.org/automaton/robotics/drones/otherlab-apsara-aerial-delivery-system (Accessed August. 2017).

[3] G. Grau, E. J. Frazier, and V. Subramanian, "Printed unmanned aerial vehicles using paper-based electroactive polymer actuators and organic ion gel transistors," Microsyst. Nanoeng., vol. 2, p. 16032, 2016.

[4] J. Berni, P. Zarco-Tejada, L. Suarez and E. Fereres, "Thermal and Narrowband Multispectral Remote Sensing for Vegetation Monitoring From an Unmanned Aerial Vehicle", IEEE Trans. Geosci. Remote Sens., vol. 47, no. 3, pp. 722-738, 2009.

[5] Y. Nijsure, G. Kaddoum, N. Khaddaj Mallat, G. Gagnon and F. Gagnon, "Cognitive Chaotic UWB-MIMO Detect-Avoid Radar for Autonomous UAV Navigation", IEEE Trans. Intell. Transp. Syst., vol. 17, no. 11, pp. 3121-3131, 2016.

[6] H. Menouar, I. Guvenc, K. Akkaya, A. Uluagac, A. Kadri and A. Tuncer, "UAV-Enabled Intelligent Transportation Systems for the Smart City: Applications and Challenges", IEEE Commun. Mag., vol. 55, no. 3, pp. 22-28, 2017.

[7] M. A. Goodrich et al., "Supporting wilderness search and rescue using a camera-equipped mini UAV", J. Field Robot., vol. 25, no. 1, pp. 89-110, Jan./Feb. 2008.

[8] H. Zhou, H. Kong, L. Wei, D. Creighton and S. Nahavandi, "Efficient Road Detection and Tracking for Unmanned Aerial Vehicle", IEEE Trans. Intell. Transp. Syst., vol. 16, no. 1, pp. 297-309, 2015.

[9] Guowei Cai, B. Chen, Kemao Peng, Miaobo Dong and T. Lee, "Modeling and Control of the Yaw Channel of a UAV Helicopter", IEEE Trans. Ind. Electron., vol. 55, no. 9, pp. 3426-3434, 2008.

[10] L. Gupta, R. Jain and G. Vaszkun, "Survey of Important Issues in UAV Communication Networks", IEEE Commun. Surveys Tuts., vol. 18, no. 2, pp. 1123-1152, 2016.

[11] S. Hayat, E. Yanmaz and R. Muzaffar, "Survey on Unmanned Aerial Vehicle Networks for Civil Applications: A Communications Viewpoint", IEEE Commun. Surveys Tuts., vol. 18, no. 4, pp. 2624-2661, 2016.

[12] G. Virone, A. Lingua, M. Piras, A. Cina, F. Perini, J. Monari, F. Paonessa, O. Peverini, G. Addamo and R. Tascone, "Antenna Pattern Verification System

Based on a Micro Unmanned Aerial Vehicle (UAV)", IEEE Antennas Wireless Propag. Lett., vol. 13, pp. 169-172, 2014.

[13]   F. Namin, J. Petko and D. Werner, "Analysis and Design Optimization of Robust Aperiodic Micro-UAV Swarm-Based Antenna Arrays", IEEE Trans. Antennas Propag., vol. 60, no. 5, pp. 2295-2308, 2012.

[14]   N. Neveu, Y. Hong, J. Lee, J. Park, G. Abo, W. Lee and D. Gillespie, "Miniature Hexaferrite Axial-Mode Helical Antenna for Unmanned Aerial Vehicle Applications", IEEE Trans. Magn., vol. 49, no. 7, pp. 4265-4268, 2013.

[15]   A. Barka, "Integration of antennas onboard vehicles and diffraction by large and complex structures with multiple-domain–multiple-methods techniques," Proc. IEEE, vol. 101, no. 2, pp. 280–297, Jan. 2013.

[16]   Q. Liu et al., "A novel broad beamwidth conformal antenna on unmanned aerial vehicle," IEEE Antennas Wireless Propag. Lett., vol. 11, pp. 196–199, 2012.

[17]   B.-H. Sun, Y.-F. Wei, S.-G. Zhou, and Q.-Z. Liu, "Low-profile and horizontally-polarised antenna for UAV applications," Electron. Lett., vol. 45, no. 22, pp. 1106–1107, Oct. 2009.

[18]   D. Kang, J. Tak and J. Choi, "Wideband low-profile planar square segmented loop antenna for UAV applications", Electron. Lett., vol. 52, no. 22, pp. 1828-1830, 2016.

[19]   L. Scorrano, A. Di Rosa, B. Orobello, A. Manna and F. Trotta, "Experimental Investigations of a Novel Lightweight Blade Antenna for UAV Applications [Antenna Applications Corner]", IEEE Antennas and Propag. Magazine, vol. 59, no. 2, pp. 108-178, 2017.

[20]   G. Shaker, S. Safavi-Naeini, N. Sangary, and M. Tentzeris, "Inkjet printing of ultrawideband (UWB) antennas on paper-based substrates," IEEE Antennas Wireless Propag. Lett., vol. 10, pp. 111–114, 2011.

[21]   AgIC Inc., [online]: Available: https://agic.cc/en/ (Accessed August. 2017).

[22]   The International Organization for Standardization, [online]: Available: https://www.iso.org (Accessed December. 2017).

[23]   J. Chen, K.-F. Tong, and J. Wang, "A triple band arc-shaped slot patch antenna for UAV GPS/Wi-Fi applications," in Proc. Int. Symp. Antennas Propag. (ISAP), vol. 1, pp. 367–370, 2013.

[24]   J. Romeu, A. Aguasca, J. Alonso, S. Blanch and R. R. Martins, "Small UAV radiocommunication channel characterization," in Proc. 4th EuCAP, Apr. 2010.

[25]   PowerUp, [online]: Available: https://www.poweruptoys.com/ (Accessed August. 2017).

[26]   P. Pounds and S. Singh, "Integrated electro-aeromechanical structures for low-cost, self-deploying environment sensors and disposable UAVs," in Proc. IEEE/RAS Int. Conf. Robotics Automation, pp. 4459– 4466, 2013.

[27]   Y. Lu and Y. Lin, "A mode based design method for dual-band and self-diplexing antennas using double T-stubs loaded aperture," IEEE Trans. Antennas Propag., vol. 60, no. 12, pp. 5596–5603, Dec. 2012.

[28]   Y.-L. Kuo and K.-L. Wong, "Printed double-T monopole antenna for 2.4/5.2 GHz dual-band WLAN operations," IEEE Trans. Antennas Propag., vol. 51, pp. 2187-2192, 2003.

[29]   I.-F. Chen and C.-M. Peng, "Microstrip-fed dual-U-shaped printed monopole antenna for dual-band wireless communication applications," Electron Lett., vol. 39, pp. 955-956, 2003.

CHAPTER 6.

3D AND INKJET PRINTED CIRCULAR POLARISED ANTENNA

6.1 Introduction

This chapter describes the use of additive manufacturing (AM) equipment for the development of circularly polarised (CP) antennas. Two AM processes are combined for the fabrication of a CP patch antenna: stereolithography (SLA) and inkjet printing of silver conductive inks. As CP patch antennas are created by slightly modifying the shapes of the radiators, they are particularly suitable for the assessment of the fabrication process. A widely available SLA printer is first employed for the layer-by-layer fabrication of the substrate. Subsequently, inkjet printing is used to deposit the metallic layers of the radiating element on the substrate. The two printing machines are very low-cost in comparison to those used in previously reported work. Good adhesion of the metallic patterns to the substrate is observed. Furthermore, reasonably low resistance is achieved on the metallic surfaces. The aim of this chapter is to demonstrate the use of alternative, inexpensive machines, for the prototyping and manufacturing of antennas. In this work, the antenna operates at the 1575MHz GPS frequency band for the application of the satellite communication.

Metal etching and subtractive processes are the most common methods employed for the fabrication of antennas and microwave devices. Recently, there has been an increasing research interest in applying AM [1]-[7] for electronic device prototyping and fabrication. AM offers design freedom, customisation, and potential cost reduction for low volume production processes. Several microwave structures have been reported, including frequency selective surfaces (FSS) [1], electromagnetic band gap structures (EBG) [2], waveguide components [3] and antennas [4]. A variety of technologies and materials are available for the layer by layer fabrication

of dielectric and metals. Two of the most accessible and lowest cost techniques for the printing of dielectrics are fuse deposition modelling (FDM) and stereolithography (SLA). EM structures have been fabricated by adding metallic layers over FDM substrates [2], [5]. In [2], the metallic layer was added by hand, while in [5] a dispenser was used to add layers of silver conductive paste. One of the problems of FDM substrates is the roughness of the external surfaces which limits the metallic layers to thicker, paste based metallic materials. SLA substrates, on the other hand, provide smoother surfaces which can be an advantage when fabricating with other metallic layer deposition processes such as inkjet printing. Inkjet printing has been demonstrated for the fabrication of antennas on various substrates such as paper [6] and textiles [7]. Only recently, fabrication methods for printing plastic and metallic layers have been combined for the development of RF harvesting sensors [8]. However, the devices are fabricated using printing equipment which is relatively expensive and inaccessible for home use.

This chapter is organized as follows. Section 5.2 describes the CP antenna design and performance. Section 5.3 proposes the combined fabrication process of a CP antenna with inexpensive 3D printed equipment. The performance of the antenna is summarised through simulations and experimental results. A conclusion is included in Section 5.4. The finite integration technique (FIT) method included in CST Microwave Studio^{TM} was used for all the simulations in this chapter.

6.2 Antenna design

6.2.1 Dimension

The design of a CP antenna using an asymmetrical patch is a relatively simple process [9]. Figure 6.1 shows the perspective and side views of the configuration and geometry dimensions of such a structure. The main dimensions of the antenna are Ws=100 mm, Ls=100mm, Wp=50.4 mm, Lp=53.6mm, Wf=14.6mm, Lf=11.6mm. The antenna is made up of a rectangular patch element on a square substrate of side

100mm and height 3mm. The rectangular patch is positioned in the center of the square substrate. The antenna is fed by a probe at a location diagonal to the rectangular patch. The required circular polarization is achieved by adjusting the ratio between Wp and Lp of the rectangular patch. The desired input impedance is achieved by optimising the position of the port and therefore the dimensions Wf and Lf. The dielectric permittivity of the SLA printed substrates was given as 2.83 with loss tangent of 0.038 [13]. In simulations, the rectangular patch and the ground plane were set with thickness of 0.1mm.

(a)

(b)
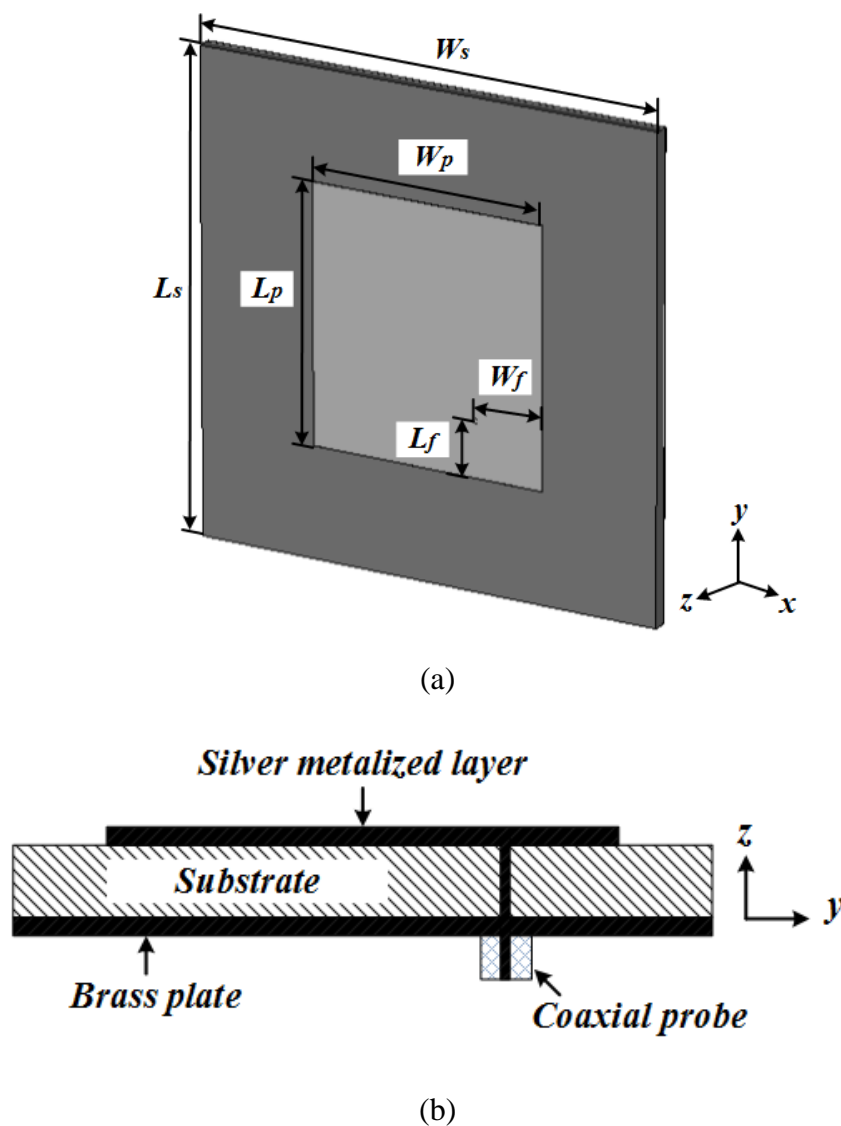
Figure 6.1 Geometry of the antenna (a) perspective view (b) side view

6.2.2 Simulation

The simulated reflection coefficient (S_{11}) of the antenna is presented in Figure 6.2. The antenna had -10dB bandwidth of 7.5%, which spans from 1540MHz to 1660MHz. It can cover the resonant frequency corresponding to the 1575MHz for GPS L1 frequency band. Figure 6.3 shows the simulated axial ratio. It is less than 3dB from 1572MHz to 1603MHz, resulting in 1.9% bandwidth. At the target frequency of 1575MHz the axial ratio (AR) is 2.45dB. The simulated radiation patterns at 1575MHz in two orthogonal planes are shown in Figure 6.4. Patterns were those expected for a CP patch antenna, with the patterns in the *xz* plane and the *yz* plane being very similar.
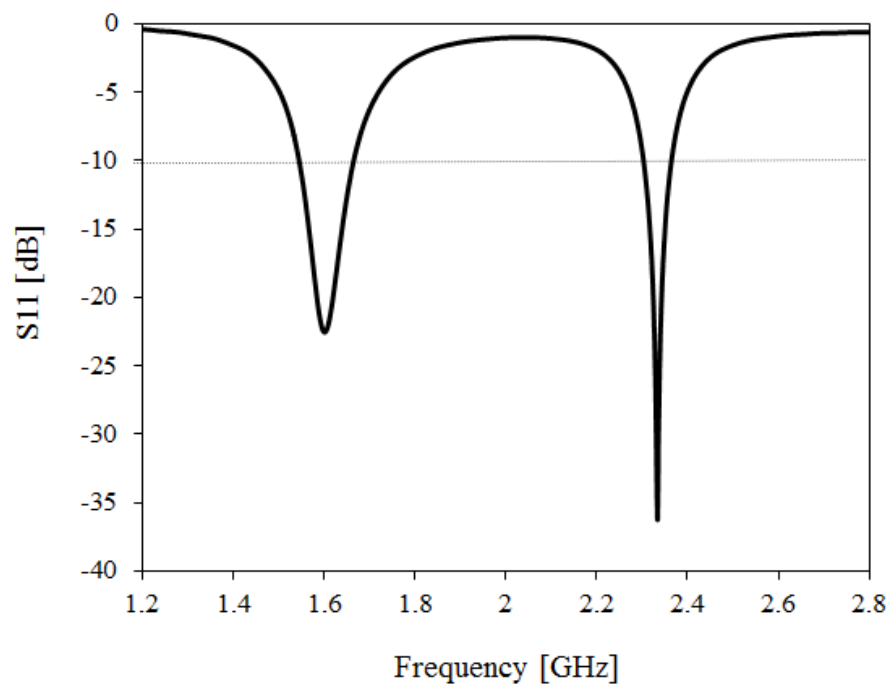
Figure 6.2 Simulated reflection coefficient (S_{11}) of the antenna
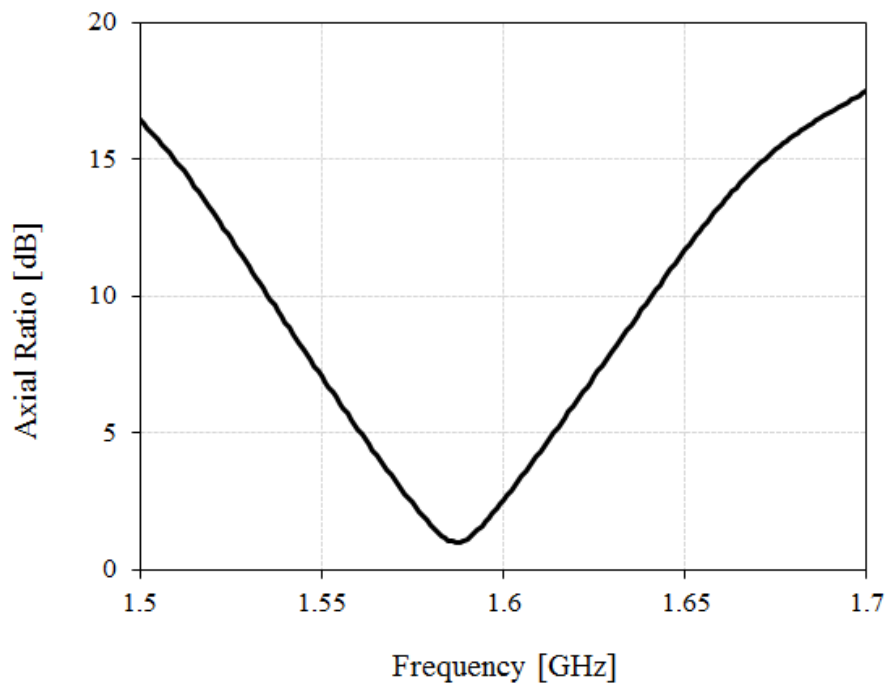
Figure 6.3 Simulated axial ratio of the antenna

(a)   (b)
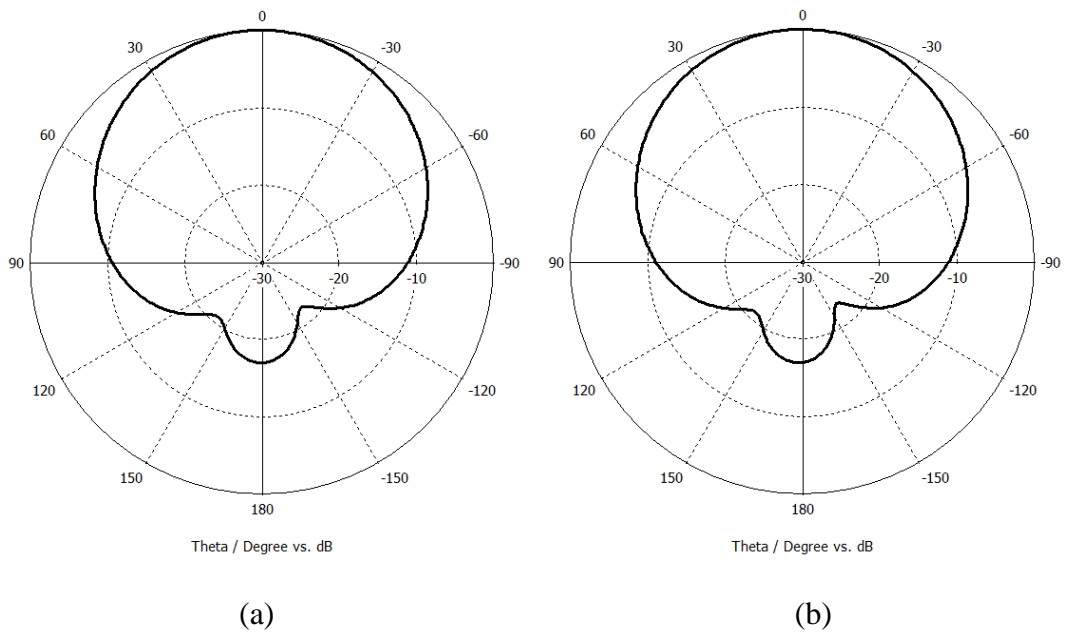
Figure 6.4 Simulated radiation patterns of the antenna at 1575MHz

(a) xz plane (b) yz plane

6.3 Fabrication and measurements

6.3.1 Fabrication

For the fabrication, the 3D geometry of the substrate is transferred to 3D printer using a standard triangulation language (STL) file in CST Microwave Studio[TM]. Formlabs' Form 1+ printer [10] was used for the fabrication of the substrate (Figure 6.5). The fabrication is based on a SLA process where a laser cures layers of UV sensitive resin. Formlab's clear resin was used for the printing of the substrate. The SLA process made the solid object by curing layer after layer of the liquid resin. In the printer, the layer thickness was set to 0.05 mm for high resolution printing. Smoother finishes are obtained compared to the alternative low-cost 3D printer methods such as FDM. Therefore, it is more suitable for combining with inkjet printing as it gives a better surface to bond the silver conductive ink onto. A 100 x 100 x 3 mm^2 substrate was printed using the SLA machine. 60 layers of thickness 0.05mm were necessary to achieve the required height. The surface roughness was 206.2 nm measured in Centre for Process Innovation - CPI [11] and the 2D representation of the surface profile can be seen in Figure 6.6.
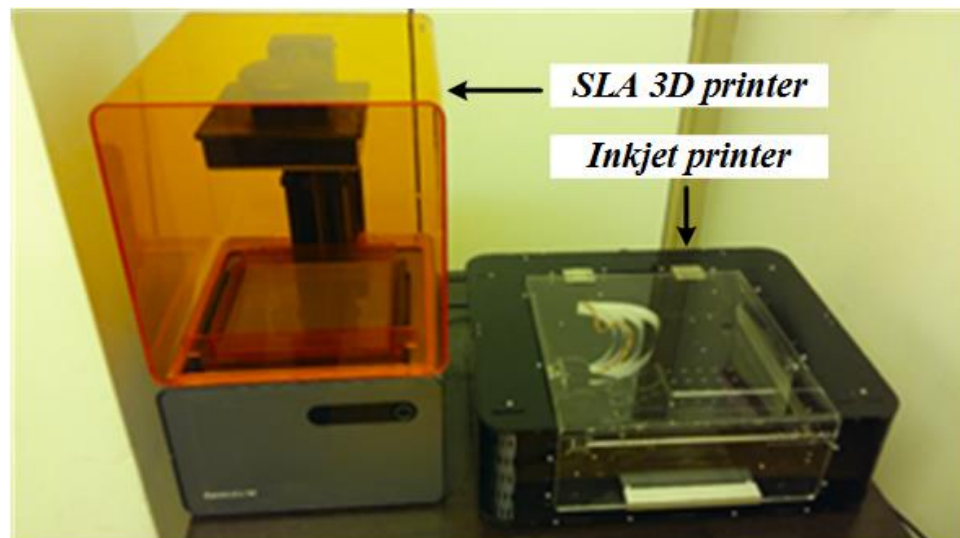
Figure 6.5 3D printing equipment employed

Figure 6.6 Measured surface profile for the 3D printed SLA substrate

The fabrication of the metallic layers was carried out using a Cartesian Co. inkjet printer [12]. The printer used a drop diameter of 0.8 mm to build up multiple metallic layers by repeatedly ejecting drops of inks. The inkjet printer (Figure 6.5) uses two cartridges in tandem. One cartridge contains silver nitrate and the second ascorbic acid (Vitamin C). The ascorbic acid chemically reacts with the silver nitrate to leave the silver metalized layer. Any excess can be washed off as the solution is water soluble. A study of this chemical processes stating the conductivities obtained on various substrates is reported in [13]. The SLA substrate was placed on the plate of the machine and adjusted to the required height. A total of 25 layers were necessary in order to achieve low resistance on the radiator. The resulting patch structure is shown in Figure 6.7. A resistance of 0.4 ohms was measured across the patch after the process was completed. The nature of the deposition of the silver, led to a less even surface profile (Figure 6.8) than for that of the initial SLA substrate (Figure 6.6). The surface roughness of the printed patch was measured to be 7183 nm. To complete the fabrication, a brass ground plane of 100mm by 100mm was placed on the underside of the substrate using double-sided adhesive tape. A 1.3mm hole was then drilled through the ground plane and the substrate to allocate the 50 ohm SMA connector. The SMA connector was soldered to the metallic ground plane. As soldering could damage the substrate and antenna, silver epoxy glue was used to connect the patch.
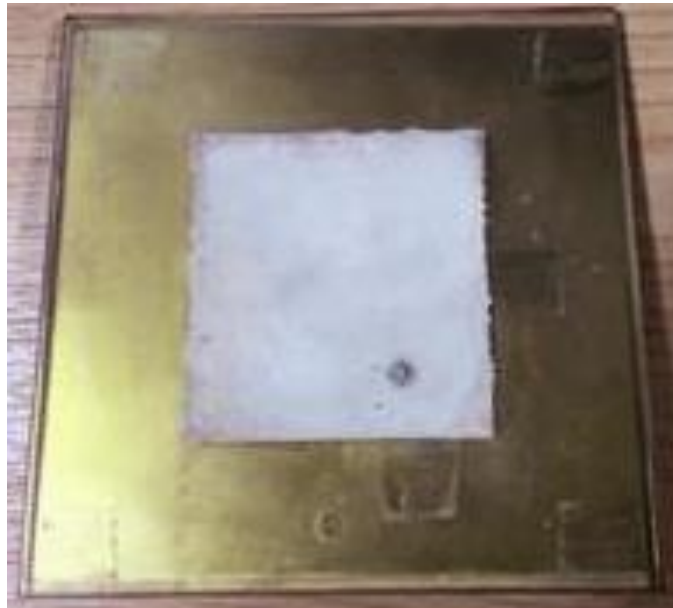
(a)

(b)

Figure 6.7 Inkjet printed antenna on 3D printed SLA substrate

(a) Top view (b) detailed view

6.3.2 Measurement

The measured reflection coefficient of the patch antenna is shown in Figure 6.9. An Anritsu 37397C vector network analyser was used for the measurement. Experiments

compared very well with simulation results. The measured S_{11} has -15dB at the resonant frequency at 1.6GHz and a -10 dB bandwidth of 7%. There was a second resonant mode at about 2400MHz. The resonant frequencies were less than 1% higher than those obtained in the simulations. The measured AR is shown in Figure 6.10. The AR was 2.48dB at 1575MHz. Figure 6.11 and Figure 6.12 show the measurement radiation patterns at 1575MHz and 2400MHz respectively. The measured results are similar to the simulated ones. The maximum measured gain is about 3dBic at 1575MHz.

Figure 6.8 Surface profile for the 3D printed SLA substrate with the silver metalized layers

The difference between the simulation and measurement result is expected from the non-uniform deposited silver metalized layers in the printing and radiation characteristic distortion caused by the leaky surface current of coaxial cable in anechoic chamber.
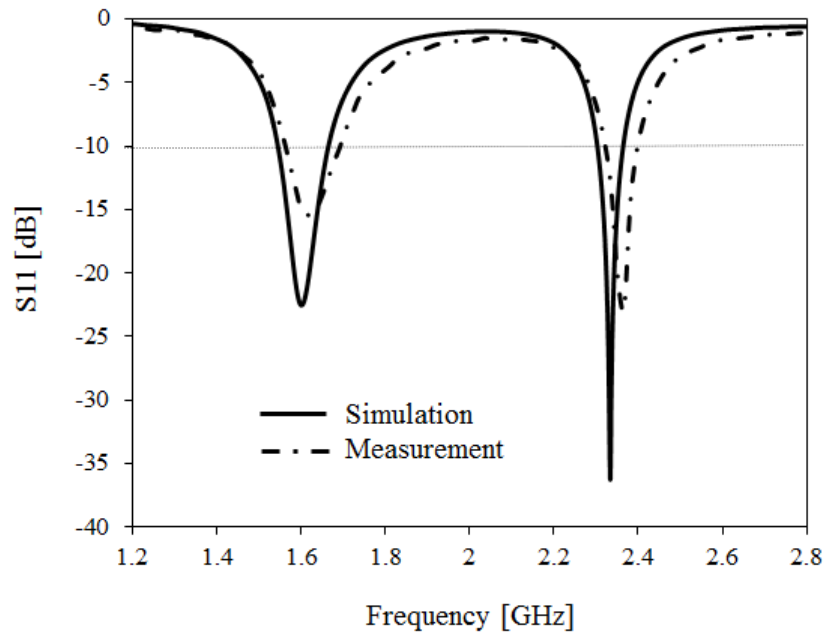
Figure 6.9 Measured and simulated reflection coefficient for the CP antenna
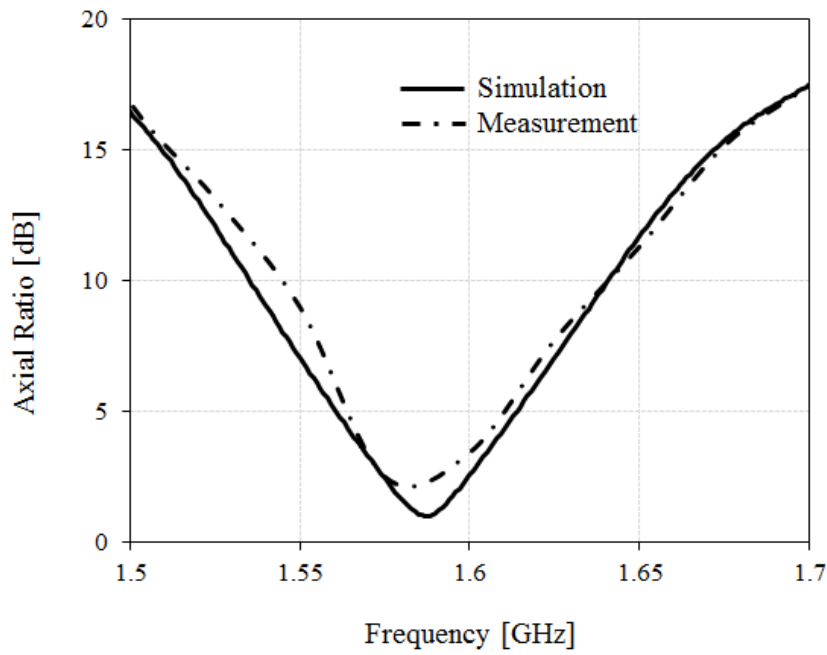
Figure 6.10 Measured and simulated axial ratio
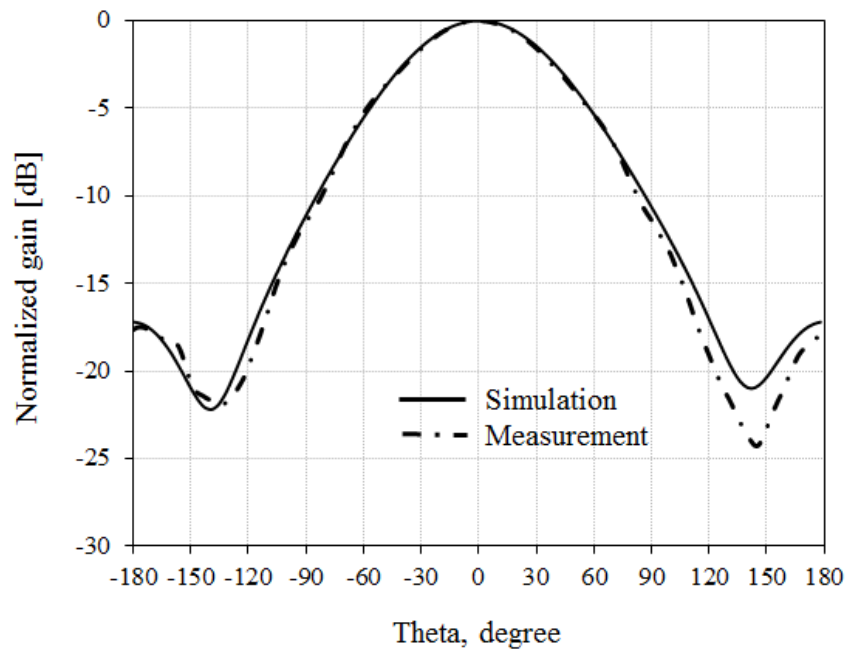
(a)
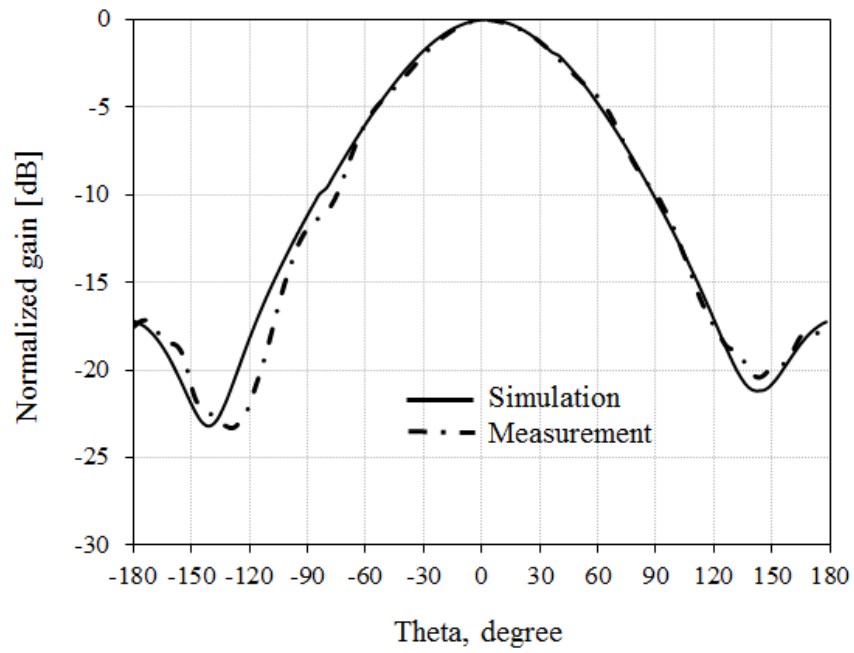
(b)

Figure 6.11 Measured and simulated radiation patterns at 1575MHz

(a) xz plane (b) yz plane

135
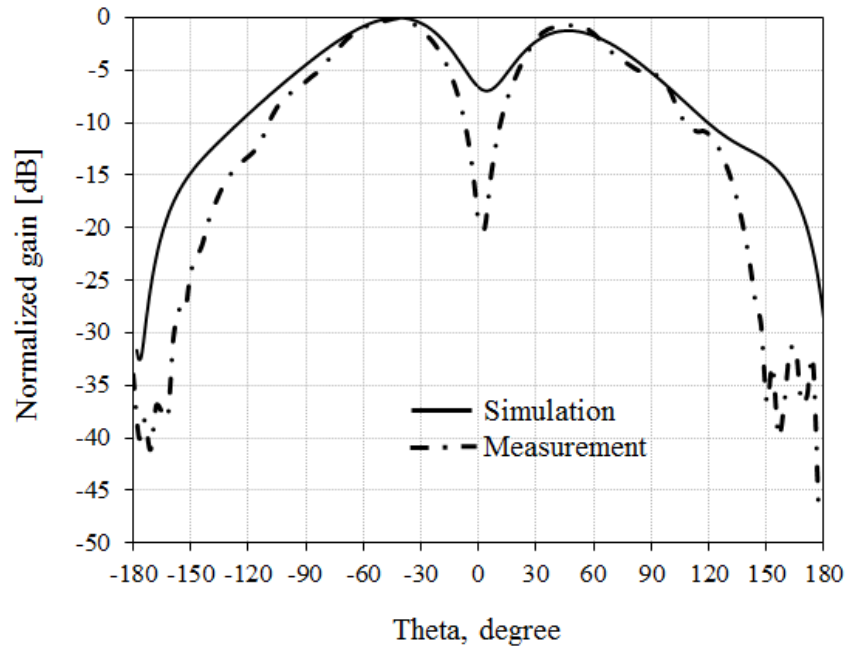
(a)
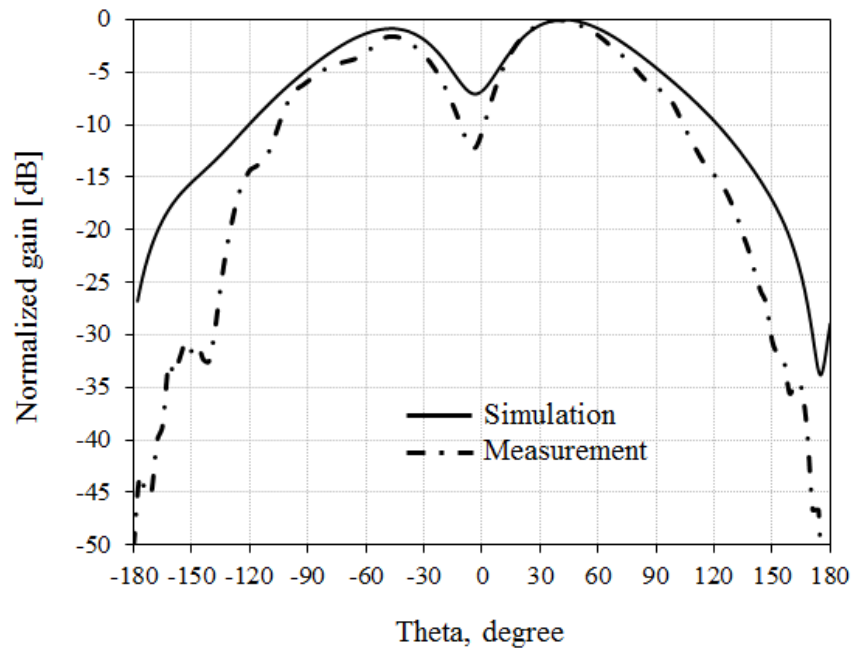
(b)

Figure 6.12 Measured and simulated radiation patterns at 2400MHz

(a) xz plane (b) yz plane

136

6.4 Conclusion

Combining SLA and inkjet printing has been demonstrated to be suitable for the manufacturing of antennas. These technologies are readily available using commercial and inexpensive equipment. The output from the SLA machine is sufficiently smooth to allow the deposition of metallic layers using inkjet printing technology. The inkjet printing process employing silver conductive ink and ascorbic acid seems to be ideal for this application. Furthermore, it produces relatively low resistance when a large number of metallic layers are deposited.

A CP patch antenna was designed, fabricated and tested as an illustration. Good performance in terms of impedance matching, AR and radiation patterns has been achieved. The CP antenna resonates at the 1575 MHz band used for GPS systems. The measured results of the printed antenna compared very well with the computational results. A minor shift in the resonant frequencies was found.

The main advantage over previously reported work is the use of low cost equipment while producing comparable results. For example, the combined technologies are expected to be useful for the fabrication of EBG sensors/detectors (Chapter 4). This process can save both time and costs compared to conventional fabrication techniques (Section 4.3.3). Moreover, the thin-layer substrate printed by the SLA printer is flexible and the metallic layer of the substrate deposited by the inkjet printer can be made for conformal antenna structure. This technology could be used in the future to fabricate antennas on substrates with special properties and internal features that can enhance their performance. Another possibility is to control the deposition of the metallic layers, and therefore optimize the amount of silver conductive ink. This technique could also be used to modify the currents in the antennas and improve results. Future developments on dedicated 3D printing materials with good RF properties are likely to improve the RF performance of devices fabricated using AM techniques.

References

[1] B. Sanz-Izquierdo and E. A. Parker, "3-D Printing of Elements in Frequency Selective Arrays," IEEE Trans. Antennas Propag., vol. 62, pp. 6060-6066, 2014.

[2] S. Jun, B. Sanz-Izquierdo, and E. A. Parker, "3D printing technique for the development of non-planar electromagnetic bandgap structures for antenna applications," Electron Lett., vol. 52, pp. 175-176, 2016.

[3] M. D'Auria, W. J. Otter, J. Hazell, B. T. W. Gillatt, C. Long-Collins, N. M. Ridler, and S. Lucyszyn, "3-D Printed Metal-Pipe Rectangular Waveguides," IEEE Trans. Compon. Packaging Manuf. Technol., vol. 5, pp. 1339-1349, 2015.

[4] P. Nayeri, M. Liang, R. A. Sabory-Garcı´a, M. Tuo, F. Yang, M. Gehm, H. Xin, and A. Z. Elsherbeni, "3D Printed Dielectric Reflectarrays: Low-Cost High-Gain Antennas at Sub-Millimeter Waves," IEEE Trans. Antennas Propag., vol. 62, pp. 2000-2008, 2014.

[5] P. Pa, Z. Larimore, P. Parsons, and M. Mirotznik, "Multi-material additive manufacturing of embedded low-profile antennas," Electron Lett., vol. 51, pp. 1561-1562, 2015.

[6] S. Kim, Y. J. Ren, H. Lee, A. Rida, S. Nikolaou, and M. M. Tentzeris, "Monopole Antenna With Inkjet-Printed EBG Array on Paper Substrate for Wearable Applications," IEEE Antennas and Wireless Propagation Letters, vol. 11, pp. 663-666, 2012.

[7] A. Chauraya, W. G. Whittow, J. C. Vardaxoglou, Y. Li, R. Torah, K. Yang, S. Beeby, and J. Tudor, "Inkjet printed dipole antennas on textiles for wearable communications," IET Microw. Antennas Propag., vol. 7, pp. 760-767, 2013.

[8] J. Kimionis, M. Isakov, B. S. Koh, A. Georgiadis, and M. M. Tentzeris, "3D-Printed Origami Packaging With Inkjet-Printed Antennas for RF Harvesting Sensors," IEEE Trans. Microw. Theory Tech., vol. 63, pp. 4521-4532, 2015.

[9] S. Gao, Luo, Q., and Zhu, F, Circularly polarized antennas. New York: Wiley-IEEE Press, 2013.

[10] Centre for Process Innovation, http:// https://www.uk-cpi.com/, accessed Aug 2017.

[11] Formlabs, http://formlabs.com/, accessed Aug 2017.

[12] Cartesian Co., http://cartesianco.com/, accessed Aug 2017.

[13]   S. M. Bidoki, D. M. Lewis, M. Clark, A. Vakorov, P. A. Miller, and D. McGorman, "Ink-jet fabrication of electronic components," J. Micromech. Microeng., vol. 17, no. 5, pp. 967–974, May 2007.

[14]   Index SAR, http://www.indexsar.com/, accessed Aug 2017.

CHAPTER 7.

3D PRINTING OF CONFORMAL ANTENNAS FOR DIVERSITY WRIST WORN APPLICATIONS

7.1 Introduction

This chapter presents the 3D printing (3DP) of conformal antennas for wrist worn applications. It proposes manufacturing processes to address the challenges related to the 3D printing of antennas on a curved substrate that has been fabricated using inexpensive fuse filament fabrication techniques (FFF). The main issues relate to the surface roughness and surface energy of the FFF substrates. On the other hand, wrist worn devices such as a wristbands and bracelets are made of curved surfaces and require a procedure that is able to print in such shapes. Three additive fabrication processes have been assessed and are discussed here. The first is a multi-step process that is able to smooth the surface and then add metallic layers on a curved bracelet. The second involved painting the antennas on the bracelet and then electroplating. The last uses a machine to fabricate both the antenna and the bracelet.

3DP has also found applications in the development of wearable garments and devices [1]-[5]. Antennas are needed if these wearables are smart and wirelessly connected. Ideally, these antennas should be printed along the wearable structure. A novel loop antenna for wearable applications has been realized by using a flexible 3D printable material in [3]. A dual band CPW fed antenna has been printed on leather substrate for foot wear application in [4]. An inkjet printing method on textiles for wearable antenna is presented in [5].

Antenna diversity is an important technique in advanced microwave wireless and mobile communication systems. Antenna diversity can improve performance and wireless transmission in environments with multipath fading of radio waves [6], [7]. Multipath signal fading causes the restriction in system channel capacity. Body worn systems can benefit from antenna diversity. It can improve channel capacity, compensate for some of the human body effects such as loss in antenna matching, radiation efficiency and blocking of the signal from the human body movements [8] - [11].

This chapter is organized as follows. Section 7.2 describes the antenna design and the fabrication using the multistep process and discusses its performance in free space and at the human wrist. Section 7.3 presents the fabrication of three antennas using silver conductive paint and electroplating. Section 7.4 proposes the manufacturing of the diversity wrist worn antenna using a customized 3D printer. Finally, Section 7.5 discusses all the results and concludes this study. All antenna designs have been simulated using CST Microwave Studio^{TM} and verified with experimental results.

7.2 Wrist worn antenna

7.2.1 Design and Analysis

The dipole antenna is one of the simple radiating structures that can be used for the testing of fabrication processes [12], [13]. It is also suitable for evaluation of the effect of the human body on antenna performance [1], [14]. Figure 7.1 shows the configuration of the dipole antenna with two resonant arms at each end on the 3D bracelet. The inner radiuses of the elliptical bracelet substrate are 35 and 30 mm and the thickness 3 mm. The dimensions have been chosen using an author's wrist. Low-cost polylactic acid plastic filament (PLA) material with dielectric constant of εr =2.4, loss tangent of $tan\delta$ =0.01 is employed as substrate [15]. The dipole antenna has two symmetric arms which allows it to operate at the 2.4 GHz and 5.5 GHz of the WLAN communications. The final dimensions of the antenna after optimization are as follows: $A = 42.4$ mm, $B = 9$ mm, $S = 9$ mm, $L = 24$ mm, $G = 0.4$ mm.

The potential effect of fabrication errors to changes in impedance matching (S_{11}) is shown in Figure 7.2. The length of the two main arms, L and S, are the most likely dimensions to cause a change in resonant frequency of the antenna. The longer arm, L, controls the lower frequency while the second resonator, S, tunes the upper frequency. The antenna is required to cover the 2.4 GHz to 2.5 GHz band and the 5.0 GHz to 6 GHz band with an S_{11} of less than -10 dB. Using this target, the maximum variations allowed are 2 mm (3%) and 1 mm (5%) for the larger (L) and smaller (S) resonators respectively. This is considered to be acceptable for the resolution of the techniques that are described in this chapter.

(a)

(b)
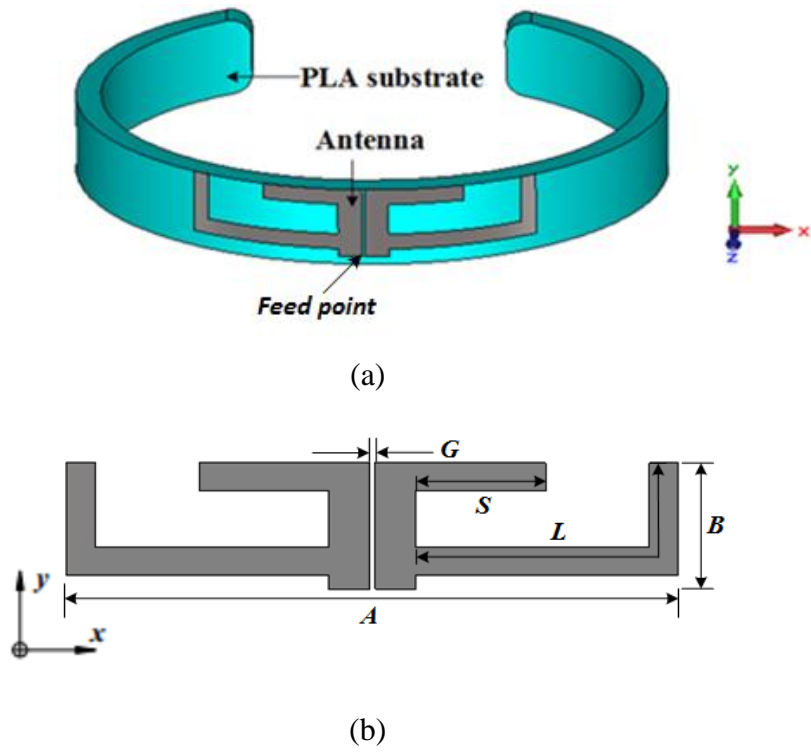
Figure 7.1 Configuration of the wrist worn antenna on the bracelet substrate (a) perspective view (b) dimension.

(a)   (b)
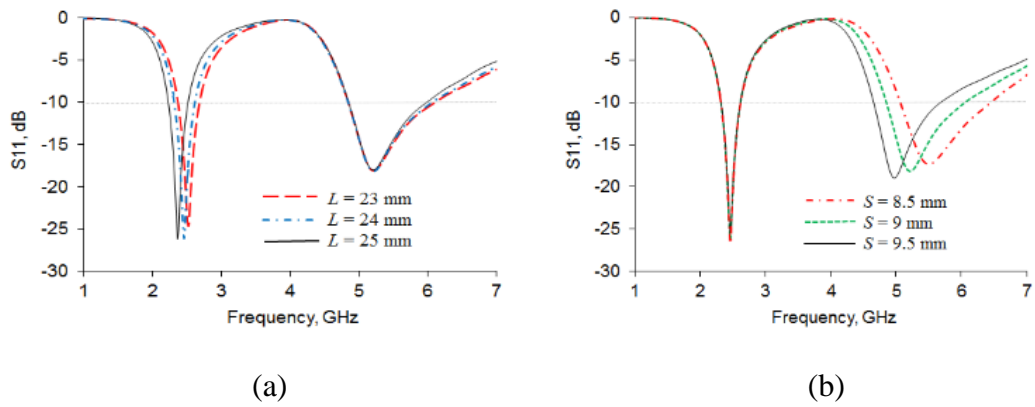
Figure 7.2 Computed sensitivity of the antenna to changes in the dimensions (a) length *L* (b) length *S* on reflection coefficient (S_{11}).

The high relative permittivity of the human body produces a shift in the resonance frequency and reduces antenna efficiency [9]. Therefore, a wrist worn antenna should also be considered with the presence of the human wrist. A three tissue body model is typically employed to emulate this. Figure 7.3(a) shows a cross section of the antenna and bracelet mounted on the elliptical non-homogenous human tissue layers with dimensions of the skin (1 mm), fat (2 mm) and muscle (29 mm). The length of the piece of wrist used for the simulation is 24 mm. The electrical parameters of human tissue layers are given in Table 7.1 [16]. Figure 7.3(b) presents the simulated reflection coefficient (S_{11}) of the proposed antenna for variations of the distance between the bracelet and the human body from 0 to 3 mm, and also free space. The resonant frequencies of the lower and higher bands are shifted down as the gap decreases. The bandwidth of higher frequency also becomes wider. The difference in radiation patterns for the two cases (with vs without human wrist model) is shown in Figure 7.3(c). The human body reduces significantly the back radiating power. This reduction may cause insufficient coverage wireless communications. The coverage can be improved by adding more antennas in the bracelet as described in Section 7.3.
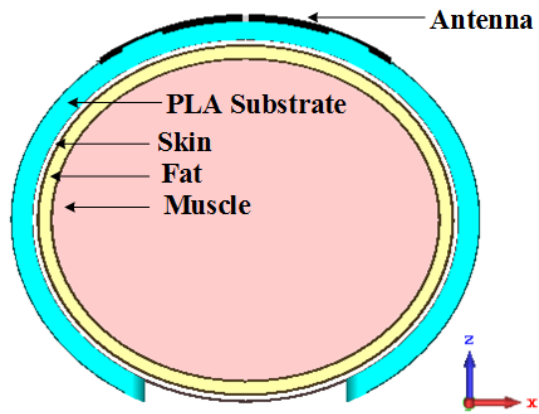
(a)
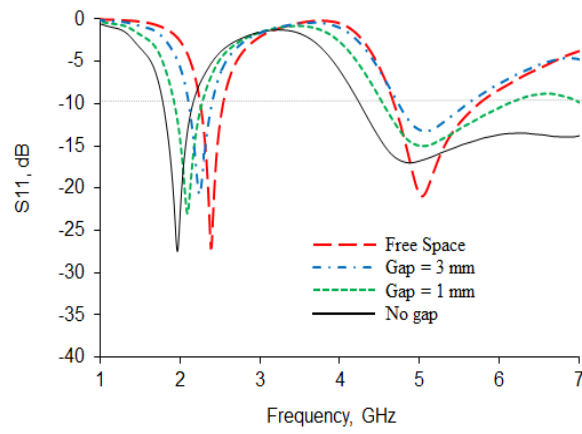
(b)
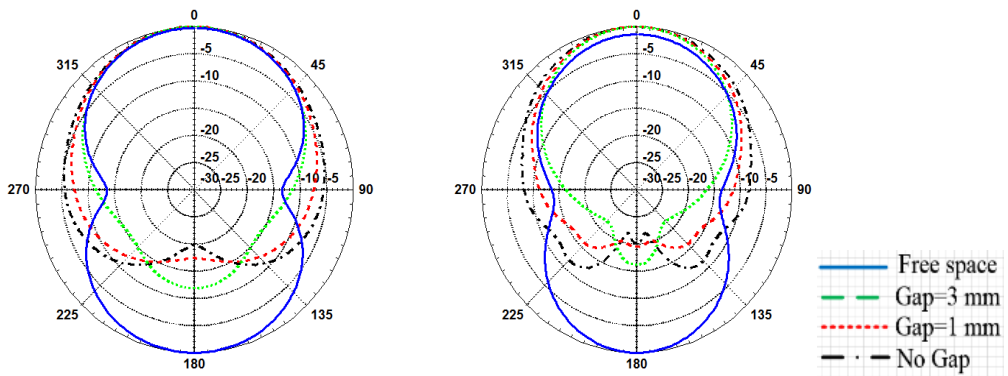
(c)

Figure 7.3 Human wrist model with the wrist wear antenna (a) geometry (b) reflection coefficient (S_{11}) (c) radiation pattern *x-z* plane. (Left: 2.4 GHz, Right: 5.5 GHz).

TABLE 7.1

HUMAN TISSUE LAYERS

	Relative Permittivity		Conductivity	
	2.4 GHz	5.5 GHz	2.4 GHz	5.5 GHz
Skin	38	35.3	1.4	3.4
Fat	5.2	4.9	0.1	0.2
Muscle	52.7	48.8	1.7	4.6

7.2.2 Fabrication using Aerosol Jetting Process

The digital model of the bracelet substrate was exported from CST Microwave Studio^{TM} using an STL file. It was then sent to the Ultimaker 3D printer using CURA software. The density of the printer was set to 100%. White PLA was employed to make the bracelet. Preliminary experiments using Optomec's Aerosol Jet to deposit layers directly on the bracelet were unsuccessful [26]. This was due to problems related to the surface energy and surface roughness of the PLA substrate [17], with the surface energy described in the range of 10 µm to 40 µm in [18]. Surface energy is the ability of the adhesive to deposit the metallic layers. Consequently, a new process was developed and is fully illustrated in Figure 7.4. After printing the bracelet, a layer of fast-acting adhesive (cyanoacrylates) was deposited by using an adhesion substance applied by a hand to smooth the FFF surface as well as to increase the surface energy. Only then the metallic layers were added uniformly using Optomec's aerosol jetting process with silver conductive ink. Owing to the low-temperature characteristics of the FFF substrate, the antenna was cured using a NovaCentrix PulseForge machine [19] via photonic curing technique in the Centre for Process Innovation (CPI) [26]. During the curing process, the conductive layers are heated by pulsed light from a flash lamp with an exposure time of less than a millisecond so that the substrate does not overheat cool. Therefore, the conductive layers are cured without damaging the FFF substrate. The printed antenna was then electroplated to further increase the conductivity. Figure 7.5(a) and Figure 7.5(b) show the photograph of the fabricated antennas before and after electroplating process. The wrist worn antenna was connected by a 50 ohm SMA connector on the top side of the elliptical 3D printed bracelet substrate.
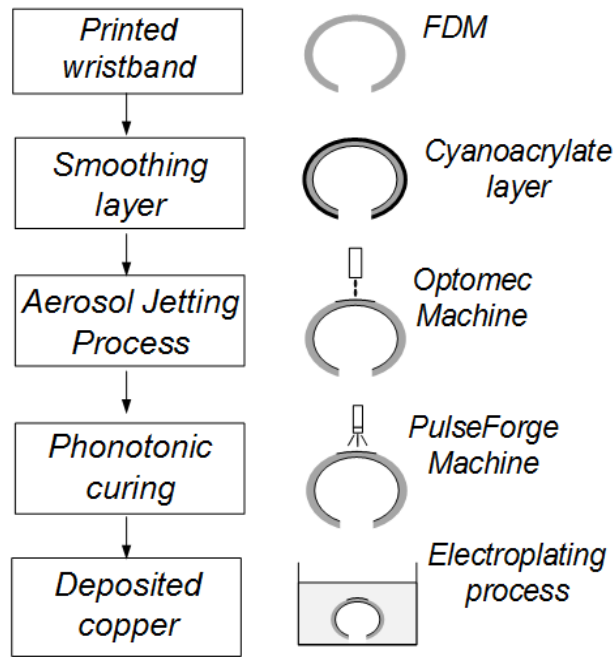
Figure 7.4 Generalized aerosol jetting fabrication process of the wrist wear antenna.

(a)

(b)
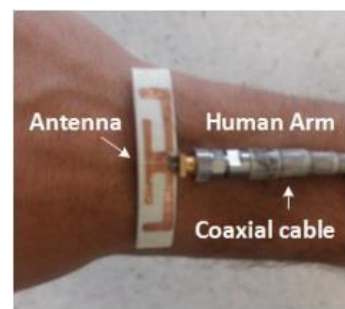
Figure 7.5 Fabricated antenna on the 3D printed bracelet (a) before electroplating (b) after electroplating and with human wrist.

Figure 7.6 shows the surface profile of the printed plastic after the smoothing layer, and also the printed ink layer. The calculation of the surface roughness was done on a TalySurf CCI which provides ultra-high resolution interferometric measurements for non-contact surface roughness. The printed plastic PLA with the layer of glue had a surface roughness of 6 µm. The surface roughness of the silver ink was about 1 µm which is significantly smother than the PLA. This indicates that when the ink is deposited onto the plastic, it levels out, filling in most of the gaps along the surface. The electro plating procedure contributes further to this smoothing process.

(a)   (b)

Figure 7.6 Surface profile map of the 3D printed bracelet (a) PLA substrate after the smoothing layer was applied, and (b) the top metallic layer.

Figure 7.7(a) presents the measured S_{11} of the wrist worn antenna. The measurement was carried out using an Anritsu 37397C vector network analyzer. The S_{11} of the wrist worn antenna on the human wrist is included. The gap from the human wrist to the antenna was set to approximately 5 mm using polystyrene formers. The 2.4 GHz and 5.5 GHz bands were covered with an S_{11} level of less than -10 dB. Figure 7.7(b) shows the measured radiation patterns at 2.4 GHz and 5.5 GHz. Both results show omnidirectional radiation patterns in free space, with increased directionality and mainly directional on the human wrist.

Although this first method was successful, the main drawback was the many processes required for the fabrication of the antenna. Another problem was the fact that the machine used in the jetting process was only able to move in the *x-y* axis and therefore calculations had to be done to produce the curved design. A 3 axis robotic arm would be ideal, but this solution could prove even more costly. In terms of antenna performance, there is a clear limitation as the body reduces significantly the power transmitted backwards and therefore communication coverage. Multiple antenna systems are desirable.

(a)

(b)
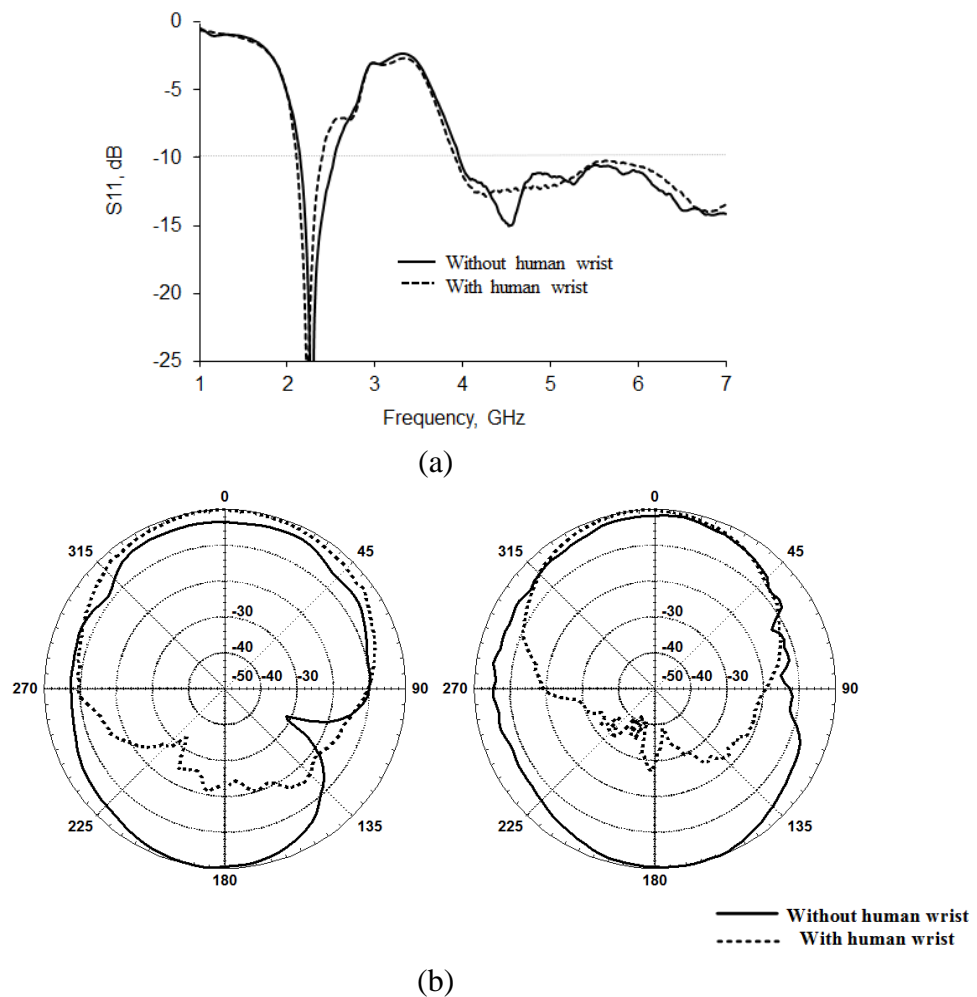
Figure 7.7 Fabricated antenna on the 3D printed bracelet (a) reflection coefficient (S_{11}) (b) radiation pattern (Left: 2.4 GHz, Right: 5.5 GHz)

7.3 Diversity Antenna System

7.3.1 Diversity Antenna Design

There are cases were antennas and circuits might be required to be manufactured in different sections of the bracelet. One example is the use of multiple antennas to increase coverage in the communication system. This type of antenna arrangement is typically defined as space diversity. Figure 7.8 shows a simple antenna diversity solution for the bracelet. Two more antennas have been added symmetrically at a distance of 50.3 mm from the antenna in the centre. The idea is that each antenna may be connected to its own RF circuit and circuit board and is able to send information such as location about the person with the bracelet.

(a)

(b)
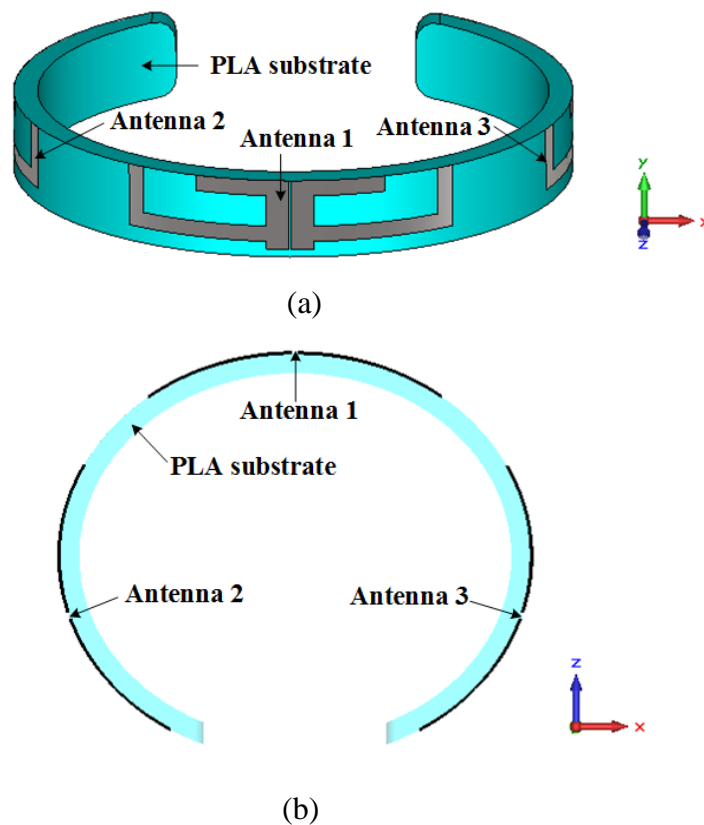
Figure 7.8 Configuration of the diversity wrist worn antenna (a) prospective view (b) top side.

Figure 7.9 shows the main *S* parameters of the three antennas in free space. All antennas cover 2.4 GHz and 5.5 GHz frequency bands with less than -10 dB in their reflection coefficients (S_{ii}). There is also good isolation between the antennas as indicated by the S_{ij} parameters (S_{12}, S_{21}, S_{23}, S_{32}, S_{31}, S_{13}) with a level of less than -10 dB [20]. Figure 7.10 shows the simulated radiation pattern (*x-z* plane) at 2.4 GHz and 5.5 GHz in free space. There is a clear increase in coverage as indicated by the additional power available at 45º, 135º, 225º, and 315º.
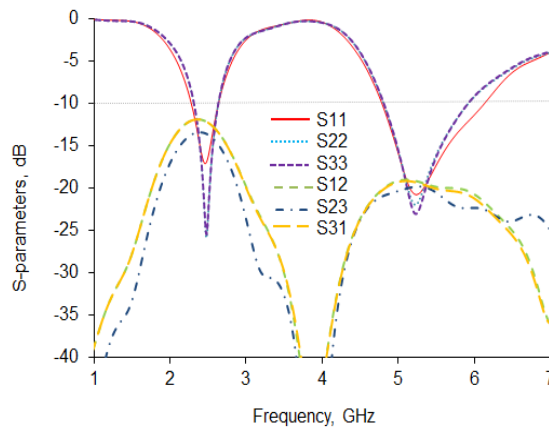
Figure 7.9 Simulated S-parameters of the proposed diversity wrist worn antenna.

(a)   (b)
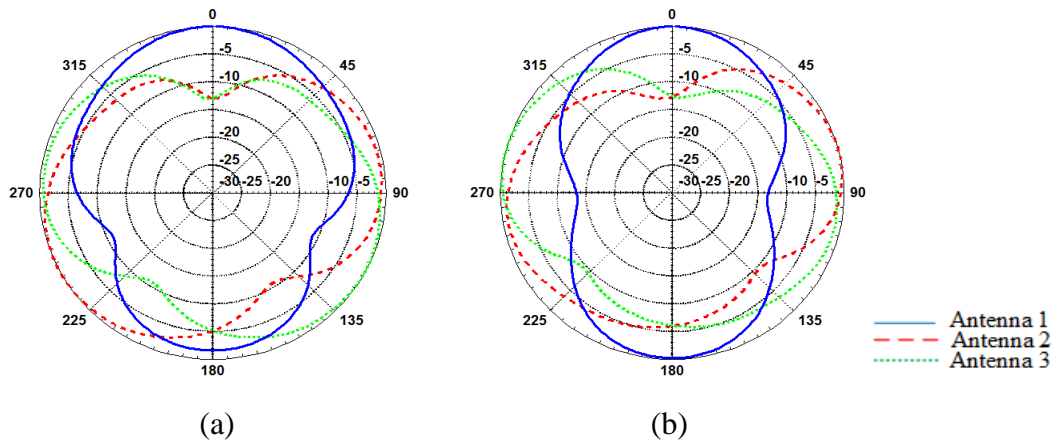
Figure 7.10 Radiation patterns of the diversity wrist worn antenna at (a) 2.4GHz (b) 5.5GHz.

7.3.2 Fabrication by painting the silver conductive ink and Electroplating

This section describes a relatively simple fabrication process of the antenna by combining the silver conductive ink and electroplating process. This is illustrated in Figure 7.11. First, the bracelet was printed with thin grooves of thickness of 0.2 mm. This groove facilitated the painting of the antennas. Then silver conductive ink was applied to the substrate by hand. The specific ink was RS 186-3600 [21]. This ink did not provide sufficient conductivity for low temperature curing. Therefore, a layer of copper of about 50 µm is deposited by electroplating. Figure 7.12. shows the surface profile of the printed layers. The surface roughness of the PLA substrate was about 10 µm while the copper layer was about 3 µm.
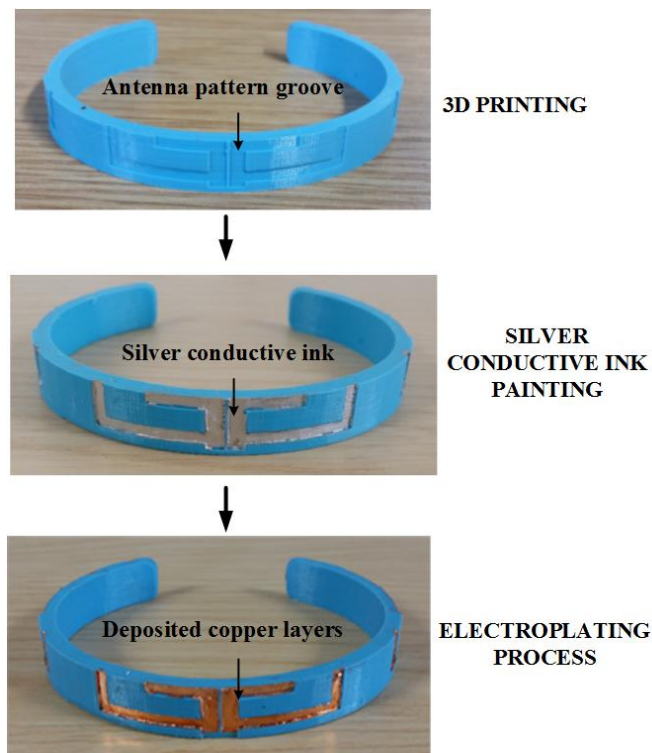
Figure 7.11 Illustration of the first fabrication process for the diversity antenna system.

(a)   (b)

Figure 7.12 Surface profile map for (a) PLA substrate, and (b) Copper layer

Figure 7.13 shows the measured *S* parameter on the human body. Although the S parameters differed between ports, the antennas are able to cover the intended frequency bands. The differences in *S* parameters for various ports is likely to be due to the variation in distances between the antennas and the human body. These variations are likely to occur in real life scenarios. In term of fabrication, imperfect edges were found due to the process of painting the antennas by hand. Figure 7.14 presents the measurement set up for the far field measurements of the antenna with the human wrist. Two scenarios of hand up and hand down were tested.

(a)

(b)
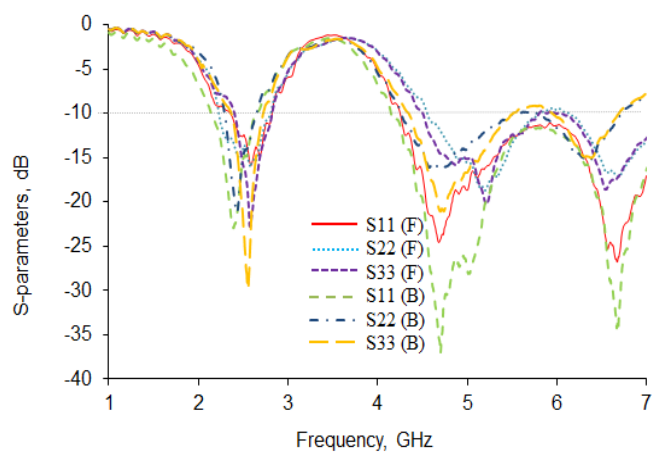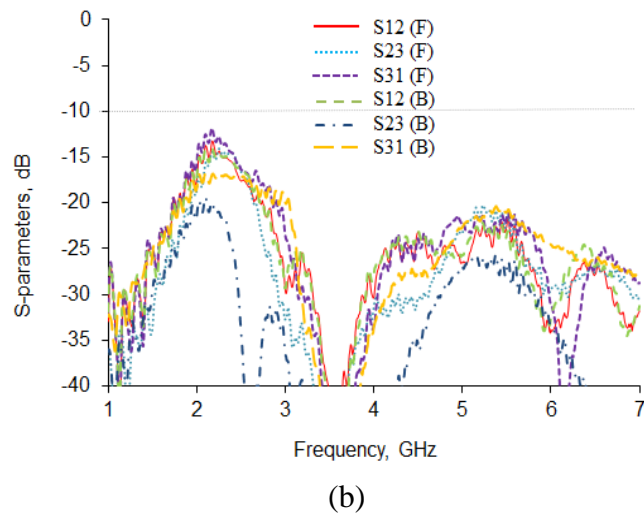
Figure 7.13 Reflection coefficients (S_{11}, S_{22}, S_{33}) and correlation coefficients (S_{12}, S_{23}, S_{31}) of the diversity wrist worn antenna after electroplating process.

(a)   (b)
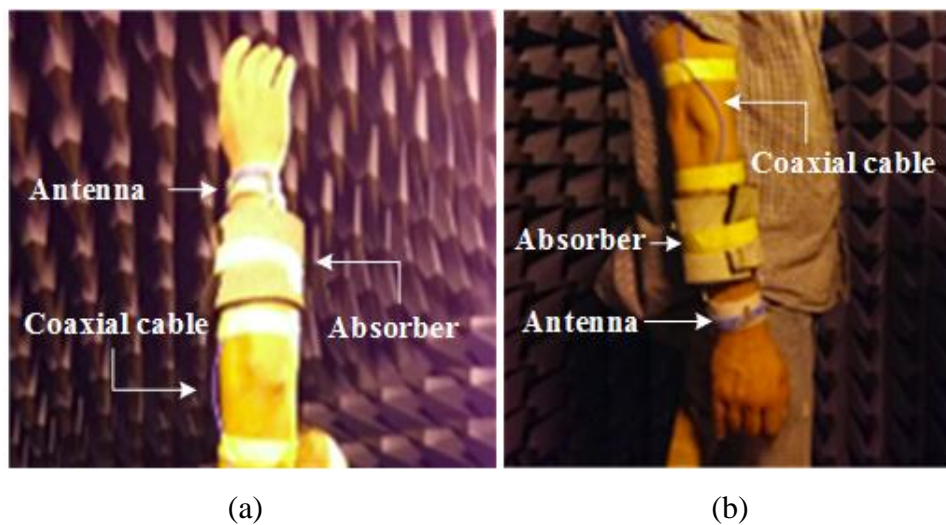
Figure 7.14 Measurement setting in anechoic chamber for radiation patterns of the diversity wrist worn antenna after electroplating process with human wrist (a) Hand up (b) Hand down.

Figure 7.15 and Figure 7.16 present the measured radiation patterns for the two cases. The measured gain at 2.4 GHz and 5.5 GHz was 2.0 dB and 1.3 dB respectively. As seen in the results, both scenarios provided directional radiation pattern on the human body. As expected, the case of the hand down has slightly more backside radiation suppression than the one with the hand up.

(a)   (b)

Antenna 1
Antenna 2
Antenna 3
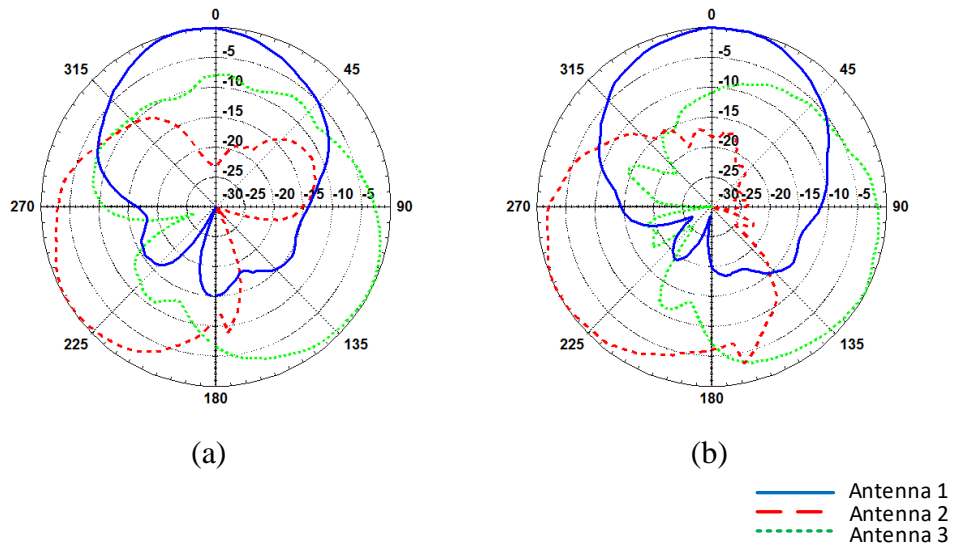
Figure 7.15 Radiation patterns of the diversity wrist worn antennas fabricated by
painting the ink layers (Hand up) at (a) 2.4GHz (b) 5.5GHz.

(a)   (b)

Antenna 1
Antenna 2
Antenna 3
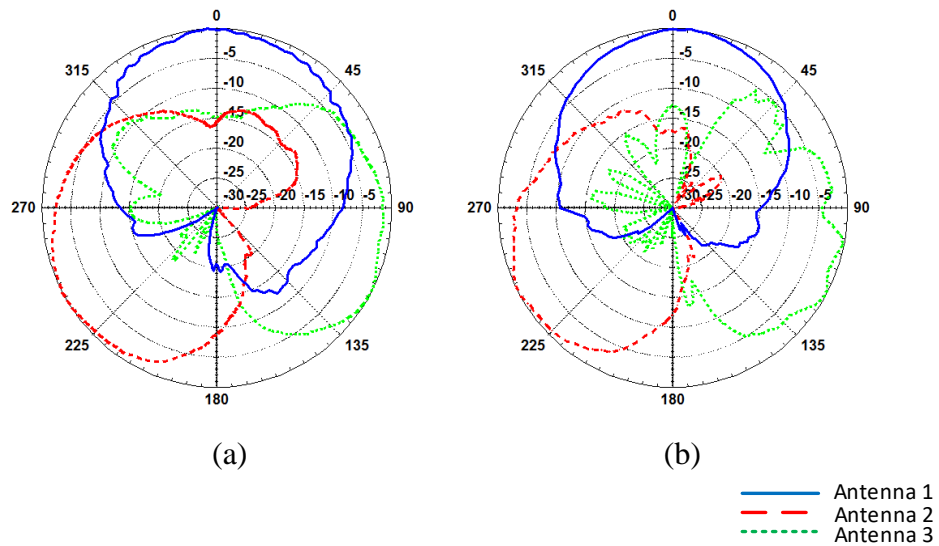
Figure 7.16 Radiation patterns of the diversity wrist worn antennas fabricated by
painting the ink layers (Hand Down) at (a) 2.4GHz (b) 5.5GHz.

7.4 Fully 3D Printed Wrist Worn Antenna

The final fabrication technique tested uses a single machine that combines two
technologies: FFF and direct write. In order to realize such process, a machine was
developed in-house using the open-source Mbot Cube [22] machine as a base frame.
A direct drive extruder was used for the FFF fabrication with a pneumatic dispenser
for the direct write technique. The Techcon TS250 pneumatic dispenser [23] with

output pressure of between 1 - 100 psi was employed. The dispenser was connected to a syringe with a 250 µm nozzle to deposit variable line widths of silver ink.

The machine with the syringe, dispenser, and the plastic extruder are shown in Figure 7.17(a). The dispenser was operated using a serial switch. This connected the printers' microcontroller board to the input trigger of the dispenser. By using a mixture of stepper signals from the RAMPS board, an Arduino was used to turn on or off the dispenser. The dispenser was capable of depositing a layer thickness of less than 200 µm of the silver conductive ink onto the printed plastic substrate with precision. The silver conductive ink used for this work was provided by Voxel8 [23]. The conductivity as stated by the manufacturer is about less than 5.00×10^{-7} Ω-m which makes it highly conductive.

Figure 7.17(b) shows the fully fabricated 3D printed diversity wrist worn antenna. Due to the nature of the bracelets' curvature and the required antenna on each side, the bracelet substrate was printed in two parts. One print was used for the frame of the bracelet substrate and the other to house the antennas. The frame of the bracelet was printed on a rigid, durable yellow PLA plastic filament from 3D FilaPrint [24], which had an infill of 100% and a layer resolution of 100 µm. The thickness of this layer was 2 mm. The top layer of the bracelet was developed using a flexible PLA plastic filament from NinjaFlex [25]. The thickness of this layer was 1 mm. Immediately after printing this layer, the pneumatic dispenser printed the metallic tracks that make the antenna. A single layer of ink was enough to produce a resistance of less the 0.4 Ohm between the two further ends of the dipole arms. Figure 7.18 shows the surface profile of the printed layers. The surface roughness for the flexible PLA was about 11 µm and the metallic ink layer of 2 µm. The flexible printed part with the antennas was mounted onto the rigid frame of the bracelet before the silver conductive ink had fully dried and cured. The two sections were then adhered together using double-sided tape with a thickness of 100 µm.
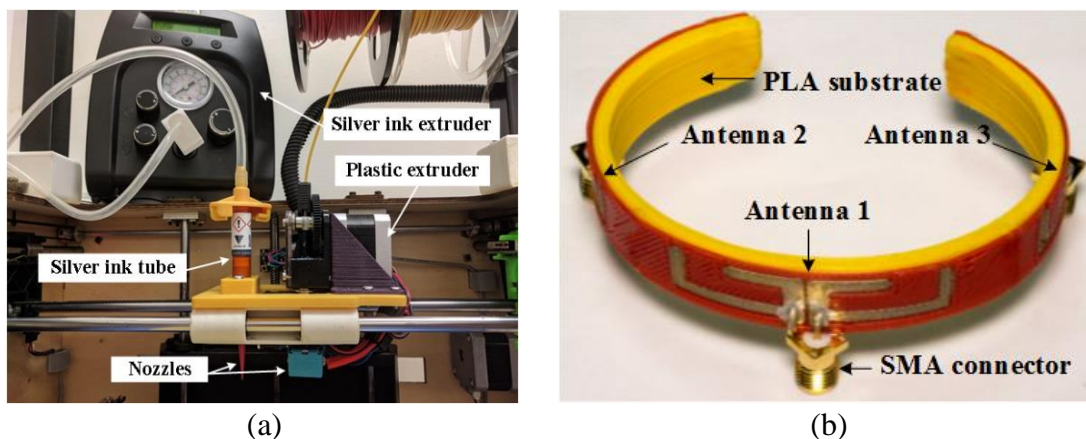
Figure 7.17 Photograph of (a) used open-source 3D printer with dual extruders (b) Fabricated fully 3D printed diversity wrist wear antenna.

(a)   (b)

Figure 7.18 Surface profile map for (a) flexible PLA substrate, and (b) conductive layer.

The measured reflection *S* parameters of fully 3D printed diversity wrist worn antenna are shown in Figure 7.19. In all tests, the 2.4 GHz and 5.5 GHz WLAN band were covered. The -10 dB bandwidth ranges from 2.24 GHz to 3.14 GHz at the lower band and from 4.6 GHz to 7 GHz at the higher land.

Dipole antennas are well known for having balance ports. To suppress unbalanced surface current from the coaxial cable for the radiation measurement purpose, the probe-fed solution of the bazooka balun was applied to the antenna [26]. This was

designed for the 2.4 GHz band. Figure 2.20 shows the antenna system on the human wrist with the baluns.

Figure 7.21 and Figure 7.22 present the radiation patterns. It is evident that the human wrist provides backward signal attenuation. The radiation patterns are not significantly different for two locations of human wrist such as hand up and hand down. The patterns were more directional on the human wrist than in free space. The use of baluns did not show a significant change in the patterns in the x-z plane compared to the straight measurements using coaxial feed.
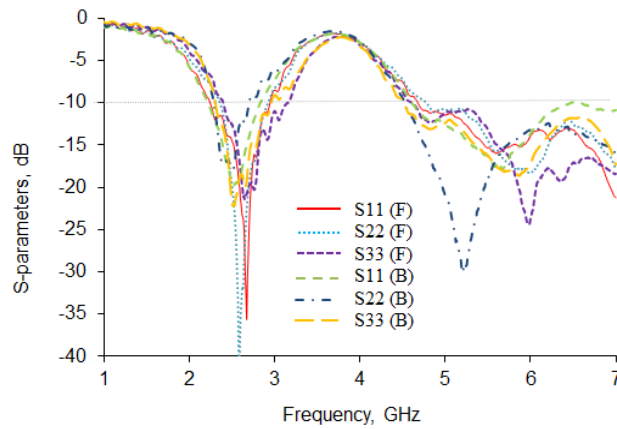
(a)
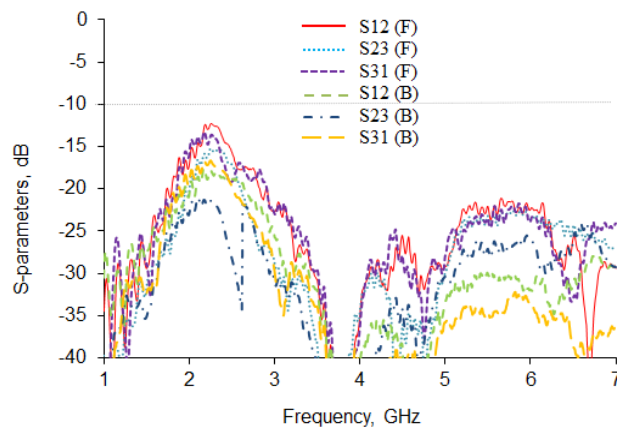
(b)

Figure 7.19 Reflection coefficients (S_{11}, S_{22}, S_{33}) and correlation coefficients (S_{12}, S_{23}, S_{31}) of the fully 3D printed diversity wrist wear antenna.
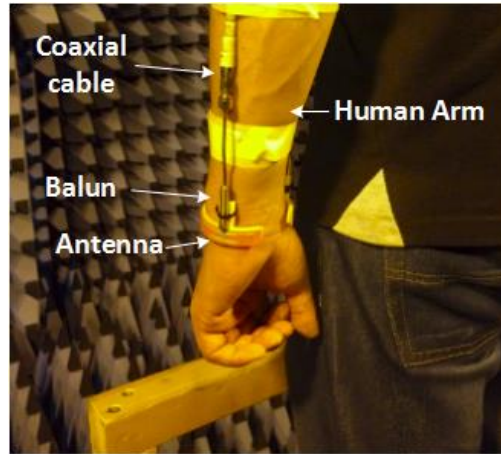
Figure 7.20 Measurement setting in anechoic chamber for fabricated fully 3D printed diversity wrist wear antenna.

(a)   (b)
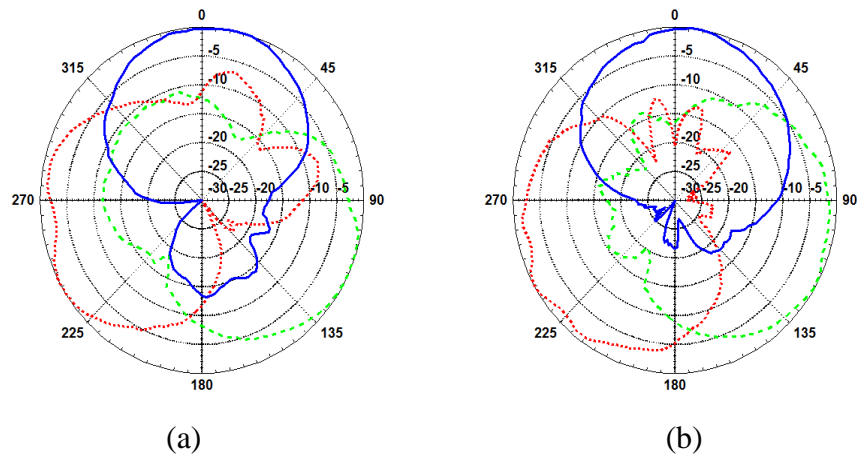
Figure 7.21 Radiation patterns of the fully 3D printed diversity antenna with the human wrist (Hand up) at (a) 2.4GHz (b) 5.5GHz.

(a)   (b)
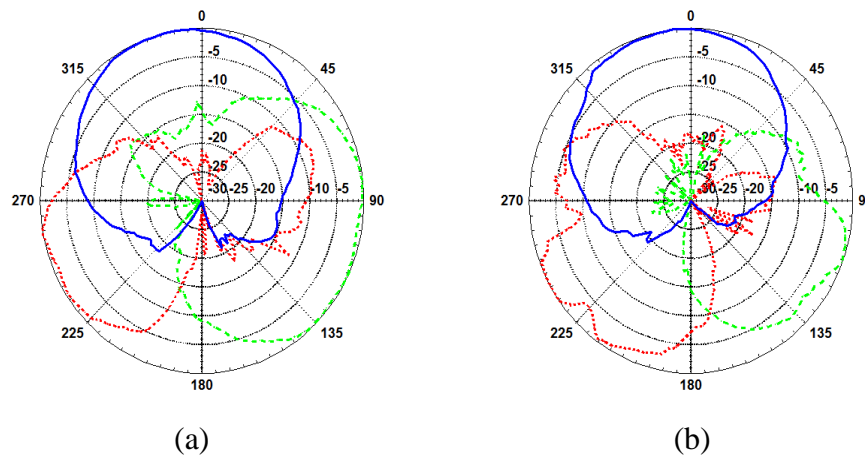
Figure 7.22 Radiation patterns of the fully 3D printed diversity antenna with the human wrist and human body (Hand Down) at (a) 2.4GHz (b) 5.5GHz.

158

7.5 Conclusion

The additive manufacturing of conformal antennas onto a 3D printed wearable bracelet has been demonstrated. An antenna design suitable for the 2.4 GHz and 5.5 GHz WLAN bands has been used for this demonstration. Three different AM procedures have been investigated. The first technique is a multistep process consisting: 3D printing of the bracelet, deposition of a smoothing layer, aerosol jet printing of silver inks, flash curing, and electroplating with copper. The main advantages of this process are the high resolution of the printed antennas and the very smooth and thin metallic layer. The fact that it uses a range of machines means that it could become a chain process and therefore could be scaled up to a medium or even large industrial process. The main disadvantages are the many tasks involved in the fabrication. Only one antenna can be printed in the bracelet fabricated unless a 3-axis deposition process is employed [17].

The second technique involves printing the bracelet with grooves and then painting the metallic layers of the antennas by hand. This process was able to produce three antennas on the same bracelet with various conformal shapes. The main disadvantage is the errors related to the painting of the antennas by hand. This process is more suitable for small scale production and prototyping unless the painting of the metallic tracks is carried out using an automatic procedure.

The final process employs a single machine combining FFF for the fabrication of the bracelet and a pneumatic dispenser for the addition of the metallic layer using silver ink. A flexible PLA substrate has been used so that the antennas are printed in a planar form and then folded to create the bracelet. This has been proven to be the best manufacturing solution in terms of the number of tasks involved, the relative resolution of the printed tracks and the fact that is an automatic procedure. This could be scaled up to a medium industrial process. All techniques described produced good results in terms of S_{11} and radiation pattern. The use of three antennas on a bracelet has been demonstrated to be a good antenna diversity solution capable increasing coverage in wireless body area networks, particularly for off-body applications.

References

[1] B. Sanz-Izquierdo and S. Jun, "WLAN antenna on 3D printed bracelet and wrist phantom", in *2014 Loughborough Antennas and Propagation Conference (LAPC)*, 2014.

[2] S. Jun, B. Sanz-Izquierdo, and M. Summerfield, "UWB antenna on 3D printed flexible substrate and foot phantom," in *2015 Loughborough Antennas and Propagation Conference (LAPC)*, 2015.

[3] M. Rizwan, M. W. A. Khan, L. Sydänheimo, J. Virkki, and L. Ukkonen, "Flexible and Stretchable Brush-Painted Wearable Antenna on a Three-Dimensional (3-D) Printed Substrate," *IEEE Antennas Wireless Propag. Lett.,* vol. 16, pp. 3108-3112, 2017.

[4] M. F. Farooqui and A. Shamim, "Dual band inkjet printed bow-tie slot antenna on leather," in *Antennas and Propagation (EuCAP)*, 2013 7th European Conference on, 2013, pp. 3287-3290.

[5] W. G. Whittow, A. Chauraya, J. Vardaxoglou, Y. Li, R. Torah, K. Yang, S. Beeby, and J. Tudor, "Inkjet-printed microstrip patch antennas realized on textile for wearable applications," *IEEE Antennas Wireless Propag. Lett.*, vol. 13, pp. 71-74, 2014.

[6] J. Winters, J. Salz and R. Gitlin, "The impact of antenna diversity on the capacity of wireless communication systems", *IEEE Transactions on Communications*, vol. 42, no. 234, pp. 1740-1751, 1994.

[7] Lizhong Zheng and D. Tse, "Diversity and multiplexing: a fundamental tradeoff in multiple-antenna channels", *IEEE Trans. Inform. Theory*, vol. 49, no. 5, pp. 1073-1096, 2003.

[8] C. Dietrich, K. Dietze, J. Nealy and W. Stutzman, "Spatial, polarization, and pattern diversity for wireless handheld terminals", *IEEE Trans. Antennas Propagat.*, vol. 49, no. 9, pp. 1271-1281, 2001.

[9] Z. Wang, L. Lee, D. Psychoudakis and J. Volakis, "Embroidered Multiband Body-Worn Antenna for GSM/PCS/WLAN Communications", *IEEE Trans. Antennas Propagat.*, vol. 62, no. 6, pp. 3321-3329, 2014.

[10]   L. Akhoondzadeh-Asl, I. Khan and P. Hall, "Polarisation diversity performance for on-body communication applications", *IET Microw. Antennas Propag.*, vol. 5, no. 2, p. 232, 2011.

[11]   R. Bharadwaj, S. Swaisaenyakorn, C. G. Parini, J. C. Batchelor, and A. Alomainy, "Impulse Radio Ultra-Wideband Communications for Localization and Tracking of Human Body and Limbs Movement for Healthcare Applications," *IEEE Trans. Antennas Propag.*, vol. 65, pp. 7298-7309, 2017.

[12]   I. T. Nassar, T. M. Weller, and H. Tsang, "A 3-D printed miniaturized log-periodic dipole antenna," in *Antennas and Propagation Society International Symposium (APSURSI)*, 2014 IEEE, 2014, pp. 11-12.

[13]   M. Mirzaee and S. Noghanian, "Additive manufacturing of a compact 3D dipole antenna using ABS thermoplastic and high temperature carbon paste," in *Antennas and Propagation (APSURSI), 2016 IEEE International Symposium on*, 2016, pp. 475-476.

[14]   J.-S. Roh, Y.-S. Chi, J.-H. Lee, Y. Tak, S. Nam, and T. J. Kang, "Embroidered wearable multiresonant folded dipole antenna for FM reception," *IEEE Antennas Wireless Propag. Lett.*, vol. 9, pp. 803-806, 2010.

[15]   D. Sjöberg, A. J. Johansson and C. Larsson, "Electromagnetic properties of heterogeneous material structures produced in 3D-printers," *2014 International Conference on Electromagnetics in Advanced Applications (ICEAA)*, Palm Beach, 2014, pp. 605-607.

[16]   Federal Communications Commissions: Body tissue dielectric parameters, http://www.fcc.gov/oet/rfsafety/dielectric.html, C. Gabriel, "Compilation of the dielectric properties of body tissues at RF and microwave frequencies," Report N.AL/OE-TR- 1996-0037, Occupational and Environmental Health Directorate, Radiofrequency Radiation Division, Brooks Air Force Base, Texas, USA, June 1996

[17]   M. Hedges, A. Borras-Marin, "3D Aerosol jet printing - Adding electronics functionality to RP/RM", *Neotech Services MTP*.

[18]   M. S. Alsoufi and A. E. Elsayed, "How Surface Roughness Performance of Printed Parts Manufactured by Desktop FDM 3D Printer with PLA+ is Influenced by Measuring Direction," *American Journal of Mechanical Engineering*, vol. 5, pp. 211-222, 2017.

[19] [online] https://www.novacentrix.com/ (Accessed 03/05/2018)

[20] A. T. M. Sayem, S. Khan, and M. Ali, "A miniature spiral diversity antenna system with high overall gain coverage and low SAR," IEEE Antennas Wireless Propag. Lett., vol. 8, pp. 49–52, 2009.

[21] [online] https://uk.rs-online.com/ (Accessed 03/05/2018)

[22] [online] http://www.mbot3d.com/ (Accessed 03/05/2018)

[23] [online] http://www.voxel8.com/ (Accessed 03/05/2018)

[24] [online] https://shop.3dfilaprint.com/ (Accessed 03/05/2018)

[25] [online] https://ninjatek.com/ (Accessed 03/05/2018)

[26] M. Farooqui, C. Claudel and A. Shamim, "An Inkjet-Printed Buoyant 3-D Lagrangian Sensor for Real-Time Flood Monitoring", *IEEE Trans. Antennas Propagat.*, vol. 62, no. 6, pp. 3354-3359, 2014.

[27] Centre for Process Innovation (CPI), http://www.uk-cpi.com/ (Accessed 03/05/2018)

CHAPTER 8.

CONCLUSION AND FUTURE WORK

8.1 Summary and Conclusion

Additive manufacturing (AM) or 3D printing (3DP) technology is a popular manufacturing process that is currently used for prototyping and fabrication of customized and complex objects. They can improve and add functionality to 3D structures through design flexibility and rapid manufacturing and testing. They also allow for fabrication using different types of materials. The materials typically used for the fabrication are plastics, resins, metals, and composites. The use of AM and 3DP technology can lead to advances in RF/microwave antenna designs in the field of electronics and communication engineering. In these applications, it can be time-efficient, low cost, stable, and lightweight compared to traditional subtractive manufacturing methods.

Many different types of antennas fabricated via AM are reported in this thesis. Various substrates have been used and many applications have been found. This technique has been proven to be suitable for the development and fabrication of antennas using filaments, resins, and powder-based 3DP, as well as inkjet printing. Moreover, silver-loaded conducting inks can be combined with dielectric materials for the development of electromagnetic structures. The surface roughness and surface profile of the printed substrate and the printed metallic layers have also been investigated. This chapter provides a summary of the outcomes arising from the work and some suggestions for future work.

The work began with a review of the most common AM processes and gave an overview of AM applications for antenna and microwave components. AM has been shown to be an alternative fabrication solution to traditional methods and in some

cases can be faster, more accurate, and more reliable, as well as being relatively low cost from the antenna and microwave engineering perspective.

In chapter 3, the use of AM techniques in the fabrication of three-dimensional fractal antennas with complicated geometries has been demonstrated with a relatively simple structure: the Sierpinski Gasket. 3DP enabled the manufacturing in very few separate stages. Such structures can have shapes and internal features that are practically impossible to achieve with standard fabrication techniques. Currently, 3DP with metals is relatively expensive when compared with traditional fabrication methods, which can limit its use to the development of antennas for high-end products. In addition to their intrinsic characteristics, the fractals in AM have the further advantage of reducing the amount of metal employed, and thereby reducing costs compared with the AM of the equivalent non-fractal designs.

In chapter 4, a novel reconfigurable electromagnetic band gap (EBG) technique suitable for sensing applications has been developed. The reconfigurable behavior of the EBG is obtained by creating trenches between the unit cells and filling them with liquids of different permittivities. The sensor/detector technique can be integrated as part of a wireless sensor network. The applicability of inexpensive additive manufacturing technologies to the development of such non-planar EBG substrates for antenna applications has also been demonstrated. Low-cost materials such as polylactic acid plastic filaments are suitable for this purpose. Silver-loaded conducting ink was painted on the 3D printed non-planar EBG structure using an EBG mask that had also been printed. This technique could be used for antennas and complex 3D EBG structures.

Chapter 5 presented an investigation of inkjet printed antennas for disposable paper drones. A commercially available, low-cost, inkjet printer with cartridges filled with nanoparticle silver conductive ink can produce functional antennas for this application. The feasibility of producing paper based antennas for disposable drones using low-cost inkjet printing techniques has been demonstrated. The antenna operates at the existing 2.4 GHz and 5 GHz bands. Inexpensive inkjet printing technology may prove to be a useful fabrication method to meet the requirements for

disposable drone applications. In the future, disposable origami drones may include other electronic components that are also inkjet printed along the antenna. This will create a fully integrated disposable drone solution.

In chapter 6, the fabrication of a circularly polarized (CP) patch antenna with inexpensive 3D printed equipment was explored. Stereolithography (SLA) techniques can produce substrates with surfaces smooth enough to be suitable for printing conductive layers with inkjet printing processes. Inkjet printing of metallic layers can be achieved using low-cost inkjet printer, which uses a combination of ascorbic acid and silver nitrate. Good performance has been achieved in terms of impedance matching, axial ratio, and radiation patterns. The CP antenna resonates at the 1575 MHz band used for GPS systems. The advantage of the proposed fabrication method over previously reported work is the use of low-cost machines that are suitable for both home and office use.

Chapter 7 discussed the application of 3DP printing techniques to the development of conformal antennas for diversity wrist worn wireless communications. Three additive manufacturing procedures are investigated. First, a multi-step process is done to combine the addition of a layer to smooth the surface of the band, a jetting process that deposits the metallic tracks, a flash-curing system, and an electroplating process. Next, the process combines the act of painting of the metallic layers by hand and electroplating. The final process employs a single machine that combines fuse filament fabrication for the fabrication of the bracelet and a pneumatic dispenser for the addition of the metallic layer using silver ink. All methods produced reasonably good results, with the last method being the preferred choice for the authors due to the all-in one machine process employed. These antennas could be used in wireless location systems where each antenna is connected to a radio frequency (RF) circuit board and processor.

8.2 Future work

The work reported in this thesis has demonstrated the capability of 3DP for the fabrication of complex antenna structures. As an alternative method, inkjet-printing

technology was also presented for antenna application on a planar paper substrate. Furthermore, both technologies allowed the deposition of conductive inks on dielectric materials, enabling the fabrication of planar and non-planar antennas. Further research will be done to fabricate inkjet-printed antennas for application in an origami-style jumping robot.

3D origami antennas have been proposed in recent years. They offer frequency and radiation reconfigurability for satellite and wireless communications systems [1]-[3]. A deployable quadrifilar helix antenna (QHA) and a conical log spiral antenna (CLSA) were developed for the UHF band in [1]. In [2], a foldable frequency-selective surface (FSS) was able to tune the frequency of operation. A 3D origami antenna based on an accordion structure was designed and studied in folded or unfolded conditions in [3].

The main disadvantage of 3D origami antennas is their complexity and the need for flexible materials to realize the various folds necessary to produce the final model. This means that more sophisticated fabrication methods are necessary than those required for 2D structures, making them more time consuming and expensive. The use of paper substrates is a very attractive solution for origami applications, particularly if combined with inkjet printing technology. One of the problems with inkjet printing is that the deposited layers of nanoparticle silver inks cannot be folded easily without producing cracks and discontinuities [4].

An inkjet-printed dual band antenna for low-cost origami jumping robots [5]-[7] will be presented in future work. The antenna is designed to follow the geometry of the top surface of the origami frog, achieving the optimal dimensions for both the antenna and the origami sheet. The model is fabricated directly onto photo paper using inexpensive inkjet-printing technology and then folded to form an origami frog. As a result of the design features of the antenna, the printed metallic layers are not folded, avoiding potential cracks during the movement of the robot. The fabricated antenna is tested and investigated in uncompressed and compressed states. The effect of the proximity of the antenna to the concrete in a realistic environment was also

studied. The antenna design will be optimized and simulation performance studies carried out using CST Microwave Studio^{TM}.

References

[1] J. Costantine, Y. Tawk, I. Maqueda, M. Sakovsky, G. Olson, S. Pellegrino and C. Christodoulou, "UHF Deployable Helical Antennas for CubeSats", IEEE Trans. Antennas Propagat., vol. 64, no. 9, pp. 3752-3759, 2016.

[2] K. Fuchi, Junyan Tang, B. Crowgey, A. Diaz, E. Rothwell and R. Ouedraogo, "Origami Tunable Frequency Selective Surfaces", IEEE Antennas Wireless Propag. Lett., vol. 11, pp. 473-475, 2012.

[3] S. Yao, S. V. Georgakopoulos, B. S. Cook, and M. M. Tentzeris, "A novel reconfigurable origami accordion antenna," in Proc. IEEE MTT-S Int. Microw. Symp. (IMS), Tampa, pp. 1–4, 2014.

[4] H. AbuTarboush, M. Farooqui and A. Shamim, "Inkjet-Printed Wideband Antenna on Resin-Coated Paper Substrate for Curved Wireless Devices", IEEE Antennas Wireless Propag. Lett., pp. 1-1, 2015.

[5] M. Kovac, M. Fuchs, A. Guignard, J.-C. Zufferey, and D. Floreano, "A ˇ miniature 7 g jumping robot," in Proc. IEEE Int. Conf. Robot. Autom., pp. 373–378, 2008.

[6] M. Kovac, M. Schlegel, J.-C. Zufferey, and D. Floreano, "Steerable minia- ˇ ture jumping robot," Auton. Robots, vol. 28, no. 3, pp. 295–306, 2010.

[7] S. Miyashita, S. Guitron, M. Ludersdorfer, C. R. Sung, and D. Rus, "Untethered miniature origami robot that self-folds, walks, swims, and degrades," in Proc. of the IEEE Int. Conf. on Robotics and Automation (ICRA), pp. 1490–1496, 2015.